Submonolayer-grown Quantum Dots for Nonlinear Device Applications

vorgelegt von

MSc. Bastian Herzog

ORCID: 0000-0001-6653-3596

Von der Fakultät II - Mathematik und Naturwissenschaften
der Technischen Universität Berlin
zur Erlangung des akademischen Grades

Doktor der Naturwissenschaften

– Dr. rer. nat. –

genehmigte Dissertation

Promotionsausschuss:

Vorsitzender: Prof. Dr. Mario Dähne (TU Berlin)

Gutachterin: Prof. Dr. Ulrike Woggon (TU Berlin)

Gutachter: Prof. Dr. Wolfgang Elsäßer (TU Darmstadt)

Tag der wissenschaftlichen Aussprache: 20. September 2019

Berlin 2019

Abstract

The submonolayer (SML) growth method was developed as an alternative to the established Stranski-Krastanow (SK) technique in order to produce quantum dots (QDs) with higher areal density and consequently larger optical gain. In this dissertation, fundamental and applied aspects of SML-grown QDs as active media in optoelectronic devices are investigated using different optical spectroscopy methods. While application-relevant properties of SK QDs have been investigated comprehensively and possibilities and limitations were highlighted, the full potential of SML QDs has not yet been fully exploited. In the context of this work, devices with two different types of SML QD types were investigated: InAs/GaAs structures with and without the alloy of antimony (Sb). Integrated into optical semiconductor amplifiers, remarkably fast gain recovery dynamics on a single-digit picosecond time scales were observed. Using microscopically motivated rate equation modeling in cooperation with B. Lingnau (TU Berlin), this could be attributed to an efficient coupling of the localization centers to a reservoir of unbound charge carriers. Additionally, these were identified to cause an accompanying large phase response of the system. Henry's α-parameter was used to quantify the coupling of amplitude and phase, which was up to five times higher than amplifiers based on SK QDs or quantum wells (QWs). While a high value of α is parasitic for linear amplification, it is desirable for nonlinear operation.

In a study on semiconductor lasers, an increase in threshold current and gain bandwidth, as compared to QW-based lasers was observed. This is mainly attributed to the inhomogeneous broadening of the QD sizes, which in particular for the Sb-alloyed structures is further extended by an additional deeper exciton state. The high nonlinearity expressed in α was finally exploited via application of time-delayed optical feedback to SML QD based lasers, which successfully to drove the laser into a regime of chaotic pulsations.

ii

Zusammenfassung

Die Submonolagen (SML) Wachstumsmethode wurde als Alternative gegenüber der etablierten Stranski-Krastanov (SK) Technik entwickelt, um Quantenpunkte (QPe) mit höherer Dichte und damit einhergehend, höherem optischen Gewinn herzustellen. In dieser Dissertation werden mittels verschiedener optischer Spektroskopie-Methoden fundamentale und anwendungsrelevante Aspekte von SML-gewachsenen QPen als aktives Medium in optoelektronischen Bauelementen untersucht.

Während anwendungsnahe Eigenschaften von SK QPen weitgehend erforscht und Möglichkeiten und Grenzen herausgestellt wurden, sind bei SML QPen noch nicht alle Potentiale ausgeschöpft. Im Rahmen dieser Arbeit wurden Bauelemente mit zwei verschiedenen Arten von SML QP Arten untersucht: reine -, sowie mit Antimon (Sb) legierte InAs/GaAs Strukturen. Eingebracht in optische Halbleiterverstärkern, wurde eine besonders schnelle Gewinndynamik auf einstelliger Pikosekunden-Zeitskala beobachtet. Anhand von Ratengleichungsmodellierungen von B. Lingnau (TU Berlin) konnte diese auf eine effiziente Kopplung der Lokalisierungszentren an ein Reservoir ungebundener Ladungsträger zurückgeführt werden. Diese wurden zusätzlich als Ursache für eine ungewöhnlich große Phasenantwort des Systems identifiziert. Mit Hilfe von Henry's α-parameter konnte die Kopplung von Amplitude und Phase quantifiziert werden, welche im Vergleich zu Verstärkern basierend auf SK QPen oder Quantenfilmen (QFen) einen bis zu fünffachen Wert annahm. Während dieser hohe Wert für lineare Verstärkung parasitär wirkt, ist er im Falle von nichtlinearem Betrieb durchaus wünschenswert.

In einer Studie an Halbleiterlasern wurde eine Erhöhung des Schwellstroms und der Gewinnbandbreite im Vergleich zu QF-basierten Lasern beobachtet. Dies wird vorwiegend auf die inhomogene Verbreiterung der SML QP-Größen zurückgeführt, welche im Falle von Sb-legierten SML QPen noch durch einen zusätzlichen tieferen Zustand erweitert wird. Die hohe Nichtlinearität in Form von α wurde schließlich ausgenutzt, um mittels zeitverzögerter optischer Rückkopplung erfolgreich chaotische Laserfluktuation zu erzeugen.

Publications

Peer Reviewed Publications Related to this Thesis

[1] B. Herzog, B. Lingnau, M. Kolarczik, S. Helmrich, A. W. Achtstein, K. Thommes, F. Alhussein, D. Quandt, A. Strittmatter, U. W. Pohl, O. Brox, M. Weyers, U. Woggon, K. Lüdge and N. Owschimikow, *"Broadband Semiconductor Light Sources Operating at 1060 nm Based on InAs:Sb/GaAs Submonolayer Quantum Dots"*, IEEE J. Select. Top. Quantum Electron. **25**, 1900310 (2019).

[2] B. Lingnau, K. Lüdge, B. Herzog, M. Kolarczik, Y. Kaptan, U. Woggon and N. Owschimikow, *"Ultrafast gain recovery and large nonlinear optical response in submonolayer quantum dots"*, Phys. Rev. B **94**, 014305 (2016).

[3] B. Herzog, B. Lingnau, M. Kolarczik, Y. Kaptan, D. Bimberg, A. Maassdorf, U. W. Pohl, R. Rosales, J.-H. Schulze, A. Strittmatter, M. Weyers, U. Woggon, K. Lüdge and N. Owschimikow, *"Strong amplitude-phase coupling in submonolayer-quantum-dots"*, Appl. Phys. Lett. **109**, 201102 (2016).

[4] B. Herzog, N. Owschimikow, J.-H. Schulze, R. Rosales, Y. Kaptan, M. Kolarczik, T. Switaiski, A. Strittmatter, D. Bimberg, U. W. Pohl and U. Woggon, *"Fast gain and phase recovery of semiconductor optical amplifiers based on submonolayer quantum dots"*, Appl. Phys. Lett. **107**, 201102 (2015).

Other Peer Reviewed Publications

[5] M. Kolarczik, C. Ulbrich, P. Geiregat, Y. Zhu, L. K. Sagar, A. Singh, B. Herzog, A. W. Achtstein, X. Li, D. van Thourhout, Z. Hens, N. Owschimikow, and U. Woggon. *"Sideband Pump-Probe Technique Resolves Nonlinear Modulation Response of PbS / CdS Quantum Dots on a Silicon Nitride Waveguide."* APL Photonics **3**, 016101 (2018).

[6] B. Lingnau, Benjamin, B. Herzog, M. Kolarczik, U. Woggon, K. Lüdge, and N. Owschimikow. *"Dynamic Phase Response and Amplitude-Phase Coupling of Self-Assembled Semiconductor Quantum Dots."* Appl. Phys. Lett. **110**, 241102 (2017).

[7] M. Kolarczik, M., Nina Owschimikow, B. Herzog, F. Buchholz, Y. Kaptan, and U. Woggon. *"Exciton Dynamics Probe the Energy Structure of a Quantum Dot-in-a-Well System: The Role of Coulomb Attraction and Dimensionality."* Phys. Rev. B **91**, 235310 (2015).

[8] Y. Kaptan, A. Röhm, B. Herzog, B. Lingnau, H. Schmeckebier, D. Arsenijevic, V. Mikhelashvili, O. Schöps, M. Kolarczik, G. Eisenstein, D. Bimberg, U. Woggon, N. Owschimikow, and K. Lüdge. *"Stability of Quantum-Dot Excited-State Laser Emission under Simultaneous Ground-State Perturbation."* Appl. Phys. Lett. **105**, 191105 (2014).

[9] Y. Kaptan, H. Schmeckebier, B. Herzog, D. Arsenijevic, M. Kolarczik, V. Mikhelashvili, N. Owschimikow, G. Eisenstein, D. Bimberg, and U. Woggon. *"Gain Dynamics of Quantum Dot Devices for Dual-State Operation."* Appl. Phys. Lett. **104**, 261108 (2014).

Book Chapter

- M. Kneissl, A. Knorr, S. Reitzenstein, and A. Hoffmann (ed.) *"Semiconductor Nanophotonics - Materials, Models, Devices",* Chapter 1 - Submonolayer Quantum Dots, to be published by Springer Verlag, Series on Material Science, (2020).

Conference Proceedings

- B. Herzog, B. Lingnau, M. Kolarczik, S. Helmrich, U. Woggon, K. Lüdge, and N. Owschimikow. *"Role of Mixed-dimensional Excitons in Phase Dynamics of Semiconductor Lasers based on InAs(Sb)/GaAs Submonolayer Quantum Dots,"* Conference on Lasers and Electro-Optics (CLEO), San Jose, CA, USA, paper JW2A.24 (2019).

- M. Kolarczik, A. Koulas-Simos, B. Herzog, B. Lingnau, S. Helmrich, K. Lüdge, N. Owschimikow, and U. Woggon. *"Heterodimensionally confined carriers in*

III-V semiconductor nanostructures in multidimensional spectroscopy," Conference on Lasers and Electro-Optics (CLEO), San Jose, CA, USA, paper FM3D.2 (2019).

- M. Kolarczik, K. Thommes, B. Herzog, S. Helmrich, N. Owschimikow, U. Woggon. *"Ultrafast photonics in coherently coupled III-V semiconductor nanostructures,"* Proc. SPIE 10638, Orlando, FL, USA (2018).

- B. Herzog, M. Kolarczik, S. Helmrich, B. Lingnau, K. Lüdge, J.-H. Schulze, U. Pohl, A. Strittmatter, O. Brox, M. Weyers, N. Owschimikow, U. Woggon, *"Exciton dynamics and state splitting in antimony-doped InAs submonolayer agglomerations,"* Fundamental Optical Processes in Semiconductors (FOPS), Stevenson, WA, USA (2017).

- B. Herzog, M. Kolarczik, Y. Kaptan, B. Lingnau, K. Lüdge, J.-H. Schulze, R. Rosales, D. Bimberg, A. Strittmatter, U. W. Pohl, U. Woggon, and N. Owschimikow. *"Fundamental and Applied Aspects of Submonolayer Quantum Dots as Active Medium in Opto-electronics",* 42nd European Conference on Optical Communications (ECOC), Düsseldorf, Germany, (2016).

- B. Herzog, M. Kolarczik, Y. Kaptan, U. Woggon, N. Owschimikow, B. Lingnau and K. Lüdge. *"Carrier relaxation pathways in submonolayer quantum dots",* Conference on Lasers and Electro-Optics (CLEO), San Jose, CA, USA, paper JTu5A.70 (2016).

- M. Kolarczik, B. Herzog, C. Ulbrich, Y. Kaptan, U. Woggon, N. Owschimikow, A. Singh, X. Li, Y. Zhu, D. v. Thourhout, P. Geiregat, and Z. Hens. *"Biexciton-mediated modulation response of colloidal quantum dots deposited on a silicon nitride waveguide at high laser excitation rate",* Conference on Lasers and Electro-Optics (CLEO), San Jose, CA, USA, paper JTu5A.44 (2016).

Contents

1. Introduction

1.1. Semiconductor Nanostructures

Since the development of advanced epitaxial methods and the accompanying development of semiconductor nanostructuring, the field of photonic technologies started its triumphant march. By means of two-dimensional quantum well (QW) and zero-dimensional quantum dot (QD) semiconductor heterostructures a number of highly engineered optoelectronic devices have been fabricated, enabling low-cost and efficient light emitters for multiple fields of applications. In particular replacing microwave electronics for data transmission by optical transmission lines, a growing demand has risen for fast and efficient light emitters and detectors.

In general, an optical data transmission link consists of three components: the transmitter, a transmission medium and the receiver. While the transmission takes place within optical fibers, the transmitting and receiving units are realized by optoelectronic components such as semiconductor lasers, modulators, amplifiers and photodetectors, where the combined bandwidth is typically limited by the dynamics of the transmitting unit. For suitable media for the active zone of these laser diodes, nanostructured semiconductor materials such as QWs, rods, or QDs are of preferred choice. While the former provide large gain and convenient tunability, the latter enable fast charge carrier dynamics, low threshold current density, and good temperature stability.

1.2. Novel Gain Media for III-V Optoelectronics

Within the framework of this thesis an alternative approach aiming to combine the advantages of 0 D and 2 D nanostructures has been investigated, namely the *submonolayer* (SML) grown QDs. Since their first proposal in 1994 by Egorov et al. [11], a number of works has been published, showing successful implementation of
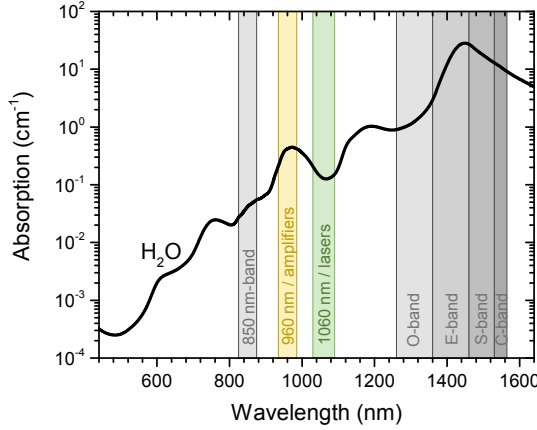
Figure 1.1: Absorption coefficient of liquid water, data taken from Ref. [10]. Gray areas mark transmission windows used for optical communication, yellow and green areas mark the operating range of the devices presented in this work.

those QDs into semiconductor high power lasers [12, 13], disc lasers [14], detectors [15, 16], or solar cells [17]. Even first steps towards the realization of mode-locked lasers based on SML QDs have been demonstrated [18].

Despite the excellent gain properties found in SML QD based devices, this material is actually limited to a room temperature emission wavelength reported to date in the range between 900 nm [19] and 1180 nm [20]. Samples created and analysed for this thesis contain semiconductor optical amplifiers and lasers emitting around 960 nm [2–4] and 1060 nm [1], respectively, which is visualized in Figure 1.1. The figure shows the spectral absorption coefficient of liquid water, revealing several local minima for favored optical transmission. Windows for long-haul data transmission are indicated by gray areas, containing the historic 850 nm range and the commercially used bands of 1310 nm (O) and 1550 nm (C). However, for short-haul communication the choice of wavelength not dominated by transmission loss and devices working at other wavelengths, including 960 nm, exist.

In addition another favourable range, regarding the green area in Figure 1.1, is the local minimum of water absorption around 1060 nm, which in particular makes this range desirable for medical applications and sensing [21]. This wavelength window further contains the demand for energy-efficient replacement of Nd:YAG lasers.

1.3. Optical Communication with Chaotic Light

Leaving the field of linear device applications for optical communication or sensing, semiconductor lasers were found to demonstrate an extreme sensitivity to optical feedback and injection [22]. Often considered as nuisance, complex laser dynamics have gained the maturity to aim for novel applications. In particular, the creation of a chaotic light source and its use as broadband information carrier has been shown to

Figure 1.2: Concept of secure communication with synchronized chaotic laser sources. After [24].
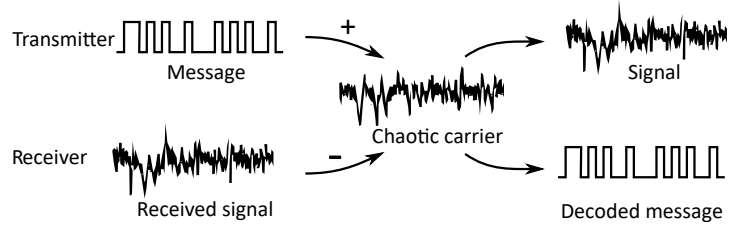
enable a high level of robustness and privacy for optical data transmission [23]. The idea of this type of encryption is sketched in Figure 1.2. For optical communication with synchronized chaotic lasers information is written on top of a chaotic carrier to create a signal, which then can only be decoded after correlation with the exact time-trace of the carrier [24].

Generally, the denotation *chaotic* describes time-dependent irregular phenomena that are derived by a deterministic rule with sensitive conditions. In other words systems which are able to change their states only after a small disturbance tend to behave chaotic. Regarding semiconductor lasers, such a system is found when exposing the laser to time-delayed optical self-feedback. As firstly described by Lang and Kobayashi [25], a certain ratio of delayed re-injected light into the cavity is able to undamp the laser's relaxation oscillations between its charge carrier reservoir and the light field. Thereby, the main nonlinearities to drive undamped oscillations into a chaotic state are the gain-coefficient κ and the amplitude-phase coupling in terms of Henry's α-parameter [26].

Regarding the latter, exceptionally large values for α were found in SML QD based devices within the framework of this thesis [1, 3], which is why a number of SML based lasers were taken to the lab of a group with broad knowledge about laser dynamics and complex systems. During a research stay at the Institute for Cross-Disciplinary Physics and Complex Systems (IFISC) in the group of Prof. Ingo Fischer the dynamics of SML QD based lasers subject to optical feedback were investigated and chaotic light was successfully created. The idea of the experiment is sketched in Figure 1.3, where an exemplary trace by means of (a) regular and (b) chaotic pulsations are plotted. The graphs show color-coded intensity traces of a self-feedbacked SML QD based laser with the bottom plane stretched by the time evolution and the roundtrip phase.
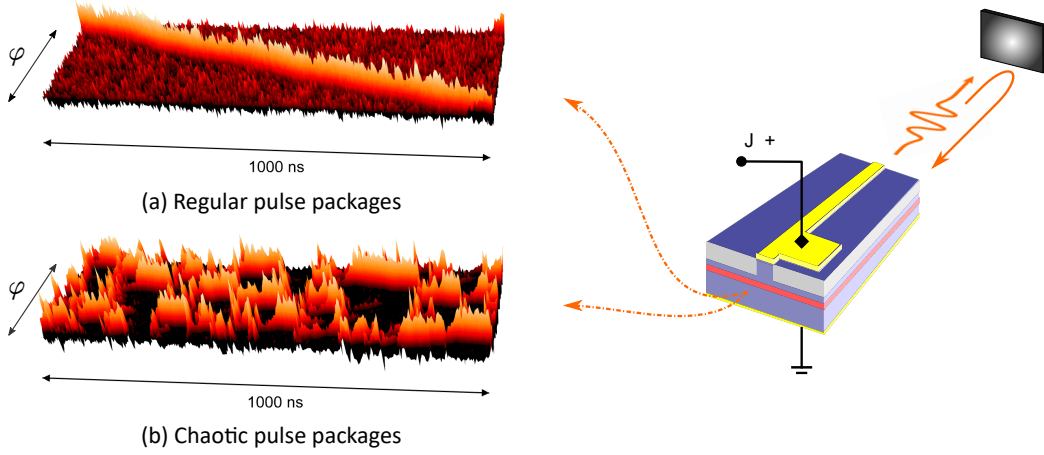
Figure 1.3.: Feedback-induced laser dynamics in terms of (a) regular and (b) chaotic pulsations.

Outline of this Thesis

The present work is divided into two parts. The first part contains fundamentals about semiconductor nanostructures, giving an introduction to growth and optical properties of SML QDs, as well as their role as active medium in optoelectronic components. Additionally, all experimental techniques that were applied within the framework of this theses will be introduced. Those comprise static methods, such as laser characterization and gain measurement, as well as dynamic methods ranging from direct electrical sampling up to all-optical sampling by means of heterodyne-detected pump probe spectroscopy.

The second part treats the application of SML QDs into optoelectronic devices. Optical semiconductor amplifiers containing SML QDs as active medium will be demonstrated, which revealed an ultra-fast gain recovery, accompanied by an unusually strong phase response. After modeling the gain dynamics via microscopically motivated rate equations by B. Lingnau, two distinct exciton states were revealed, denoted as *active* and *inactive* states. At last, SML QD based lasers will be demonstrated and exposed to delayed optical feedback, where the conditions for chaotic light generation will be determined.

Part I.

Samples and Methods

In the first part of this work a theoretical background will be given, including the introduction to submonolayer growth, semiconductor devices and laserdynamics. Further an introduction to the used measurement methods, as well as the investigated sample pool will be given. The samples were categorized into two types, denoted by their room temperature emission wavelength. The *960*-series containes a number of InAs/GaAs SML QD based semiconductor optical amplifiers, which were used for dynamics measurements, as published in Refs. [3] and [4]. The *1060*-series comprises lasers, amplifiers, and unprocessed wafer pieces of InAs/GaAs SML QDs alloyed with Sb, accompanied by similar processed reference samples containing unalloyed SML QDs, as well as a single QW and SK QDs.

2. Theoretical Background

Since the first semiconductor laser based on GaAs was developed in 1962 by R. N. Hall et al. [27], a large number of completely new applications have opened up. While in the beginning people struggled with high laser threshold current and low efficiency even at cryogenic temperature, the commercial usability of laser diodes has increased with the development of semiconductor heterostructures and the use of quantum confinement [28].

The most important emitters for modern optoelectronics are based on III-V compound semiconductors, comprising GaAs, InP, and GaN as most important substrates. Those materials exhibit a direct bandgap at $k = 0$, which is Γ point in k-space, thus enabling large radiative recombination probability. For these types of semiconductors the band structure $E(k)$ for the valence band (VB) and conduction band (CB) around Γ can be approximated by parabolic bands according to: [29]

$$E_C(k) = E_g + \frac{\hbar k^2}{2m_e^*} \qquad E_V(k) = -\frac{\hbar k^2}{2m_h^*}, \qquad (2.1)$$

with the effective mass m^* and the bandgap E_g. Regarding the carrier density of states (DOS) $D(E)$ this translates into a square root dependency with:

$$D_C(E) = \frac{(2m_e^*)^{3/2}}{2\pi^2\hbar^3}\sqrt{E - E_C} \qquad D_V(E) = \frac{(2m_h^*)^{3/2}}{2\pi^2\hbar^3}\sqrt{E_V - E}, \qquad (2.2)$$

which is only valid for bulk semiconductors where the motion of charge carriers is not restricted by spatial dimensions.

2.1. Quantum Confined Heterostructures

In contrast, if the carrier motion gets restricted in at least one spatial dimension quantum confinement effects arise and the effective DOS changes. For heterostructures with a low bandgap material embedded in a larger bandgap matrix, e.g., InAs in GaAs, this is the case when the inner spatial dimension is reduced below the carrier
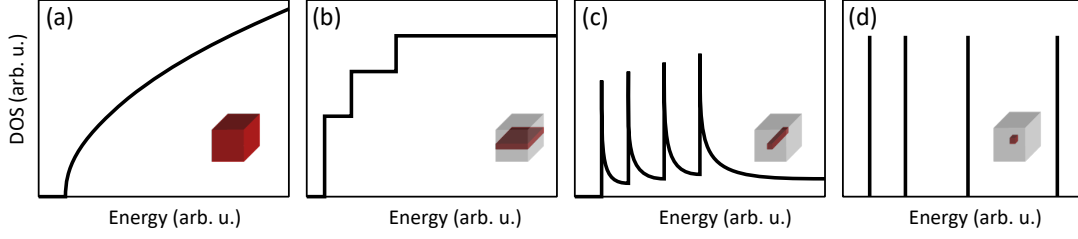
Figure 2.1.: Modification of the (a) bulk semiconductor density of states by reduction of the dimensionality, leading to (b) 2 D quantum well, (c) 1 D quantum wire, and (d) 0 D quantum dot structures. After [30].

de Broglie wavelength, given by: [29]

$$\lambda_{deBroglie} = \frac{2\pi\hbar}{\sqrt{2m^*E}} \, . \tag{2.3}$$

For the aforesaid main III-V semiconductor materials $\lambda_{deBroglie}$ ranges in the order of 7 to 70 nm.

The thus created nanostructures are categorized by their confinement dimension, as sketched in Figure 2.1 as 2 D quantum well (QW), 1 D quantum wire, and 0 D quantum dot (QD) structures [30]. For these structures the square-root shaped bulk DOS from Equation 2.2 gets modified to a step function for 2 D confinement up to discrete states in case of 0 D QDs.

2.1.1. Submonolayer Quantum Dots

The SML growth technique has been developed in 1994 by A. Egorov et al. [11], who originally aimed for an alternative QW growth. In the course of fundamental studies on the material properties signatures of fully confined excitons were found within those SML-grown QW structures. In 1995 M. Belousov et al. [31] proposed the SML QD growth technique via cycled deposition of sheets of InAs into GaAs matrix, leading to vertically correlated islands, which form agglomerations for carrier recombination.

After the first publication of a high power SML QD laser, realised by the group of the later Nobel prize winner Z. Alferov [12], numerous studies on fundamentals and applications of this material were performed. They established that the biggest advantage of SML QDs, as compared to self-assembled grown QDs after Stranski and Krastanov (SK), are the larger gain and quantum efficiency, which is highly beneficial for laser fabrication [13].

A major part in SML QD research was performed by Zhangcheng Xu in the group

of Jørn M. Hvam at the TU of Denmark in Lyngby, who found a transfer from QD to QW emission in μ-PL measurements in 2003 [32]. Those were addressed to the coexistence of localized and delocalized exciton states [33, 34], which the autors also assumed to cause the oberseved narrow and large modal gain in SML QD lasers [35].

With the beginning of the collaborative research center (CRC) 787 *Semiconductor Nanophotonics* located mainly at the TU Berlin, the investigation of SML QDs as active medium for optoelectronic applications gained renewed attention. Within the framework of this CRC, studies on the atomic structure were performed via cross-sectional scanning tunnelling microscopy, revealing features of a laterally inhomogeneous In distribution, containing InAs-rich agglomeration centers [36, 37]. These centers were found to be mainly caused by In-segregation into the GaAs matrix and act as shallow localization centers for exctions [38]. Additionally within the CRC 787 SML QD based vertical-cavity surface-emitting lasers (VCSELs) with high temperature stability and large modulation bandwidth were successfully reported [39] and also SML QD based disk lasers could be realised [14, 40].

Latest research on SML QDs also includes the further development of the growth technique by adding antimony to the InAs sheets[20, 41], which will be treated later in more detail. Also attempts for the application of SML QDs as infrared photodetectors [42, 43] and solar cells [44] were published.

The epitaxial structures of a typical InGaAs QW and InAs/GaAs SML QDs are sketched in Figure 2.2 (a) and (b), respectively. While QW structures are typically grown as homogeneously distributed InAs and GaAs composition with at a few tens of ML height, SML QDs are created via cycled deposition of InAs SML sheets embedded into a GaAs matrix, as mentioned before. The induced local strain thereby leads to correlated In-rich regions, which are marked as dashed lines in the figure.

Since In-adatoms tend to segregate during InAs growth on GaAs due to the larger lattice constant of InAs as compared to the GaAs matrix, an increase of the material contrast between In-rich and In-poor areas is a challenging issue.

The alloy with Antimony (Sb) has been first demonstrated by Quandt et al. in 2015 [41], with the aim to push the emission of SML QD structures towards longer wavelengths. In their work the authors proposed an SML QD growth where in between each cycle of SML deposition a flush of Sb atoms by means of triethylantimony (TESb) during MOVPE growth was added with the nominal amount of up to 14 μmol. This leads to a reduction of the In mobility and thus enables the formation of islands
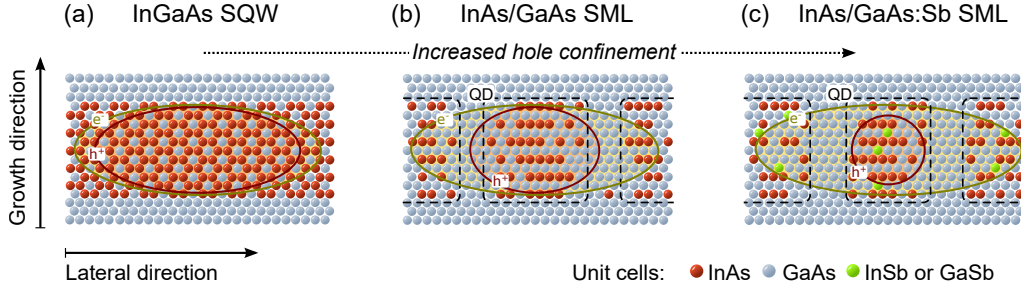
Figure 2.2.: Schematic structure of the (a) SQW, (b) SML and (c) SML:Sb active media embedded into a GaAs matrix (not to scale). Red circles sketch the wavefunction of the lowest electron state and green circles the respective heavy hole distribution [1].

with higher In-content gradients and reduced volume expansion [42], thus enhancing the carrier localization [45]. Since the Sb relative amount in the structures is in the order of a single-digit percentage, the term Sb *alloy* rather than Sb doping is used. While originally, Sb was used as a surfactant to improve the interface of a InAs/GaAs heterostructure [46], the relatively large Sb atoms in case of SML growth have been found to cause a shrinkage of the In-rich agglomerations, since In atoms tend to cluster to the Sb. After comparison to 8-band k · p modelling of different Sb distributions, implemented by A. Schliwa at TU Berlin, it was found that the Sb incorporates and clusters mainly within rather than adjacent to the QDs [41]. This leads to a redshift due to the lower bandgap of either GaSb or InSb bulk material. A sketch for the epitaxial structure of SML:Sb QDs is given in Figure 2.2 (c). In addition even though a GaAs/GaSb heterostructure is known to show a type-II band alignment [47, 48], the Sb-alloyed SML structures (SML:Sb) still exhibit a type-I alignment but with enhanced hole localization energies [41].

Heterodimensional charge carrier confinement denotes a difference in the dimensionality of electron and hole wavefunctions within the active region of quantum confined semiconductor structures. In SK QDs attached to a QW (DWELL) this was revealed by means of *crossed excitons*, which in addition to the QD and QW eigenstates represents a mixed state with one carrier confined in the QD and the conjugate carrier in the QW [7, 49]. While for DWELL structures this is just a minor effect, S. Harrison et al. [50] found that the majority of SML QD excitons comprise heterodimensional carrier confinement.

In their studies the authors performed magneto-PL experiments, where they used a magnetic field to stretch the excitons and to create an anisotropy, which they where able to access via PL measurements [50]. Thus the electron wavefunction has been found to extend over several In-rich agglomerations, while the hole wavefunction was
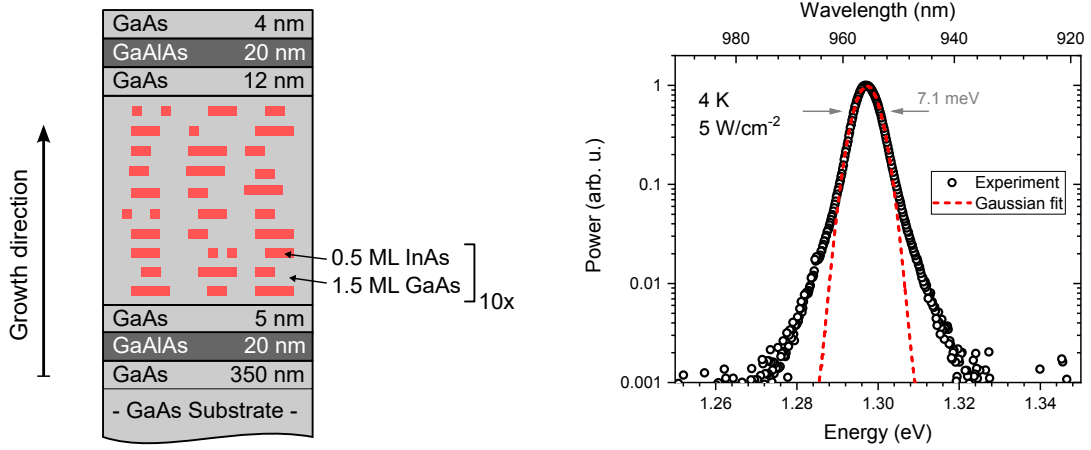
Figure 2.3.: (a) Typical epitaxial layer structure of a submonolayer quantum dot layer, embedded in a AlGaAs/GaAs waveguide heterostructure. (b) Gaussian peak fit of a typical submonolayer quantum dot photoluminescence spectrum, recorded at 4 K sample temperature and low excitation density.

limited to the island size, marked with green and red ellipses in Figure 2.2, respectively. This effect is referred to as *heterodimensional confinement*, indicating that features of 0 D and 2 D confinement were observed.

2.1.2. Optical Properties

The SML QD laser structure from Zhukov et al. was realised by 13 layers of 0.5/2.3 ML InAs/GaAs SML QDs and reached up to 1.4 W output power, centerd at 1034 nm [12]. Since it has been found that the nominal amount of InAs layer size, accompanied with the GaAs buffer size and cycle number play important roles for the optical properties of the material, the growth protocols always have to be indicated when comparing results obtained from different samples. In particular, luminescence studies on a 10x0.5/1.5 ML structure showed signatures of carrier heteroconfinement [50], as stated before, as well as a density of InAs-rich agglomeration centers in the order of 10^{12} cm^{-2} [37].

Generic optical properties of SML QDs are demonstrated in Figure 2.3 (a), using a typical SML structure, formed by a tenfold cycled deposition of 0.5/1.5 ML InAs/GaAs, thus representing a standard growth protocol for SML QDs. The photoluminescence lineshape of this structure at low temperature was found to be mainly Gaussian distributed with a linewidth of $\Delta E = 7.1$ meV and covering 94 % of the luminescence intensity, which is is sketched in Figure 2.3 (b). This further lets assume that the exciton recombination takes place at the site of the less mobile carrier, formed by the 0 D confined holes.
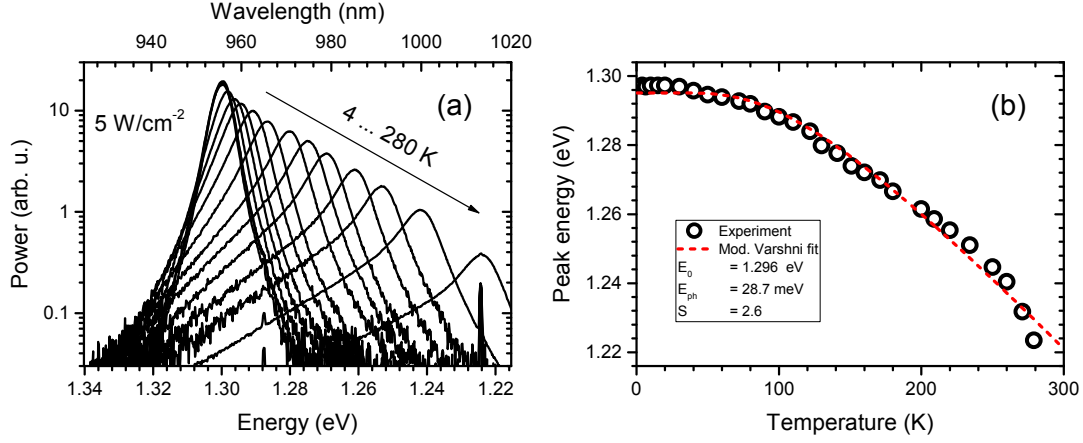
Figure 2.4.: (a) Photoluminescence spectra of a typical SML QD sample for temperatures increasing from 4 to 290 K after optical excitation into the GaAs barrier at an intensity of 5 W/cm^2. (b) Temperature development of the peak energy and application of two empirical models for bandgap fitting.

The bandgap temperature dependence   of the sample discussed in the previous subsection is shown in Figure 2.4. The development of the luminescence with increasing temperature from 4 to 290 K after optical excitation into the GaAs barrier has been analyzed. A peak shift description for the phonon-induced bandgap shrinkage in semiconductors has been provided by O'Donnell and Chen [51], who derived a modification of the Bose-Einstein model for the bandgap energy E_g to read:

$$E_g(T) = E_g(0) + S\langle\hbar\omega\rangle[\coth(\langle\hbar\omega\rangle/2k_BT) - 1], \tag{2.4}$$

where the average phonon energy $\langle\hbar\omega\rangle = E_{ph}$ and the dimensionless parameter S are fit parameters carrying an immediate physical meaning with the latter describing the phonon coupling strength as inspired by the Huang Rhys factor. The fit is shown in Figure 2.4 (b) as red dashed lines, which yields the parameters $E_{ph} = 28.7$ meV and $S = 2.6$. Both parameters are close to the GaAs literature values with $E_{ph,GaAs} = 35.3$ meV and $S_{GaAs} = 3$ [51].

2.2. Semiconductor Optoelectronic Devices

The application of SML QDs as gain medium for optoelectronic light emitters requires both, the embedding of the active medium into an optical waveguide, as well as establishing a link to electrical contacts for current injection. Typically both is provided by the design of a separate confinement heterostructure (SCH).

(a) DOS and occupation   (b) Hetero-junction
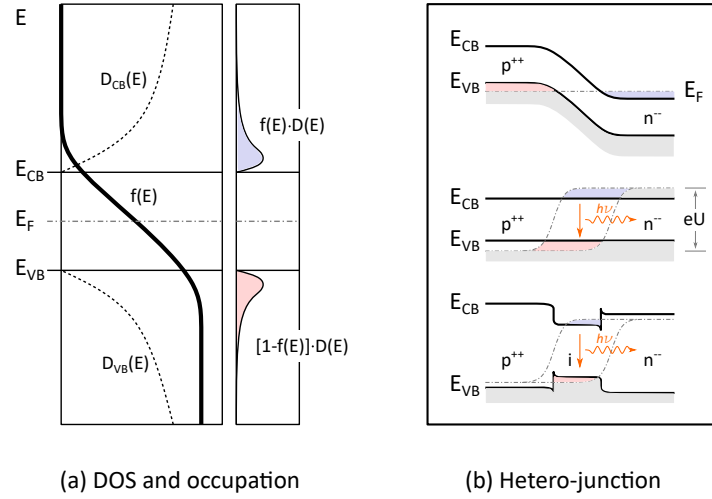
Figure 2.5.: Fermifunction $f(E)$, density of states (D), and occupation probability for electrons $f \cdot D$ or for holes $(1 - f) \cdot D$ in a semiconductor. (b) From top to bottom: pn-junction at thermodynamical equilibrium; pn-junction under forward bias condition eU; pn-junction with additional intrinsic separate confinement region under forward bias condition eU. CB: conduction band, VB: valence band. After [29].

2.2.1. PIN Diodes

In general the carrier occupation probability of the valence band (VB) and conduction band (CB) in semiconductors is given by the Fermi-Dirac distribution $f(E)$: [29]

$$f(E) = \frac{1}{\exp \frac{E - E_F}{k_B T} + 1} , \tag{2.5}$$

with the temperature T dependent Fermi Energy E_F and the Boltzmann constant k_B. For an intrinsic direct bandgap semiconductor $f(E)$, the DOS (D), and the occupation probability for electrons $f \cdot D$ or for holes $(1 - f) \cdot D$ are sketched in Figure 2.5 at a temperature $T > 0$, revealing a small amount of thermally activated carriers. Since the amount of those is typically not enough for efficient room temperature carrier transport, the conductance can be increased via doping. This is achieved by introducing electrically active impurities into the material, creating either donor (n) or acceptor (p) states. While for intrinsic, meaning undoped, semiconductors E_F is roughly located in the middle of the band edge, it is shifted towards the CB in case of n-doping or towards the VB in case of p-doping [29].

Most optoelectronic devices are realized as a junction of p- and n-doped semiconductors. When bringing two semiconductors of identical bandgap but different doping close to each other, thus creating a homo-junction, the respective Fermi levels align under thermodynamic equilibrium. This leads to band bending, as it is demonstrated

in the upper sketch in Figure 2.5 (b), forming a barrier for carrier motion, accompanied by charge carrier depletion in the junction region.

As sketched in the middle of Figure 2.5 (b), this barrier can be overcome after application of a forward bias eU, thus lifting E_F in the n-region, while lowering it in the p-region. To be precise, the specification of a E_F only holds for thermodynamic equilibrium, which is why under external bias the term *quasi*-Fermi energy is used. The depleted region in this case contains an overlap of electrons and holes, enabling them to radiatively recombine. [29]

In order to increase the electron-hole overlap, an intrinsic lower bandgap material can be applied into the intrinsic region, as demonstrated in the bottom sketch of Figure 2.5 (b). This leads to enhanced carrier confinement and consequently to an increase of the recombination probability. For an SCH structure this material is also embedded into an optical waveguide.

2.2.2. Lasers and Superluminescence Diodes

The realization of a semiconductor laser (SCL) is performed by applying a cavity to the SCH structure, described above, in order to enable stimulated emission. Typical geometries are vertical or edge-emitting cavities, but also external cavities exist.

In case of Fabry Pérot (FP) edge-emitting SCLs, the resonator is given by the cleaved edges of the waveguide. According to the selection rules, all longitudinal laser modes need to satisfy the resonator condition according to:

$$\nu = \frac{c}{2Ln} \cdot m \, , \tag{2.6}$$

with the cavity length L, the refractive index n, and the mode number m.

Superluminescence   denotes the transition region where the SCL output characteristic changes from spontaneous to stimulated emission, translating into a *kink* in the light-current curve. When driven in this specific mode, the output power rises significantly, while at the same time the broad spectral bandwidth is maintained with the latter leading to a relatively short coherence length L_C.

For certain applications such as, e.g., optical coherence tomography (OCT), bright light sources with short-coherence length are essential, since the spatial resolution of this imaging technique is mainly determined by L_C [21]. Generally sources of short

coherence require a broad gain spectrum $\Delta\lambda_G$ with both quantities linked via:

$$L_C = \frac{\lambda_0^2}{\Delta\lambda_G} \, . \tag{2.7}$$

The best light source combining both properties are supercontinuum fiber lasers, providing several hundreds of nm bandwidth at above mW power levels. These sources, however, are very cost-intensive and relatively large, making them applicable mainly for lab rather than commercial usage. A good alternative thus is represented by superluminescent diodes (SLDs). Those devices resemble typical SCLs regarding their epitaxial structure, but are optimized for superluminescence operation with main differences affecting gain medium and facet reflectivity [52].

Regarding the NIR spectral range commercial devices usually contain stacks of chirped nanostructures, such as MQWs [53], SK QDs [54] or even a combination of both [55]. *Chirping* in this case means stacking of layers with shifted transition energies, which is engineered via tuning of material composition and confinement energy. This leads to an extreme increase of the emission bandwidth as compared to a homogeneous layer structure. To this end self-assembled QDs are a material of major interest, since such layers produce an intrinsic large emission bandwidth due to inhomogeneous broadening.

Further, engineering of the facet reflectivity is the second key to superluminescence operation. While in case of SCLs a large facet reflection enables high stimulated emission rates and thus narrow linewidth lasing, the opposite is desired in case of SLDs. However depending on the cavity feedback a trade-off between output power and bandwidth needs to be found, as lower feedback translates into lower output due to lower carrier recombination rates.

2.2.3. Optical Amplifiers

The invention of bulk SOAs took place soon after the SCL development [57]. In contrast to the SCL emission, SOAs are designed for coherent light amplification, necessary for, e.g., long transmission lines. As a main difference the facet feedback is adverse and thus suppressed to ensure a single transmission without reflection. Mainly this is achieved via anti-reflection (AR) coating and facet tilt, which is sketched in Figure 2.6 (a) as top view on an SOA.

The reflectivity of transverse electric (TE) polarized light after Fresnel's law can be
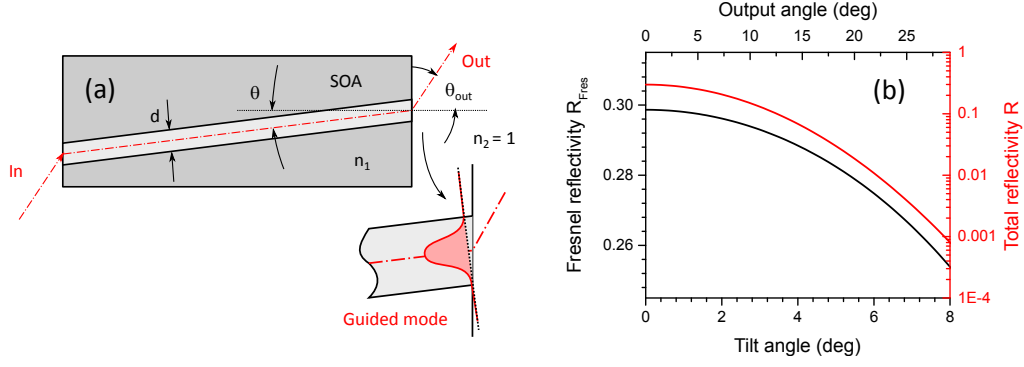
Figure 2.6.: (a) Top view of the tilted waveguide of an SOA. (b) calculated facet reflectivity over the tilt angle considering only TE Fresnel reflection (black) and a Gaussian distributed waveguide mode with $w = 1.7 \, \mu m$ (red). After [56].

described via: [58]

$$
R_{Fres}(\theta) = \frac{n_1 \cos\theta - n_2 cos\theta_{out}}{n_1 \cos\theta + n_2 cos\theta_{out}} \stackrel{n_2=1}{=} \left(\frac{\cos\theta - n_1 \sqrt{n_1 - \sin^2\theta}}{\cos\theta + n_1 \sqrt{n_1 - \sin^2\theta}} \right)^2 , \qquad (2.8)
$$

which is calculated in Figure 2.6 (b) for a GaAs waveguide in air ($n_1 = 3.4$, $n_2 = 1$) and tilt angles θ ranging from 0 to 8°. Suffice it to recall here, that the calculation is limited to TE guided light, which applies for most SOAs in use.

The plot reveals a reflection reduction from 30 % to 25 %, equivalent to 1 dB, which would be not sufficient for application. Additionally also the spatially distributed mode profile has to be considered, which leads to misalignment of the reflected phase fronts [59] and has a big effect already at few degrees of waveguide tilt. For a Gaussian TE waveguide mode $E_y = A_y \, \exp(-y^2/w_y^2)$ with the amplitude A_y and the mode width w_y the Fresnel reflectivity gets scaled by an additional term to read:

$$
R(\theta) = R_{Fres}(\theta) \exp\left[-\left(\frac{2\pi n_2 w\theta}{\lambda} \right)^2 \right]. \qquad (2.9)
$$

The full facet reflectivity has been calculated for a mode width of $w = 1.7 \, \mu$m, which is a typical value for a GaAs-based 4 μm wide ridge waveguide, and is plotted in Figure 2.6 (b) as red line. Note that due to the exponential term in Equation 2.9 the reflectivity drops on a logarithmic scale and reaches values down to -30 dB ($R =0.001$) for an 8 ° waveguide tilt.

A further reflection reduction is achieved by dielectric coating of the facet. By adding only few AR-layers of e.g. TiO$_2$/SiO$_2$ with an optical thickness of $n \cdot d = \lambda/4$, the reflectivity can be further decreased by more than 30 dB.

Linear signal amplification in optical amplifiers generally happens via stimulated emission of light propagating through an optically active waveguide after its inversion. Besides SOAs, doped fibers and Raman amplifiers represent established ways for coherent light amplification.

After their invention in the 90s Er-doped fiber amplifiers (EDFAs) became first choice for long-haul linear amplifiers due to their low noise and high gain properties as compared to the bulk-SOAs at that time. Similar to the SCLs, SOAs experienced a big improvement after the application of nanostructured semiconductors in terms of QWs and SK QDs, where in particular the former enabled much larger gain and efficiency. For linear operation such as boosters, in-line amplifiers or preamplifiers, today ED-FAs are still first choice in case of long haul application. However due to their cost effectiveness and possibility for integration, SOAs are mainly used in metro networks [56].

Nonlinear Operation exceeds the classic amplification scheme and enables multiple ways of all-optical data processing. Due to their higher nonlinearity and ultrafast gain recovery dynamics, SOAs are first choice in this field. Mainly in this mode the gain and phase of transmitted pulses are self- or cross modulated [60].

Regarding one propagating signal, a nonlinear gain response can cause self-gain modulation (SGM) due to saturation or spectral hole burning. A nonlinear response of the effective refractive index leads to self-phase modulation (SPM) and causes chirp and waveform shaping. In terms of multiple signals both effects can crosstalk and lead to cross-gain modulation (XGM) or cross-phase modulation (XPM), which are used for e.g. multiplexing, wavelength conversion, or all-optical switching. Further signals may even cause beating along the waveguide and generate light at new optical frequencies, which is called four-wave mixing (FWM) and used for e.g. optical gates [56].

The SOA Gain G in general is defined as the input-output power ratio of an optical pulse with power P. Assuming a positive and linear amplification in terms of a constant modal gain g along the z-axis, the electrical field after a propagation of the length L can be described by:

$$G = \frac{P_{in}}{P_{out}} \quad \Rightarrow \quad \frac{dP}{dz} = gP \quad \Rightarrow \quad G = \exp(gL). \tag{2.10}$$

Considering saturation and spectral dependence as $g = g(\omega, P_{in})$ the description of this parameter can reach a high degree of complexity depending on the amplifying material. However, regarding a single optical transition as homogeneously broadened
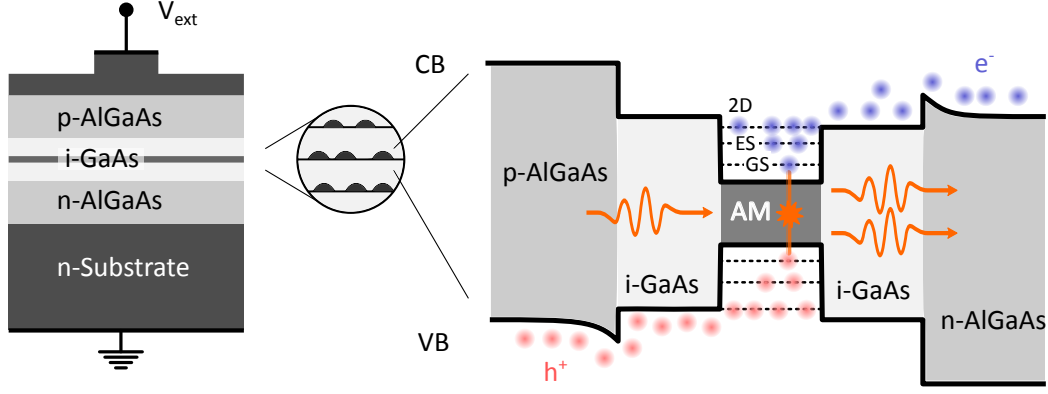
Figure 2.7.: Left: simplified epitaxial layer structure of an SK QD based SOA in front view. Right: energy band diagram under forward bias condition including carrier reservoir and QD states. ES: excited state, GS: ground state, CB: conduction band, VB: valence band, AM: active medium. After [56].

two-level system with the transition frequency ω_0 and the dipole relaxation time τ a commonly used model is:

$$g(\omega, P) = \frac{g_0}{1 + (\omega - \omega_0)^2 \tau^2 + P/P_{sat}}, \qquad (2.11)$$

with the maximum gain g_0 and the saturation power P_{sat}. In case of small input signals $P_{in} << P_{sat}$ this equation collapses to a Lorentzian shaped gain spectrum:

$$g(\omega) = \frac{g_0}{1 + (\omega - \omega_0)^2 \tau^2}. \qquad (2.12)$$

Apparently due to the exponential relation of g and G, the SOAs gain bandwidth Δg is smaller than the modal gain bandwidth ΔG and even decreases for longer cavities [56].

Quantum dot amplifiers, based on SK QDs as active medium were object of numerous fundamental and applied studies. While the exciton DOS in those dots represents a reliable test object for studies on two level systems, an excellent performance with respect to gain recovery dynamics and noise as compared to QW SOAs has been achieved.

As sketched in Figure 2.7 the amplification in SK QD SOAs typically takes place at wavelengths resonantly to the ground state (GS) exciton transition. After stimulated recombination and consequently carrier depletion the GS gets refilled by fast carrier relaxation from the excited state (ES) and the 2D carrier reservoir (either a QW or the wetting layer). Due to the strong localization in SK QDs, this process typically
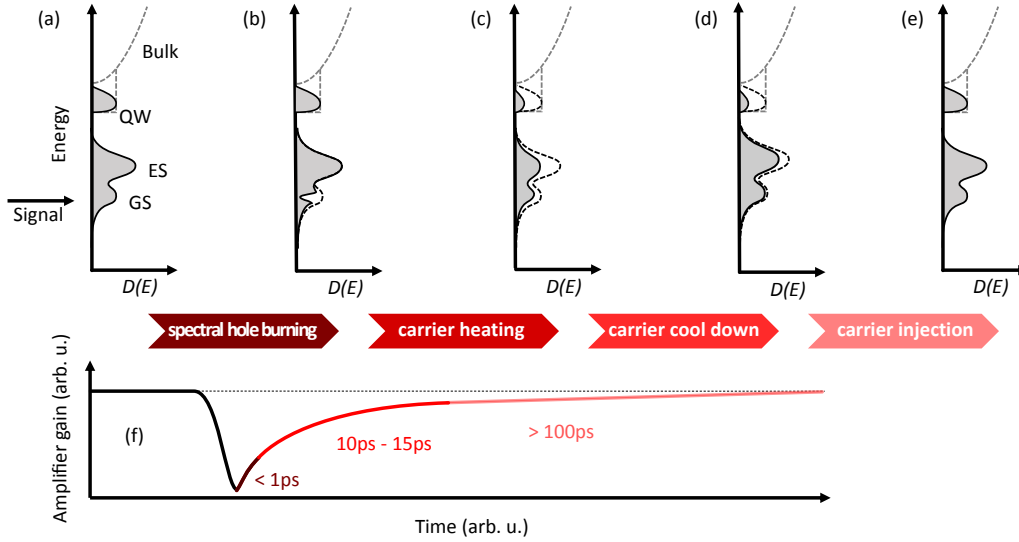
Figure 2.8.: Gain recovery of an SK QD-in-a-well SOA after amplification of a short optical pulse in spectral resonance to the QD ground state. Dashed lines mark the DOS $D(E)$, gray areas represent the occupation $N(E)$.

happens on a single-digit ps time scale and enables very fast recovery dynamics [61]. In Figure 2.8 a typical pulse amplification process of an SK QD SOA is sketched [56]. The optical signal depletes the exciton GS (a) and burns a spectral hole in the carrier distribution (b). This non-equilibrium state is overcome by mainly carrier-carrier scattering heating up the lattice (c) and cooling down again through phonon emission (d) up to the original distribution. Via carrier injection from the reservoir the DOS gets finally refilled evenly (e).

This full cycle typically happens on a time scale of 100 ps, as sketched in Figure 2.8 (f). However, light-matter interaction and carrier heating are processes on a fs-time scale, while the phononic cool down takes two-digit ps and the reservoir-induced refilling even one order of magnitude in time longer.

2.2.4. Quantum Dot Carrier Dynamics

In order to gain deeper understanding in the amplification process of SK QD SOAs numerous model systems have been designed based on multiple level rate equations capturing inter- and intraband processes within the active medium [62, 63]. As sketched in Figure 2.7 the simplest model would consider the carrier number of three respective levels: the QD GS N_{GS}, involved in the amplification process, the ES N_{ES} acting as fast and small carrier reservoir and the slow but large 2D reservoir N_{Res}. Note that the reservoir can be formed either by a grown QW surrounding the
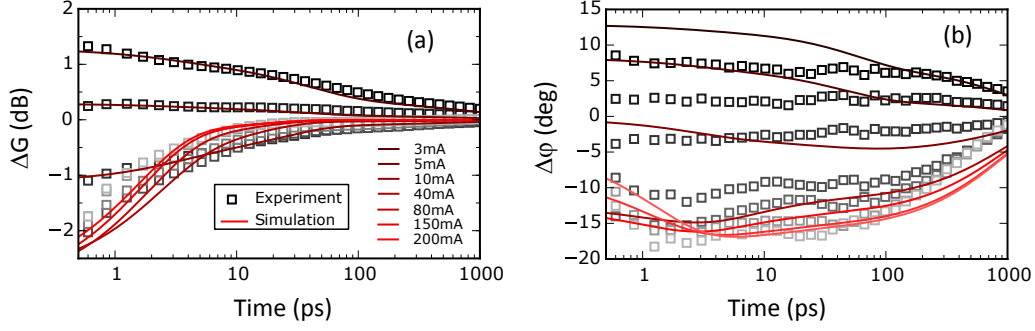
Figure 2.9.: Typical (a) gain and (b) phase recovery traces of an SK QD SOA modeled via microscopically motivated rate equation system. Experimental data has been obtained from time-resolved pump probe measurements [2].

QDs or the WL itself, as explained earlier in section 2.1.

Generally all population changing processes can be described by means of transfer rates R_x^j, which combine population numbers and their lifetimes $R_x^j = \sum_i^j N_i^j / \tau_i^j$. In QD based devices the carrier relaxation cascade happens by electrical pumping the reservoir R_{pump}, where they either recombine spontaneously with R_{spont}, stimulated with R_{stim} or feed the QD states with R_{cap}. Additional back scattering R_{esc} of carriers might be possible as well due to thermal escape or Auger processes. The same processes except for the electrical pumping account for the QD states as well. For a number of dots j within a distribution f_j the rate equation system condenses into: [64]

$$\frac{\partial}{\partial t} N_{Res} = R_{pump} - R_{spont}^{Res} - R_{stim}^{Res} - \sum_j f^j (R_{cap}^j - R_{esc}^j) \tag{2.13}$$

$$\frac{\partial}{\partial t} N_{ES}^n = (R_{cap}^j - R_{esc}^j) - R_{rel}^n - R_{spont}^{j,ES} - R_{stim}^{j,ES} \tag{2.14}$$

$$\frac{\partial}{\partial t} N_{GS}^j = R_{rel}^j - R_{spont}^{j,GS} - R_{stim}^{j,GS} \tag{2.15}$$

For simplification the capture process into the dots is only considered to take place into the QD ES state, rather than the GS. The latter is then only fed by its corresponding ES via carrier relaxation R_{rel}, which in most cases represents a reasonable approximation. Further, stimulated emission and absorption share the same rates with the sign depending on the inversion of the state occupation. Since the entire active layer contains a rather large dot number j, it is common to merge multiple dots into a finite amount of ensembles with similar transition energies $\hbar\omega_{(}^j GS, ES)$.

In this work a theoretical analysis of carrier dynamics was performed in collaboration with B. Lingnau from the group of K. Lüdge at the TU Berlin. The basic model was developed for DWELL structures, assuming a Gaussian dot distribution with: [2]

$$f^j = \mathcal{N}^{-1} \exp\left[-4\ln 2 \left(\frac{\hbar \omega_{GS}^j - E_{GS}}{\Delta E_{inh}^{GS}}\right)^2\right], \tag{2.16}$$

in order to scale the respective capture rates from the reservoir into the QD ES from the n-th subensemble. Considering the current J as pump rate into the reservoir with the lifetime τ_{Res}, leading to $N_{Res}/\tau^{Res} = R_{spont}^{Res} + R_{spont}^{Res}$, the full system can be expanded to read:

$$\frac{\partial}{\partial t} N_{Res} = J - \frac{N^{Res}}{\tau_{Res}} - 4N^{QD} \sum_j f^j R_{ES}^{cap}(j) \tag{2.17}$$

$$\frac{\partial}{\partial t} N_{ES}^j = -\frac{(N_{ES}^j)^2}{\tau_{ES}} + R^c a p_{ES}(j) - \frac{1}{2} R^{rel}(j) - R_{ES}^{j,stim} \tag{2.18}$$

$$\frac{\partial}{\partial t} N_{GS}^j = -\frac{(N_{GS}^j)^2}{\tau_{GS}} + R^{rel}(j) - R_{GS}^{j,stim}. \tag{2.19}$$

Since rate equation systems typically contain a high number of parameters, it is necessary to analyze dependencies in order to strengthen the respective physical interpretation. To this end Lingnau et al. use a microscopic model to obtain the capture rates $R_{ES}^{cap}(j)$ [8, 65].

With this full entity the complex dynamics of an SK QD SOA by means of gain and phase dynamics can be captured in good approximation, as it is shown in Figure 2.9.

2.2.5. Linewidth Enhancement

As shown in Figure 2.9 (b) an entering pulse into an SOA not only affects its gain, but also causes changes in the effective refractive index. Following the Kramers-Kronig relations for material dispersion, the real and imaginary part of the electric susceptibility χ and therefore the refractive index $n(\omega)$ and gain $g(\omega)$ can be directly related to each other: [2]

$$\Delta n(\omega) \propto \int \frac{g(\omega')}{\omega - \omega'} d\omega'. \tag{2.20}$$

A single optical transition as in, e.g., atom gases can be simply described by the Lorentzian oscillator model with the complex dielectric function $\varepsilon(\omega)$, calculated
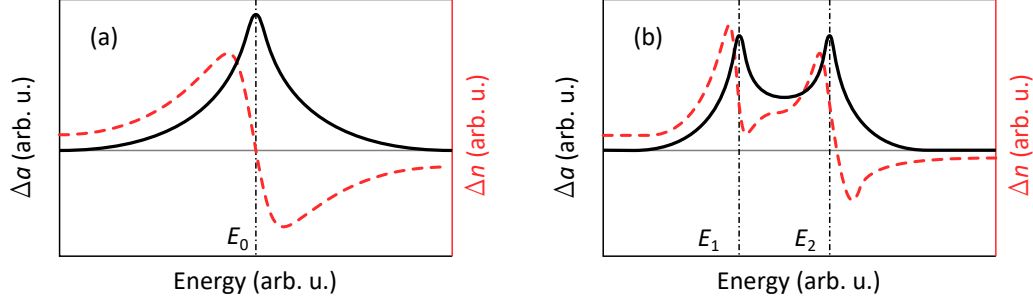
2. Theoretical Background

Figure 2.10.: (a) Complex susceptibility in terms of changes in the absorption $\Delta a \propto Re\,(\varepsilon)$ and refractive index response $\propto \Delta n \propto Im\,(\varepsilon)$ of an electric dipole with its resonance at $E_0 = \hbar\omega_0$. (b) The same quantities for two dipole transitions with resonances E_1 and E_2.

via:

$$\varepsilon(\omega) = +\frac{Ne^2}{\varepsilon_0 m_0} \frac{1}{\omega_0^2 - \omega^2 - i\gamma\omega}\,, \tag{2.21}$$

where N is the number of transitions per unit volume and e_0/m_0 is the electron charge-to-mass ratio. Separation into real and imaginary part delivers the absorption enhancement Δa and the refractive index shift Δn of that transition given by:

$$Re(\varepsilon) = \Delta a = 1 + \frac{Ne^2}{\varepsilon_0 m_0} \frac{\omega_0^2 - \omega^2}{(\omega_0^2 - \omega^2)^2 + \beta^2 \omega^2} \tag{2.22}$$

$$Im(\varepsilon) = \Delta n = \frac{Ne^2}{\varepsilon_0 m_0} \frac{\beta\omega}{(\omega_0^2 - \omega^2)^2 + \beta^2 \omega^2}\,, \tag{2.23}$$

with the damping β. As sketched in Figure 2.10 (a) at the resonance Δa is maximized, while Δn shows a zero crossing. When adding multiple transitions the single dielectric functions sum up and form an effective background with multiple resonances, where Δn differs from zero at the resonance peaks, which is sketched in Figure 2.10 (b). Since the $Im(\varepsilon)$ decays slower than the real part, off-resonant transitions will cause a phase-shift, even though the amplitude remains effectively unchanged.

In contrast to atom like gain media, in semiconductor opto-electronic devices a change in the optical gain is always accompanied by a change in the refractive index for the optical wave in the device. In most cases this leads to a modification and chirp of a propagating optical pulse[66]. The amplitude-phase coupling is caused by a coupling of the active states to the charge carrier reservoir storing the electrically injected carriers[26, 67].
Since this nonlinearity has been observed to cause broadening of the emission linewidth $\Delta\nu_0$ of a semiconductor laser, the linewidth enhancement factor (LEF) has been in-

troduced. With $\Delta v = \Delta v_0 \sqrt{1 + \alpha^2}$ the main quantity for amplitude phase coupling is represented by Henry's α-parameter [26]. It relates the changes in the real and the imaginary part of the refractive index with the changing number density N of carriers in the active region via

$$\alpha = -\frac{4\pi}{\lambda}\frac{\mathrm{d}n/\mathrm{d}N}{\mathrm{d}G/\mathrm{d}N}. \qquad (2.24)$$

Here, λ is the central wavelength, n is the real part of the refractive index and G is the effective modal gain. Typical values for bulk and QW semiconductor lasers range from 3 to 10 [68–70], though a careful selection of the spectral position of the laser line in single-mode lasers allows one to push the α-parameter to lower values [35]. Generally smaller α-parameters are predicted for devices based on QDs [71–73]. There, the interdependence of gain and refractive index is reduced by decoupling the active states and the carrier reservoir, with the isolated confined states of the QDs behaving like an atomic gain medium with ideally zero linewidth-enhancement. Experimentally, this has been confirmed for self-assembled QDs grown by the SK method at low injection current [72–74]. While for linear amplification and modulation schemes a low phase response is desirable, the opposite is true for some nonlinear applications like wavelength conversion or cross phase modulation [3].

Even though the denotation as *parameter* suggests a fixed quantity for each device, α finally has been found to be everything but that. In their work T. Fordell and A. M. Lindenberg used nine different experimental techniques for measuring the linewidth-enhancement factor of a single 760-nm VCSEL. revealing nine different quantities [75]. This actually does not make α less reliable, but instead requires an exact specification for the state of device operation corresponding measurement method. Amongst the most common measurement techniques are ASE analysis, small signal FM/AM response and direct linewidth measurements [76].

2.3. Optical Self-Feedback

Not only in academia, but also in commercial fiber optics networks SCLs can become subject to time-delayed optical self-feedback. Fiber-optical elements, interfaces of connectors, or even kinks within the fiber itself may enable partial reflection and potential re-injection of the transmitted traveling wave back into the laser. The thus created compound cavity between the laser output and the external mirror acts as a time-delayed optical perturbation of the lasing system and enables manifold laser dynamics.

2.3.1. **Laser Dynamics**

A common model to reproduce static and dynamical properties of an optically self-feedbacked SCL has been set up in 1980 by Lang and Kobayashi (LK) in terms of coupled rate equations [25]. A general form to describe the time evolution of a dynamical system with delayed coupling is:

$$\frac{\partial}{\partial t}x = f(x(t)) + \kappa g(x(t-\tau)), \tag{2.25}$$

with the feedback strength κ, the delay time τ and the arbitary functions f and g, which can be either linear or nonlinear according to the underlying system. In the LK model this formalism is specified for the complex field amplitude $E(t)$ and the carrier number above lasing threshold $N'(t) = N(t) - N_{th}$ of a self-feedbacked singlemode SCL. The most general form of the rate equations reads as follows: [22]

$$\frac{\partial}{\partial t}E(t) = \frac{1}{2}(1 + i\alpha)gN'(t)E(t) + \kappa E(t-\tau)e^{-i\omega t}, \tag{2.26}$$

$$\frac{\partial}{\partial t}N'(t) = J' - \gamma N'(t) - [\Gamma + gN(t)]E(t)^2, \tag{2.27}$$

The model links the electric field amplitude to the carrier access number in Equation 2.26 by means of the differential optical gain g and the α-parameter, which at the same time represent the major nonlinearities for the system. The second term considers the optical feedback for a given external cavity roundtrip time τ and the feedback rate κ as a scaling parameter.

The excess carrier numbers is driven by the pump current above threshold $J' = J - J_{th}$, the carrier decay rate γ, and the cavity decay rate Γ scaling the photon number $E(t)^2 = P(t)$. In case of absent feedback ($\kappa = 0$) the laser relaxation oscillation (RO) frequency $\nu_{RO} := \Omega$, denoting oscillations between carrier reservoir and photon field, is solely determined by the ratio of electron lifetime and photon lifetime. Typically the ROs of free running lasers are damped and their frequency is in the order of several GHz. However, since feedback strongly reduces this damping, oscillations may built up and drive the laser into a dynamic state of operation. In particular for SK QDs the ROs have been found to be especially strongly damped which is due to a de-synchronization of electron and hole dynamics in the dots, as reported in Ref. [6].

The cavity length for externally self-feedbacked lasers is distinguished into two different modes: the *short* and *long* cavity regime, always with respect to system internal frequencies [77, 78].
A cavity is considered as short, if $\nu_{EC} \approx \nu_{RO}$, which is typically in the order of

single-digit GHz. Translated into a physical path length, this means that short cavities measure only single-digit cm [79, 80]. In short cavities the feedback dynamics are very phase-sensitive, since resonances of the external cavity and the longitudinal lasing modes arise. In contrast, the cavity is considered long for if the external roundtrip time is at least one order of magnitude longer than the internal time scales, meaning $v_{EC} >> v_{RO}$. Typically ranging in the order of meters, external cavity modes (ECMs) average over several ROs in case of a long cavity, which is why the phase is of minor importance in that regime.

Typical phenomena in long cavities are low frequency fluctuations (LFF) [81] and coherence collapse (CC) [82], which result from the interaction of laser ROs and the mode spectrum.

2.3.2. Coherence Collapse

The denotation *Coherence Collapse* is traced back to the observation of optical self feedback reducing the coherence length of an SCL by up to three orders of magnitude [82, 83]. It has been found that this is due the feedback-induced destabilization of the cw-emitting system up to chaotic pulsations. As a consequence the denotation has been kept and CC now accounts for all kinds of chaos in optically injected or self-feedbacked systems [84–86].

Generally two parameters mainly determine the response of the system:

1. The feedback or injection rate κ

2. The nonlinear response in terms of the amplitude-phase coupling α

Regarding the feedback rate κ the laser dynamics can be categorized into five different regimes on a logarithmic power scale considering long cavities: [22]

I) -80 dB: Very low feedback already leads to a reduction or enhancement of the optical linewidth Δv, depending on the feedback phase.

II) -80...-45 dB: Depending on the cavity length L_{EC} the linewidth gets enhanced and the competition of internal and external cavity modes leads to mode hopping.

III) -45...-39 dB: In this narrow regime the mode hopping noise is suppressed and the laser returns to single mode emission.

IV) -40...-10 dB: Larger feedback leads to undamping of the laser ROs and creates sidebands within the electric spectrum, which are accompanied by a dramatic
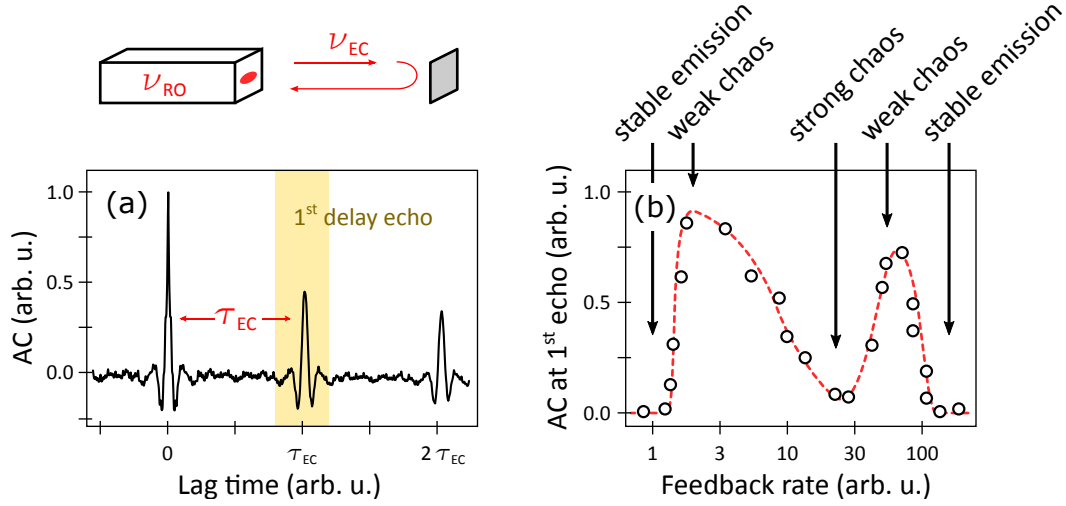
Figure 2.11.: (a) Intensity autocorrelation (AC) of feedback-induced laser intensity dynamics with the first delay echo highlighted. (b) Typical progress of the maximum AC height at the first delay echo for different feedback rates. High values indicate regimes of weak chaos, while values close to the noise floor either indicate regimes of stable emission or strong chaos. After [87].

broadening of the optical laser linewidth. This is the regime where CC occurs and the system emits chaotic pulsations independently to the feedback phase.

V) -10 dB: A further increase of the feedback ratio forces the system back to the stable mode emission at a narrow linewidth, regardless to the feedback phase. At this strong feedback regime the external and internal cavity act as one combined cavity.

In consequence when aiming at stable and linear operation mode, the optical self-feedback power of a single mode SCL should be suppressed by at least 40 dB to ensure no pulsation of the system. However the exact amount of feedback ratio for each regime of course depends on the SCL itself and mostly the α parameter [77, 84].

The intensity autocorrelation (AC) function is a convenient tool for analyzing the characteristic time scale of delayed feedbacked systems and to distinguish between different states of laser dynamics [87, 88]. Since modern technology enables the detection of dynamics on a double-digit GHz bandwidth, directly recorded time traces $I(t) = E^*E$ contain signatures of ν_{RO}, as well as multiples of external cavity

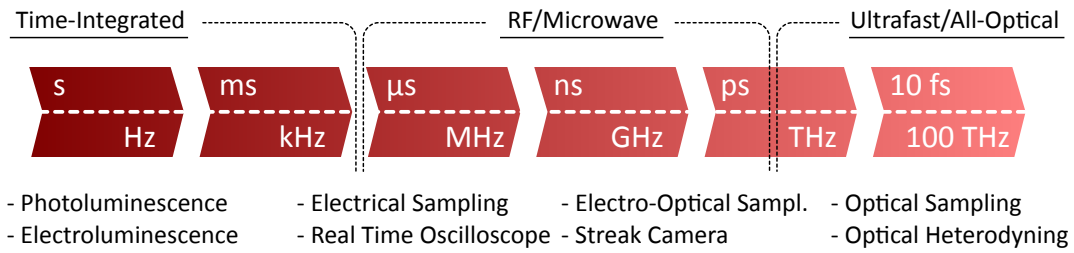roundtrips ν_{EC}. The AC at a certain lag time τ is calculated via:

$$AC(\tau) = \frac{1}{2T} \int_{-T}^{T} x(t)x(t+\tau)dt, \qquad (2.28)$$

where T is the total length of the recorded time trace. A typical AC trace is shown in Figure 2.11 (a), which was calculated for a recorded time series of a QW based FP SCL under optical feedback. The trace shows the zero-delay peak and two additional peaks of high correlation, which are attributed to ECMs and will be referred to as *delay echoes*. In their work, X. Porte et al. [87, 89] showed that the highlighted first echo peak can be used as marker to distinguish between weak and strong chaotic oscillations of the time traces.

A typical curve progression of the first delay echo at varying feedback rate is sketched in Figure 2.11 (b), indicating regions of weak and strong chaos, as well as stable cw emission. Weak chaos in this case is characterized by a high amount of correlation, while strong chaos an cw emission are indicated by a vanishing echo peak. Thus the observation of strong chaotic light fluctuations and CC requires a local minimum in the AC while tuning the feedback strength.

3. Experimental Techniques

This work aims to capture a wide range of optical properties of InAs/GaAs:Sb SML QDs before and after application into optoelectronic devices. In consequence multiple measurement methods are needed to access different characteristics of that material. While previous studies were mainly focused on structural research combined with basic luminescence analysis [20, 41], this work contains the spectroscopist's point of view on the system.

Time-Integrated		RF/Microwave			Ultrafast/All-Optical
s	ms	µs	ns	ps	10 fs
Hz	kHz	MHz	GHz	THz	100 THz

- Photoluminescence   - Electrical Sampling   - Electro-Optical Sampl.   - Optical Sampling
- Electroluminescence   - Real Time Oscilloscope - Streak Camera   - Optical Heterodyning

In this chapter the pool of utilized methods will be introduced. Different experiments focus on different time scales and thus gives access to different electronic processes. With time integrated detection a first estimation for the electronic states can be found. In this work the luminescence of a flat wafer sample is denoted as photoluminescence (PL), while for a electrically contacted waveguide sample it is indicated as electroluminescence (EL), referring to the way of carrier injection.

Electronic and electro-optical sampling methods are able to access carrier lifetimes up to a below ns-time scale, equivalent to a GHz bandwidth. The bandwidth of modern electronics is typically limited to a double-digit GHz range, which is why for faster processes all-optical sampling is required. Those ultrafast methods typically use optical fs pulses for coherent sampling, with the temporal dispersion resulting from a physical detuning path length and the time resolution limited by the pulse duration.
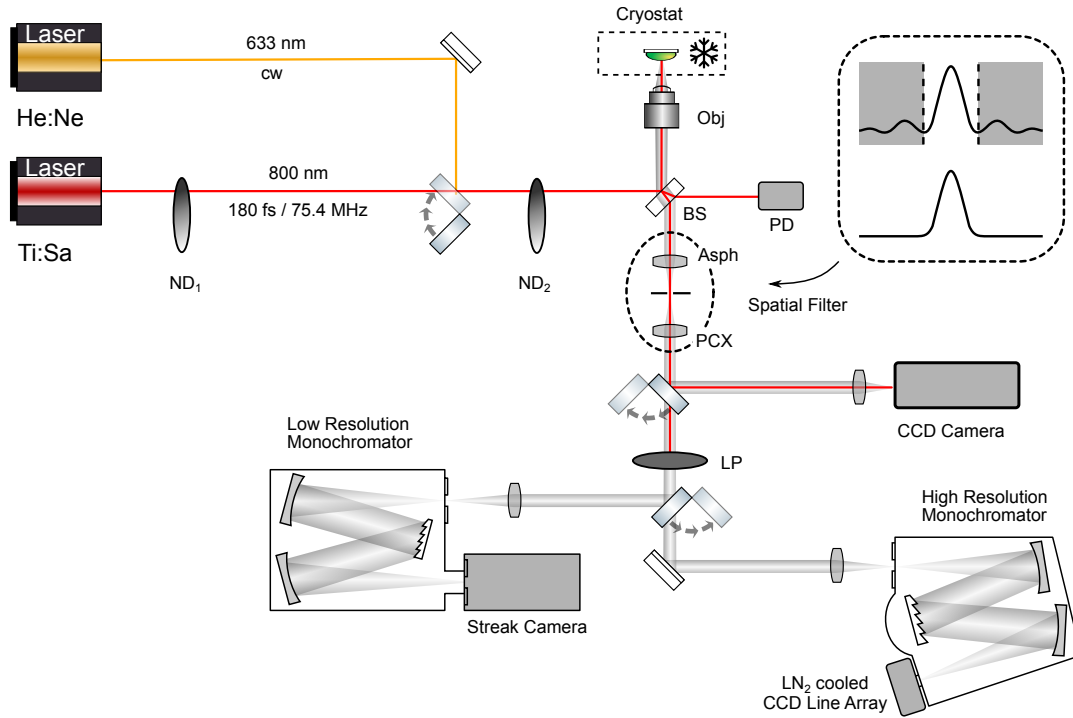
Figure 3.1.: Schematic setup for time-resolved and -integrated photoluminescence measurements. ND: neutral density filter, BS: beam splitter, PD: photo detector, LP: low pass filter, Obj: objective lens system, Asph: ashperic lens, PCX: plano convex lens, LN_2: liquid nitrogen.

3.1. Excitation Spectroscopy

The most basic way to gather information about any optically active semiconductor material's electronic states is to collect spontaneously emitted light after optical over-band excitation. Even though PL experiments are straight forward measurements, this method also represents a powerful spectroscopic tool for fundamental research. It allows the control of multiple isolated parameters, such as e.g. lattice temperature, excitation energy or external fields, which is why a large amount of fundamental material research happens by means of PL measurements. In this work PL spectra have been obtained in a twofold manner: temporally integrated and time- resolved, using different detection methods. The utilized confocal PL setup is sketched in Figure 3.1.

3. Experimental Techniques
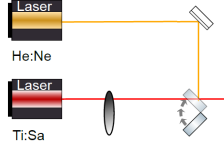
Optical excitation, thus photo-generation of charge carriers, was performed either by a cw Helium-Neon (He:Ne) laser emitting at a fixed wavelength of 633 nm (1.96 eV) or a mode-locked Coherent Mira HP Titan-Sapphire (Ti:Sa) laser with the wavelength tuned to 800 nm (1.55 eV). In both cases the respective photon energy was sufficient to linearly generate charge carriers in GaAs bulk material at 4 K lattice temperature, which forms the carrier reservoir of all investigated samples. While the Ti:Sa pulses are nearly resonant to the barrier band gap of 830 nm (1.54 eV) at 4 K, the He:Ne light creates carriers far above band edge leading to a cooling cascade. The Ti:Sa laser produces pulses of 180 fs length, which are separated by 13 ns and are equivalent to an instantaneous carrier injection at the band edge with 6 orders of magnitude larger pulse intensity as compared to cw light of similar average power. The power of both lasers is controlled by a continuous neutral density (ND) filter wheel in front of the sample with an additional ND filter in the Ti:Sa path due to its significantly larger output power.
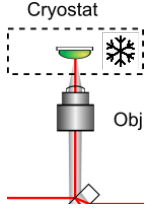
All investigated PL-samples were mounted inside a Helium-flow cryostat allowing a temperature tuning from 4 K up to room temperature. Detection of the luminescence light was performed in a threefold manner. While a standard silicon-based CCD camera is used for position control, time-integrated and time-resolved spectra were obtained by a liquid-nitrogen cooled CCD array and a fast streak camera system, each attached to a monochromator. The spatial direction for both, excitation and detection, in the setup was chosen to normal incidence to the wafer surface, which is why a dielectric filter is needed to suppress reflected laser light at the detection side.
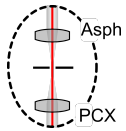
Spatial filtering is required to ensure proper imaging through the respective spectrometers. A spatial filter in its simplest geometry is built by an aspheric lens focusing the PL light onto a pinhole, thus cutting out a Gaussian beam shape, which is then collimated by a plano-convex lens. This process is visualized in the dashed box in Figure 3.1. In order to achieve a spot size close to the diffraction limit the pinhole diameter D has to be chosen after:

$$D = \frac{\lambda f_{aspheric}}{r},\tag{3.1}$$

with the aspheric focal length $f_{aspheric}$, the PL center wavelength λ and the spot size r, determined by the objective lens in front of the cryostat. In the experiment a focal length of 300 mm and an adjustable pinhole with minimum diameter of 100 μm have been chosen.

30
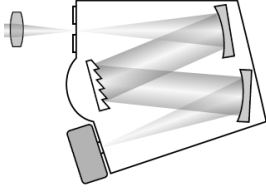
Spectral dispersion was achieved by an either high or low-resolution monochromator attached to the CCD array or streak camera system, respectively. As sketched in Figure 3.1 both grating monochromators are in the Czerny-Turner design with an either fine or coarse blazed grating. The maximum resolution of such a system is defined by:

$$\frac{\lambda}{\Delta\lambda} = m\,N_{lines}\,, \tag{3.2}$$

with the order m and the line number N_{lines}. For the time-integrated detection a Horiba Jobin Yvon iHR 550 fully automated imaging spectrometer was used, containing a 10 cm blazed grating with 300 lines/mm. According to Equation 3.2 the maximum resolution is then $3 \cdot 10^4$ at the first diffraction order, which is equivalent to a spectral resolution of 0.035 nm at $\lambda = 1060$ nm. For detection a liquid nitrogen-cooled Horiba Jobin Yvon *Symphony IGA* InGaAs CCD array was used with a quantum efficiency >80 % at the operated wavelength range.

For the time-resolved measurement a Hamamatsu C5680 streak camera was attached to an Acton SP2500 spectrometer with an 8 cm blazed grating, containing 40 lines/mm. With this spectrometer a maximum resolution of $3.2 \cdot 10^3$, equivalent to 0.3 nm at $\lambda = 1060$ nm can be achieved. The temporal resolution of this combined system is about 33 ps. Even though the streak camera is able to reach a temporal resolution down to 3.5 ps, it was driven at lower resolution in order to capture longer luminescence lifetimes.

3.2. Laser Characterization

In contrast to the previous PL setup, a different geometry is required to investigate waveguide samples. For confocal luminescence studies the material of interest typically needs to be attached to extended wafer pieces, while it is buried inside a directed waveguide in case of edge-emitting SCLs. Charge carriers are no longer optically excited, but can be injected via electrical contacts, enabling inversion of the electronic system. The thus generated light is amplified along the waveguide via stimulated emission, enabling to produce much larger output powers than for PL samples. However cooling of waveguides becomes more difficult, since electrical contacts may flake or spall at cryogenic temperatures, which is why devices for this work were
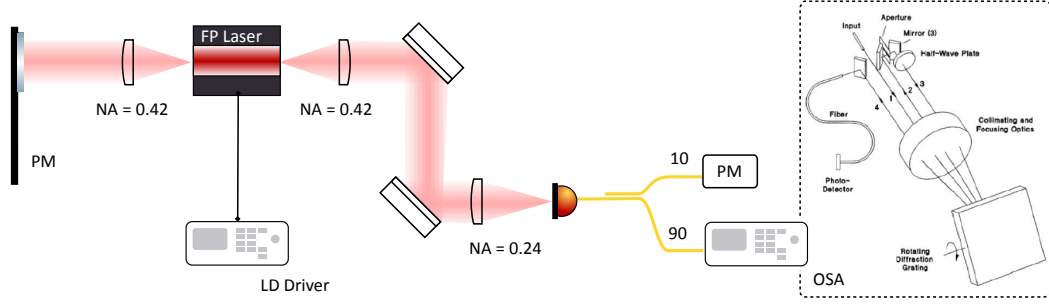
Figure 3.2.: Schematic setup for static characterization of waveguide devices, e.g., semiconductor lasers. OSA: optical spectrum analyzer, PM: power meter, LD: laser diode, FP: Fabry-Pérot.

operated at room temperature with temperature stabilization. The setup of SCL characterization is shown in Figure 3.2.

All devices in this work were processed symmetrically in terms of their output facets, which is why both sides can be simultaneously used for characterization. The divergent output light has been collected by NA-matched collimation lenses with one side used for free-space power measurement and the other side for spectral characterization via an optical spectrum analyzer (OSA). A laser diode driver was used to provide constant current injection, as such as temperature stabilization of a PID-controlled Peltier heat sink, providing $\Delta T < 0.2$ K.

3.2.1. Lasing Threshold

Light-current (LI) characteristic curves are obtained by simply tracking of the laser output power over the injected current. It is typically used to obtain quantities as, e.g., lasing threshold and quantum efficiency. Particularly for device modeling, as well as comparability among different devices the injection current often is normalized by its threshold value. Generally the designation *threshold* denotes overcoming of losses and domination of stimulated emission, which in case of SCLs means transition from LED to lasing mode, changing from thermal to coherent light emission.

Both modes follow an approximately linear output slope with a nonlinear transition area denoted as *kink*. A typical LI curve is shown in Figure 3.3 (a) for an InAs/GaAs SML QD based FP SCL. This kink, however, leads translates into an uncertainty of the exact threshold, which is why a deterministic fit method is required. The most common methods use linear fitting or derivatives of L(I). Figure 3.3 (b) - (d) shows the application of a collective of four different algorithms to the data: [90]
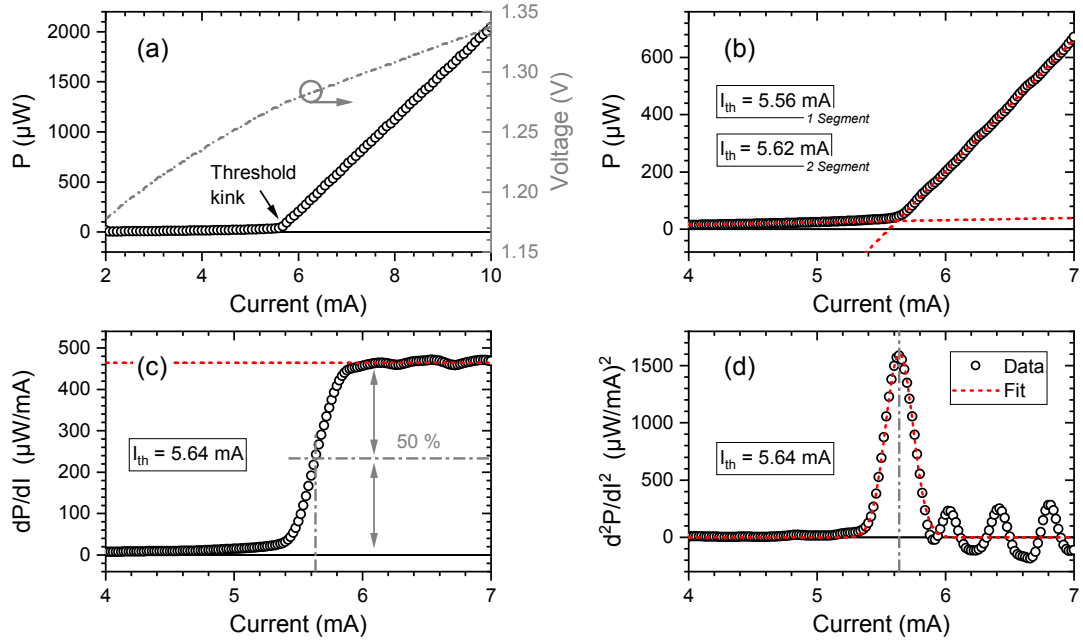
Figure 3.3.: (a) Light-current-voltage (LIV) characteristics of an InAs/GaAs SML QD based laser diode and different methods for threshold current determination: (b) linear fitting, (c) first derivative, and (d) second derivative.

- Linear line fit: extrapolation of the output power above threshold to zero
- Two segment line fit: intersection of linear regions before and after threshold
- First derivative: define threshold at 50 % slope of the output power
- Second derivative: define threshold at the strongest curvature

All methods deliver slightly different results for the very same data with I_{th} ranging from (5.557 ± 0.007) mA for the linear line fit, to (5.639 ± 0.002) mA for the second derivative method. Even though none of these algorithms claims to deliver the real threshold value, the latter leads to most reproductive and reliable results. Especially the linear methods underestimate I_{th} and are only used for quick check, since they can be applied to a small number of measurement points. The deviation of the linear method as compared to the second derivative accounts for 1.5 % at this example.

3.2.2. Gain Measurement after Hakki and Paoli

The OSA in Figure 3.2 enables to rapidly capture optical spectra at a sub-nm resolution. The operating principle of most such spectrometers is similar to the grating monochromators from previous section, but allows adjustment-free operation and good data reproduction due to a fiber-coupled input source. A schematic of the uti-

lized OSA *Hewlett Packard 71450B* is sketched in the dashed box of Figure 3.2. A double-monochromator alignment is used for two-fold filtering of the incoupled light with a single diffraction grating. A half-wave plate in the second filter path further ensures polarization-independent detection, which is required due to fiber nonlinearities. This OSA enables to capture spectra with a minimal resolution of 0.08 nm at a sensitivity down to -80 dBm. The resolution is sufficient to capture longitudinal modes of FP lases, but would be too low to capture modes of, e.g., distributed feedback (DFB) or external cavity lasers (ECLs). Highest resolution OSAs to date use nonlinear stimulated Brillouin scattering (*BOSA*) to achieve sharp filtering of below sub-pm linewidths.

The optical gain is a key quantity determining many operating characteristics of semiconductor lasers. The modal gain G basically describes the amount of light amplification when passing through an optically active medium and directly depends on the electronic structure of the medium, as well as external cavity parameters.

The net modal gain G_{net} defines the modal gain including cavity losses α_{int} and can directly be measured. In contrast, the material gain g_{mat} includes the total amount of gain within the active medium and has to be reconstructed with the mode-confinement factor Γ:

$$G_{net} = G - \alpha_{int} = \Gamma g_{mat} - \alpha_{int}. \tag{3.3}$$

Amongst multiple ways, the most common technique to obtain the modal gain G_{net} is the method after Hakki-Paoli (HP) [91]. It estimates G_{net} from the modulation-depth of longitudinal modes in Fabry-Pérot resonators below threshold. Considering a traveling lightwave through a waveguide of length L, the single pass gain reads:

$$E_{out} = E_{in} \cdot e^{(G(\lambda)-\alpha)L} \tag{3.4}$$

After a number of reflections on the facet with reflectivity R the field amplitude in case of positive interference develops into:

$$E_{out}^{+} = E_{in} \sum_{n=0}^{\inf} R^n e^{(G(\lambda)-\alpha)L} \Rightarrow E_{out}^{+} = \frac{E_{in}}{1 - R^n e^{(G(\lambda)-\alpha)L}}, \tag{3.5}$$

with the sum approximated after $\sum_{n=0}^{\inf} = (1 - x)^{-1}$ for $x < 1$, which is only fulfilled for below threshold operation. Following similar thoughts for negative interference
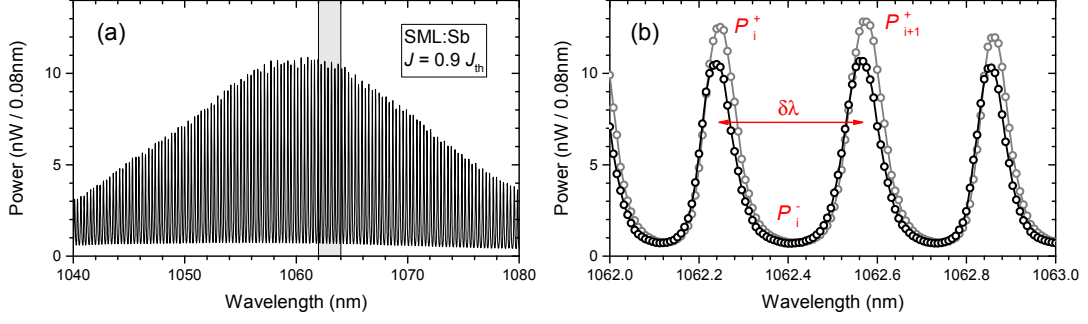
Figure 3.4.: (a) High-resolution output spectrum of a 0.5 mm long InAs/GaAs SML QD based laser diode below threshold. (b) Resolved longitudinal modes of the highlighted area.

E_{out}^- and considering the optical power $P = E^2$, the gain can be calculated via:

$$G(\lambda) - \alpha = \frac{1}{L} \left(\frac{\sqrt{P^+} - \sqrt{P^-}}{\sqrt{P^+} - \sqrt{P^-}} \right) + \frac{1}{L \, ln(R)}. \tag{3.6}$$

Figure 3.4 (a) shows a typical emission spectrum of an InAs/GaAs SML based laser diode with a 0.5 mm cavity. The magnification of the data in (b) shows the longitudinal lasing modes at P^+ and P^- marked as red data points. The measured power for this optical spectrum is given with respect to the resolution to indicate the spectral window of detection.

Further indicated in the figure is the mode spacing $\delta\lambda$, which for this laser is 0.3 nm. Considering the Nyquist theorem for proper sampling resolution, the OSA reaches a fourfold resolution with respect to the mode spacing, leading to properly reconstructed spectra. As the mode spacing inversely scales with the cavity length, it is not possible to measure longer devices with this particular OSA.

Apart from the widely used HP method, a large number of alternative gain measurement techniques have been developed, ranging from advanced evaluation of HP spectra [92, 93] up to, e.g., small signal modulation methods [94].

3.2.3. Amplitude-Phase Coupling after Henning and Collins

To proceed, power measurement of longitudinal lasing modes not only enables to obtain gain spectra, but also leads to the α-parameter, introduced in subsection 2.2.5. In addition to the mode gain after HP, the measurement after Henning and Collins (HC) [95] also considers the spectral mode shift with varying current, induced by a change of the refractive index n. For a specific mode λ_i, the α-parameter is obtained via:

$$\alpha_{stat} = \frac{2}{\delta\lambda} \cdot \frac{d\lambda_i}{dG_{net,i}}, \tag{3.7}$$

with the mode spacing $\delta\lambda$ determined by the cavity length L:

$$\delta\lambda_i = \frac{\lambda_i^2}{2nL}.$$ (3.8)

Since this method is based on time-integrated spectra, the parameter is retrieved in a steady-state condition of the laser, which is why it is denoted as α_{stat} in this case. The α-parameter generally is a very non-trivial parameter, which amongst others also varies with the operating condition of the device [75] and will be discussed in more detail later in this work. Typical values for α obtained from the HC method range from 1-3 for modern MQW based lasers and can reach up to 10 for more non-linear active media and cavities.

3.3. Electrical Sampling

When it comes to measuring dynamic processes, the most straight-forward way is to time-resolving detectors with fast response. Typically a bandwidth ranging in the double-digit GHz range, equivalent to time scales of double digit ps values is required.

3.3.1. RF Spectroscopy

Radio-frequency (RF) engineering aims to capture extremely fast signal rates reaching microwave bandwidths, thus representing the transition between electronics and optics. This is far from trivial, as the damping in electric waveguides rises dramatically for above-GHz frequencies. In this work, the measurement of optical self feedback-induced laser instabilities were performed solely with RF equipment at a maximum bandwidth of 16 GHz, given by the AC coupled Newport PD 1554-A-50 photoreceiver.

An Electrical Spectrum analyzer (ESA) represents the electronic counterpart to the previously introduced OSA. Instead of a diffraction grating, the ESA uses various electronic sweep techniques to scan resonances within a determined electronic spectral range. Besides the possibility of fast Fourier-transforming an input signal, most ESAs rather work with a swept local oscillator source, allowing for low noise and high bandwidth signal detection. Also used for ,e.g., analog radio reception, *heterodyne detection* is based on a frequency shift of the signal, induced by nonlinear mixing with an internal tunable local oscillator (LO) source. The multiplication of
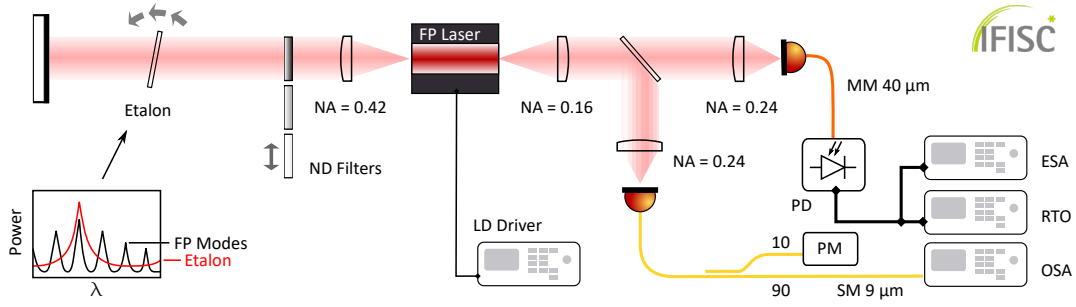
Figure 3.5.: Schematic setup for application of time-delayed optical self-feedback and measurement of laser dynamics. SM: single-mode fiber, MM: multi-mode fiber, PD: photodetector, E(O)SA: electrical (optical) spectrum analyzer, RTO: real-time oscilloscope. The measurements were performed at the IFISC / Spain in the laboratory of Prof. Ingo Fischer.

signal and LO creates new correlated frequencies, which after narrow filtering and amplification can be demodulated and processed at low noise floor. In this work an *Anritsu MS2767C* electrical spectrum analyzer (ESA) with a maximum bandwidth of 9 kHz - 30 GHz has been used.

In order to capture non-periodic events, as e.g. chaotic laser pulsations, the measurement has to be performed in *one shot*. This means capturing an adjacent trace of the temporal data, which is only possible using an analogue bandwidth oscilloscope, also referred to as real-time oscilloscope (RTO). In the experiment sketched in Figure 3.6 a LeCroy Wavemaster 816Zi RTO has been utilized with an analogue bandwidth of 16 GHz at 40 GSamples/s, equivalent to a data point distance of 25 ps. During the measurements typically time windows of 20 ms were taken at highest sampling rate, leading to a total amount of $2 \cdot 10^6$ data points per measurement.

3.3.2. Optical Self-Feedback

A schematic setup for application of delayed optical self-feedbacked and measurement of laser dynamics is shown in Figure 3.5. All measurements were performed in the photonics lab in the group of Prof. I. Fischer at the IFISC / UIB Palma de Mallorca during a 2 month research stay. The lab was optimized for measurements within the spectral telecommunication windows of 1310 and 1550 nm, which is why a free-space configuration has been chosen. Even though most groups perform feedback experiments in fiber-based setups, also the possibility of larger achievable feedback ratios, as well as the absence of fiber-dispersion support the decision for free-space measurements.

Just like the characterization measurements, both laser facets were utilized in this experiment as well with one side used for delayed self-feedback and the other side for detection of instabilities. The external feedback cavity was implemented by a dielectric high-reflection coated mirror on a Gimbal mount, ensuring constant path length during adjustment. Remaining in the long cavity regime the physical length of the external cavity was set to 53 cm, equivalent to 3.5 ns optical roundtrip time.

A tunable attenuator in the cavity side was used to set the feedback ratio $\kappa = P_{fb}/P_{out}$. As κ cannot be measured explicitly, all measurements were performed with respect to the degree of attenuation μ. Both are linked via:

$$\mu \, [dB] = -20 \log_{10} \left(\frac{\kappa}{\kappa_{max}} \right) , \tag{3.9}$$

with the maximum achievable feedback ratio κ_{max}, which can be calculated from the feedback-induced threshold current reduction. Due to the logarithmic dependency of μ and κ the attenuation is typically scaled in [dB] rather than absolute units.

The measurement of μ was simply performed by recording the optical power before and after the ND filters showing a maximum attenuation of 39 dB.

Finally, an etalon within the cavity was used for mode selection in case of single/few modal feedback investigations. However, investigations of multimodal feedback have been performed without mode selection.

3.4. All-Optical Sampling

While the RF setup from previous section aims to measure non-reproductive dynamics on a sub-ns time scale, the temporal resolution in case of all-optical sampling enables to capture sub-ps dynamics and thus access processes as, e.g., electronic intraband transitions or Auger scattering. The key idea of ultrafast spectroscopy is to overcome electronics and instead to use short optical pulses for gating or sampling of any optical signal.

Shortest temporal windows for light at near infrared (NIR) spectral range account for single-digit fs duration, which is the temporal limit of those methods. Further increasing the bandwidth to shorter wavelengths down to UV or even X-ray range enables to observe events even in the attosecond range.

3.4.1. Optical Heterodyne Detection

Extending the thoughts of nonlinear frequency mixing from subsection 3.3.1, the heterodyne principle is not solely limited to the microwave spectral range but rather applies to all kinds of electromagnetic waves. Entering the optical spectral range, application of heterodyne mixing would not only allow for noise-reduced detection, but also enables e.g. temporal phase resolution when detecting pulsed light.

For this work optical heterodyning was achieved using an acousto-optical modulator (AOM) to modulate pulses of a *Toptica FemtoFiber pro SCIR* supercontinuum fiber laser system. This passively modelocked lasersystem uses an Er-doped fiber oscillator attached to a photonic crystal fiber amplifier, producing optical pulses of 20...250 fs duration at a repetition rate of 75.4 MHz. Due to the largely nonlinear fiber those pulses are not bandwidth limited and require further compression and spectral shaping. As sketched in the dashed box of Figure 3.6, the AOM uses an piezo-driven acoustic field to shift the individual laser modes by a frequency of $f_{AOM} = 77.3\ MHz$, locating them close to the neighboring mode with a spacing of $f_{AOM} - f_{Rep} = 1.9\ \text{MHz}$. Feeding both signals to an electronic multiplier creates harmonic frequencies, which after filtering condenses to the heterodyne frequency of 1.9 MHz which then can be used as reference input for a lock-in amplifier.

Regarding the optical side, detection of the AOM-deflected fs-pulse is achieved by interference with a non-deflected fraction of itself, referred to as local oscillator (LO). This leads to a beating at the previously mentioned heterodyne frequency, equivalent to a unique frequency marker. In this work the thus marked pulse will be referred to as *probe*, used to e.g. probe the light matter interaction of semiconductor material. A balanced detection of that signal is used for offset-free detection and consequently high sensitivity due to a measurement relative to zero instead of detecting a small modulation on top of a finite background.

Interference with the static LO, combined with complex lock-in amplification furher enables phase sensitive measurements due to the pronounced phase relation of probe and LO pulse, as both originate from the same master oscillator. The obtained complex signal enables a full bandwidth of experiments, namely pulse characterization [96], quantum state reconstruction [97], coherent 2D spectroscopy [98], and time-delayed pump-probe spectroscopy [4, 9, 99, 100]
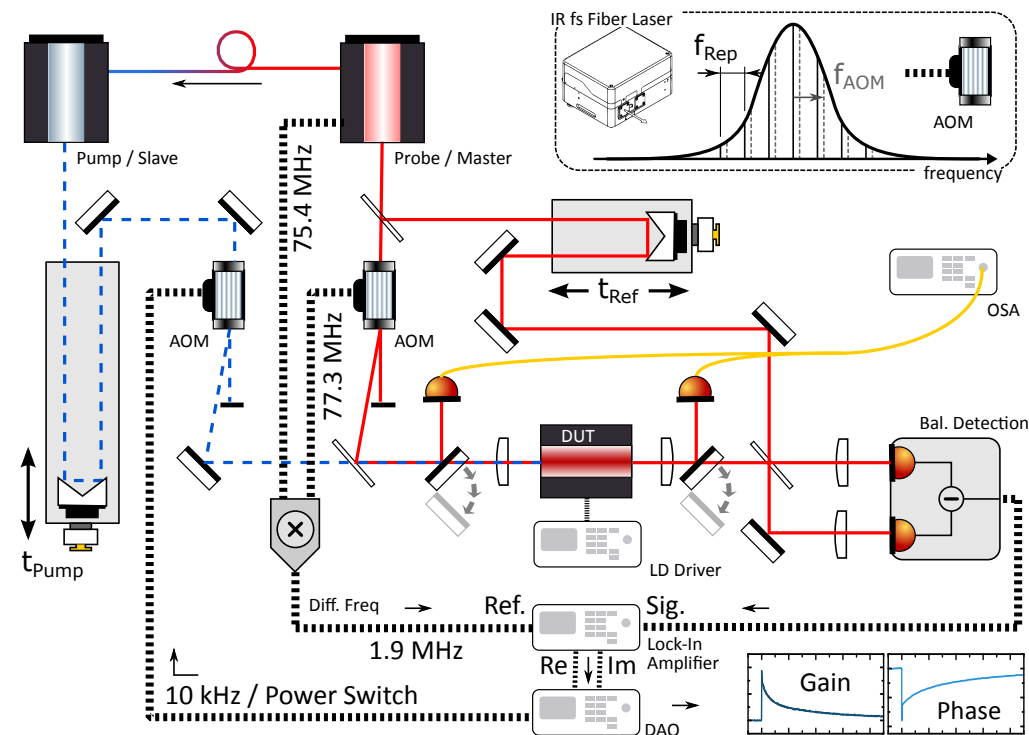
Figure 3.6.: Schematic of the heterodyne detected pump-probe experiment. AOM: acoustio-optical modulator, DAQ: data acquisition, DUT: device under test, OSA: optical spectrum analyzer.

3.4.2. Time-Delayed Pump-Probe

Based on optical heterodyne detection in 1992 K. L. Hall et al. first published a technique for time-domain studies at a collinear and copolarized pump-probe geometry [101], thus enabling to measure dynamics at waveguide structures. Two decades later this particular technique has been greatly optimized, leading to the utilized setup of this work, which was by a great extend developed by M. Kolarczik [98] and is sketched in Figure 3.6. The goal of this technique is to temporally resolve the gain and refractive index dynamics of waveguide devices, mainly SOAs, on a sub-ps time scale.

While the LO reference was guided directly to the detector without passing any transmitting optics, a suitable spectral part of the emitted fiberlaser supercontinuum is selected by an amplitude mask in the Fourier plane of a 4f pulse shaper. Typically, the pulses were shaped to a temporal and spectral FWHM of 250 fs and 10 nm (13 meV), respectively. Afterwards pulses were frequency marked and then coupled into the device under test (DUT). Due to the waveguide geometry the signal can accumulate along propagation. The outcoupled light is then interfered with the LO and after bal-

anced detection directly fed to the fast lock-in amplifier. A delay stage in the LO path was used to tune the temporal overlap, denoted as t_{Ref} of the LO and probe pulses. Pump pulses, required to excite the electronic system of the DUT, where generated with a second fiber laser system. This slave laser consists of an independent amplifier and supercontinuum stage, fed by the master oscillator of the probe laser in order to provide optimal synchronization. An additional 4f pulse shaper was used to tune the pulses similar to the probe and another AOM was used to distinguish the pulses from LO and probe and for fast on/off switching. Measurements at identical pump and probe wavelengths will be referred to as single color pump probe (1cPP), while the case of different wavelengths will be referred to as dual color pump probe (2cPP).

From the transmitted probe power reaching the balanced detector, a complex lock-in voltage $V = |V| \exp(i\,\Phi(t))$ can be derived. Considering the ratio of the signal V in presence and V_0 absence of the pump laser leads to the complex pump-probe signal at a delay time $t_{Pump} := t$. The differential gain ΔG and the phase shift $\Delta\Phi$ are obtained after separation of V into amplitude and phase:

$$\Delta G(t)\,[dB] = 20 \cdot \log \frac{|V(t)|}{|V_0|}, \tag{3.10}$$

$$\Delta\Phi(t)\,[rad] = \Phi(t) - \Phi_0. \tag{3.11}$$

As the gain G accumulates along the device length, ΔG scales logarithmic according to Equation 2.10. The sign of G is related to the probe transmission, which in case of a leading amplified pump-pulse is negative, due to carrier depletion. The cases of $\Delta G(t) > 0$ and $\Delta G(t) < 0$ will thus be named absorption and amplification regime, while transparency occurs at the transition $\Delta G(t) = 0$. The sign of Φ gives the pump-induced refractive index change with a negative sign originating from a longer transmission time due to, e.g., absorption.

3.4.3. Heterodyne-Detected Coherent 2D Spectroscopy

While the pump-probe measurement is limited to one frequency dimension, it can be extended to a two dimensional (2D) method. Unfolding the spectral information onto a second dimension, ultrafast 2D coherent spectroscopy can be used to correlate absorbing, coupling and emitting states of an electronic system [102].
Scanning of the reference delay t_{Ref} during phase-sensitive tracking of the temporal overlap further enables a method to obtain pulse characterization measurement. First

demonstrated by Kolarczik et al. [96] this method has been used to reveal Rabi oscillations in an SK QD SOA. The authors achieved phase tracking by adding a HeNe laser based Michelson interferometer to the delay stage and referring to the corresponding interference signal.

Adding the pump-laser in the next step allows to probe a two-dimensional delay map, containing not only information about electronic states, but also their coherent coupling and respective linewidth [98]. Thus the detection is not limited to the probe laser, but rather the four wave mixing (FWM) signal created by the pump-probe interference. Post-measurement Fourier transformation finally leads to a 2D map of the probed electronic system revealing the entity of coherent states and couplings.

It has to be noted that in contrast to classical 2D spectroscopy after Cundiff et al. [103] two significant differences exist in case of heterodyne white light spectrsocopy: [98]

(1) The measurement is performed with only two interacting pulses, rather than three, in case of the classical method. This means that the separated coherence and population creation are induced simultaneously.

(2) Instead of the typical spectral window of a Ti:Saphire laser, the white light pulses of the fiberlaser system provide a way broader spectral range for probing.

4. Sample Pool

In this chapter an overview of all investigated samples containing variations of differently grown InAs/GaAs and InAs/GaAs:Sb submonolayer quantum dot structures, as well as quantum well and self-assembled quantum dot layers as reference samples is given. Since this work aims to firstly understand the electronic and optical properties of submonolayer quantum dots and secondly to point out the applicability into optoelectronic devices, different types of sample structures and geometries were required. In this chapter two different series of samples will be introduced and individual features will be highlighted:

- **Series SML$_{960}$** is formed by a set of InAs/GaAs SML QD based semiconductor optical amplifiers, emitting in the spectral range of 960 nm.

- **Series SML$_{1060}$, SML:Sb$_{1060}$** contains a set of of SML and Sb-alloyed SML QD based samples, as well as self-assembled QD and QW based samples as references. All samples emit in the 1060 nm range and consist of both, unprocessed wafer pieces, as well as laser and amplifier structures.

4.1. InAs/GaAs SML SOAs Operating at 960 nm

The first sample series is denoted as SML$_{960}$, thus neglecting the unit *nm* for the sake of convenience consists. It consists of a number of SOAs processed from a single wafer. The MOVPE growth and the processing were realized by J.-H. Schulze and Arsenijević, respectively, in the group of D. Bimberg at TU Berlin. A cycled deposition of 6 x 0.4/1.6 ML InAs/GaAs was implemented, leading to room-temperature emission in the spectral range of 960 nm. An entity of five SML layers was embedded into the waveguide in order to achieve larger gain values. To enable electric injection a PIN diode structure was grown on a Si-doped GaAs substrate with the layer structure sketched in Figure 4.1. The active region was centered inside an intrinsic GaAs matrix region and sandwiched between an AlGaAs cladding forming the optical waveguide.

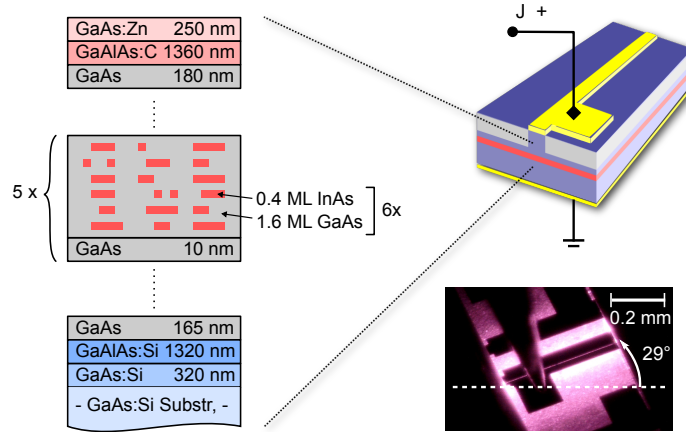The processing into SOA devices structures comprises facet cleaving, etching of a

Figure 4.1.: Epitaxial and processing structure of the semiconductor optical amplifiers from the SML$_{960}$ sample series and top-view microscope image of a forward-biased device.

ridge waveguide, and the application of contacts for current injection. The topside-p Shottky-contact was formed by highly Zn-doped GaAs and a 370 nm metal contact sequence of Ti-Pt-Au. Lateral waveguiding was achieved after shallow-etching of a 2 μm ridge down to about 80 nm above the active medium and isolating with 150 nm SiN. The ridge was tilted 8° against the facet normal, formed by a crystal axis, which is why the device was mounted at a 29° tilt towards the light propagation direction. The bottom-n Schottky-contact was formed by a 280 nm sequence of Ni-Au/Ge-Au sputtered on the GaAs:Si substrate.

It has to be noted that the SML$_{960}$ samples were the first SOAs based on SML QDs ever created, making those devices also a bit of pioneer structures. The microscope image in Figure 4.1 shows the SOA strip and the contact probe used for current supply. [4].

4.2. Combined Samples for the 1060 nm Range

The second sample series for this work followed the development of alloying InAs/GaAs SML QDs with Sb, which allows to red-shift the luminescence [41], as introduced in subsection 2.1.1. In order to analyze the applicability of in particular SML:Sb QDs for optoelectronic devices and to throw light on many different facets of performance, a number of systematic samples were grown. Those comprise SML structures with and without Sb, as well as SK QD and SQW references, designed for room temperature emission at the technologically important wavelength range of 1060 nm.

Wafers each containing one of the four different types of nanostructures were grown:

- **SQW**$_{1060}$ - A single quantum well layer formed by 8.3 nm of In$_{0.23}$Ga$_{0.77}$As

- **SML**$_{1060}$ - One layer of 15 x 0.73/1.13 ML InAs/GaAs depositions

- **SML:Sb**$_{1060}$ - One layer of 8 x 0.83/1.59 ML InAs/GaAs depositions, alloyed with 7 μmol Sb per cycle

- **SK QD**$_{1060}$ - One layer of self-assembled QDs, grown in the Stranski-Krastanow mode with a composition of In$_{0.6}$Ga$_{0.4}$As

Apart from the active region all samples were grown with identical layer structures of a pin diode, as sketched in Figure 4.2 (a). The waveguide for these structures was formed by GaAs/Al$_{13}$Ga$_{87}$As layers rather than pure GaAs, which leads to lower strain and slightly lower mode confinement. The cladding was formed by Al$_{30}$Ga$_{70}$As with the larger Al-amount enabling waveguiding. Since the layer structures of all wafers contain a single active QW or QD layer with a 10 nm GaAs buffer, comparable carrier pathways after electrical injection were ensured.
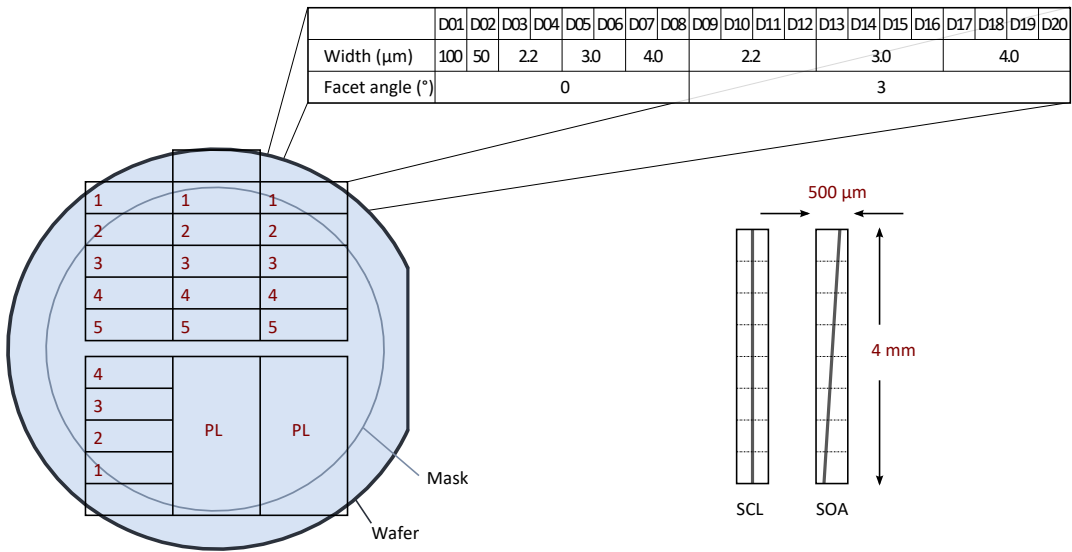
Regarding the epitaxial structure, the samples thus change from regularly distributed InAs and GaAs in case of the SQW up to In-rich agglomeration of InAs decreasing in size from the SML to the SML:Sb and SK QD material. Similar to the *960*-samples all wafers of this series were grown by J.-H. Schulze (TU Berlin) via MOVPE. Subsequent wafer processing into a systematic series of SCL, SOA, and PL samples was performed by O. Brox (FBH Berlin).

The major portion of the wafers were subdivided into bars of edge-emitting ridge waveguides, each containing a set of 20 adjacent devices, as it is listed in the table of Figure 4.2 (b). The ridges of those samples were shallow etched until 180 nm above the active region, forming the individual waveguides. Depending on width and tilt angle of those ridges the resulting device either performs as broad area laser (D01, D02), single mode laser (D03-D08), or optical amplifier (D09-D20). Measurements have shown that only waveguides with 2.2 and 3.0 μm broad ridges perform transverse single-modal. While for laser emission the bars were left as-cleaved, an AR-coating was applied to the facets to ensure feedback suppression in case of SOA structures. Amongst the large amount of samples comprised in the *1060*-series, the main goal of this series is the characterization of both, the SML and SML:Sb samples and to point out strengths and weaknesses of this material as compared to the well established QW and SK QD structures, which will be considered as reference samples in this work.

Width (nm)	Material	dopand	Layer	Refractive index (1060 nm)
270	GaAs	p	Contact	3.4715
2000	$Al_{30}Ga_{70}As$	p	Cladding	3.3042
135	$Al_{13}Ga_{87}As$	i	Waveguide	3.4025
10	GaAs	i	Matrix	3.4821
8	-- Active medium --			3.6487
10	GaAs	i	Matrix	3.4821
135	$Al_{13}Ga_{87}As$	i	Waveguide	3.4025
2000	$Al_{30}Ga_{70}As$	n	Cladding	3.3042
320	GaAs	n	Contact	3.4715
450000	GaAs	n	Substrate	3.4715
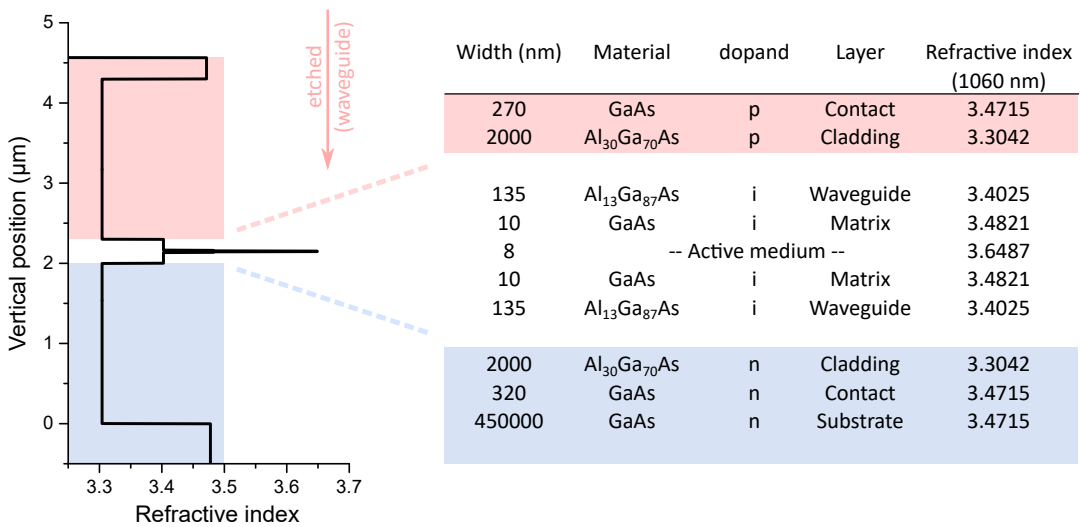
(a) 1060-Series: Layer structure

	D01	D02	D03	D04	D05	D06	D07	D08	D09	D10	D11	D12	D13	D14	D15	D16	D17	D18	D19	D20
Width (μm)	100	50	2.2		3.0		4.0		2.2				3.0				4.0			
Facet angle (°)		0							3											

(b) 1060-Series: Processing mask

Figure 4.2.: (a) Epitaxial layer structure and vertical refractive index profile of the 1060-sample series. (b) Processing mask to separate the wafer into regions of laser (SCL), amplifier (SOA), and analysis (PL) structures.

Luminescence

For luminescence experiments at cryogenic temperatures the p-doped layers of the wafers were etched down to the intrinsic region, exposing the waveguide and enabling topside optical excitation. Those PL sections were cleaved into small pieces of few mm edge length, which could then be mounted inside of a helium flow cryostat.

Figure 4.3 shows the luminescence at 4 K of all PL samples from the *1060*-series after optical excitation at 100 W/cm^{-2} on a 300 μm^2 spot. All spectra were fitted by simple Gaussian (SQW, SML, SK QD) or double-Gaussian (SML:Sb) peak functions in order to obtain individual FWHM values for qualitative comparison.

The narrowest emission was observed for the SQW sample, showing ΔE_{SQW} = 6 meV, which is due the the typical high carrier mobility in 2 D structures, enabling carriers to efficiently relax down to lowest energy states before recombining. In comparison a slightly broadened emission of ΔE_{SML} = 8 meV was observed for the SML sample, which is assumed to originate from the inhomogeneously broadened distribution of recombination centers, formed by the In-rich agglomerations. For the SML:Sb sample, in contrast, a dramatic broadening has been found, including a bimodal state distribution. The combined width of $\Delta E_{SML:Sb}$ = 54 meV can be well fitted by two distinct Gaussian states, separated by 39 meV, which will be further investigated in the following. The broadest emission of $\Delta E_{SK\ QD}$ = 68 meV has been observed for the SK QD sample, which accounts for a tenfold increase as compared to the SQW emission and is mainly due to inhomogeneously broadening of the physical dot size. Even though InGaAs SK QDs are known to hold at least two confined states, the luminescence is assumed to mainly originate from the lowest state due to the low excitation density in the experiment. All samples thus show a successive increase of the PL bandwidth from 2 D to 0 D confinement.

Further investigations on the SML:Sb$_{1060}$ bimodal emission is performed by analyzing the temperature dependence of the luminescence peak, plotted in Figure 4.4 (a). Time-integrated PL spectra were recorded at sample temperatures increasing from 4 to 280 K at an excitation intensity of 100 W/cm^2. While the peak shift represents a measure for the phononic environment, the total emitted power provides an indication for the depth of the electron potential traps. The emission peak of the Sb:SML$_{1060}$ sample at 4 K is located around 1.22 eV and shifts up to 1.17 eV at room temperature. Within the low temperature range the peak shift further follows an S-shape, which has been reported in the lirterature for different SML samples and is addressed to a charge carrier transfer between strongly and weakly localized states [41, 104]. For comparison data of the SQW$_{1060}$ and SML$_{1060}$ sample are plotted in the figure
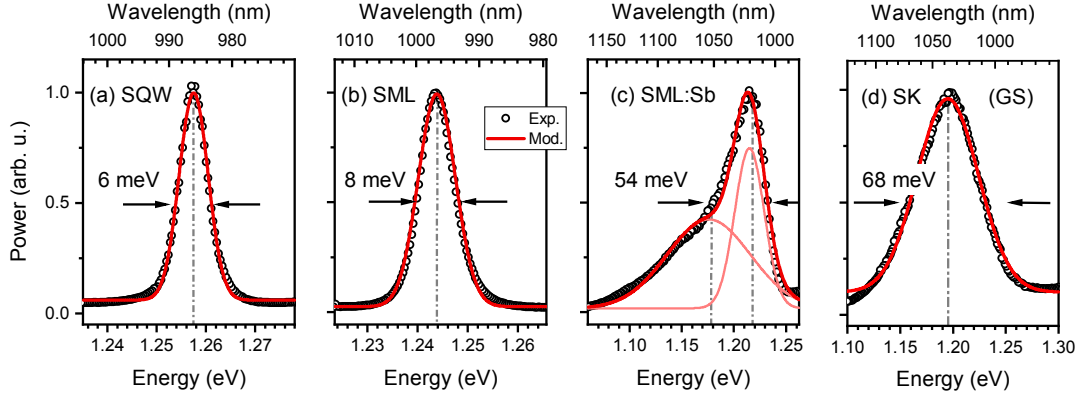
Figure 4.3.: Photoluminescence spectra of all samples from the *1060* series, taken at 4 K and excitation intensity of 100 W/cm^{-2}, showing a bandwidth increase from (a) to (d) [1].

inset, where the SML$_{1060}$ sample only shows a minor S-shape, which is absent at all for the SQW$_{1060}$ sample.

This further supports the previous assumption of a heterogeneous density of states of the SML:Sb material. At temperatures above 80 K the shift becomes monotonic which allows the application of the modified Varshni model after Equation 2.4. The phonon energy of $\langle \hbar\omega \rangle = 38$ meV has been determined, which is exceeds the GaAs longitudinal optical phonon $E_{ph,\,GaAs} = 35.3$ meV, as well as the value for the SML sample in subsection 2.1.2, reported to $E_{ph,\,SML} = 28.7$ meV

Further information about the energetic structure can be gathered from the temperature-dependent emission power of the SML:Sb sample. In particular the depth of potential traps can be determined by analyzing the activation energy, obtained from the temperature dependence of the total luminescence intensity. In Figure 4.4 (b) the spectrally integrated luminescence *I* has been fitted with a thermally activated quenching model after Ref. [105] using a scaling parameter *C*:

$$I(T) = \frac{I_0}{1 + C \cdot \exp(-E_A/k \cdot T)}, \tag{4.1}$$

For the calculation only data from 80 K up to room temperature was considered, thus neglecting the charge carrier transfer between strongly and weakly localized states at lower lattice temperature [41, 104]. An activation energy of E$_A$ = 45 meV has been obtained, which is also in good agreement with the energy separation indicated in Figure 4.3 (c).

In the next step time-resolved photoluminescence measurements according to section 3.1 have been performed in order to gain knowledge about exciton decay times of the SML$_{1060}$ and SML:Sb$_{1060}$ samples. The optical excitation into the GaAs barrier
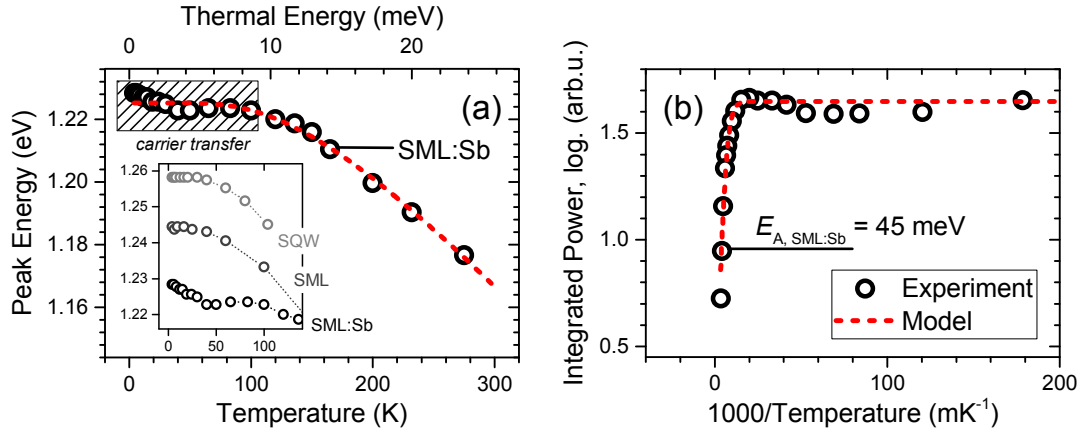
48

Figure 4.4.: (a) Obtained peak energies from photoluminescence spectra of the SML:Sb sample after optical excitation into the GaAs barrier with temperature increasing from 4 K to 280 K. Gray dots mark the center of gravity of the same data. (b) Arrhenius plot of the integrated peak power (symbols) and fit (line) [1].

at 800 nm was performed according to the setup in section 3.1. Spectral cuts of the SML and SML:Sb PL decay are visualized in Figure 4.5 (a) and (b), respectively. The data show an asymmetric decay on a ns-time scale with longer time constants for the red wing of the spectrum as compared to the blue wing. This is a common observation for SML structures and stems from the scattering of carriers between localization centers, providing an additional decay channel for carriers at higher energies [33]. This is opposed to pure capture from a reservoir for laterally uncoupled QDs, for which an even decay across all wavelengths would be expected.

The application of simple single-exponential fits to the respective intermediate decay phases was used to obtain an estimate for the carrier lifetimes, which are marked in Figure 4.5 (c) and (d) as red stars for both SML QD types. The significant decrease of the carrier lifetimes towards higher energies is typical for a Fermi-induced redistribution of coupled states after overband-excitation [106]. The obtained comparable time constants on the low energy side, in contrast, indicate the existence of decoupled states, characterized by a vanishing energy dependence.

For comparison, time constants obtained for a SML QD sample with 10 x 0.5/2.0 ML InAs/GaAs composition, according to Ref. [33], are indicated as grey dots in Figure 4.5 (c), showing comparable time constants. The decay of the low energy states of the $SML:Sb_{1060}$ sample show the longest lifetime, indicating a weaker oscillator strength as compared to the SML_{1060} sample, since the decay rate is directly linked to the overlap dipole moment of the electron and hole wavefunction.

Further, due to the nonresonant excitation into the GaAs barrier a carrier relaxation into the SML states on a timescale ranging from 80 ps for the high energy side to

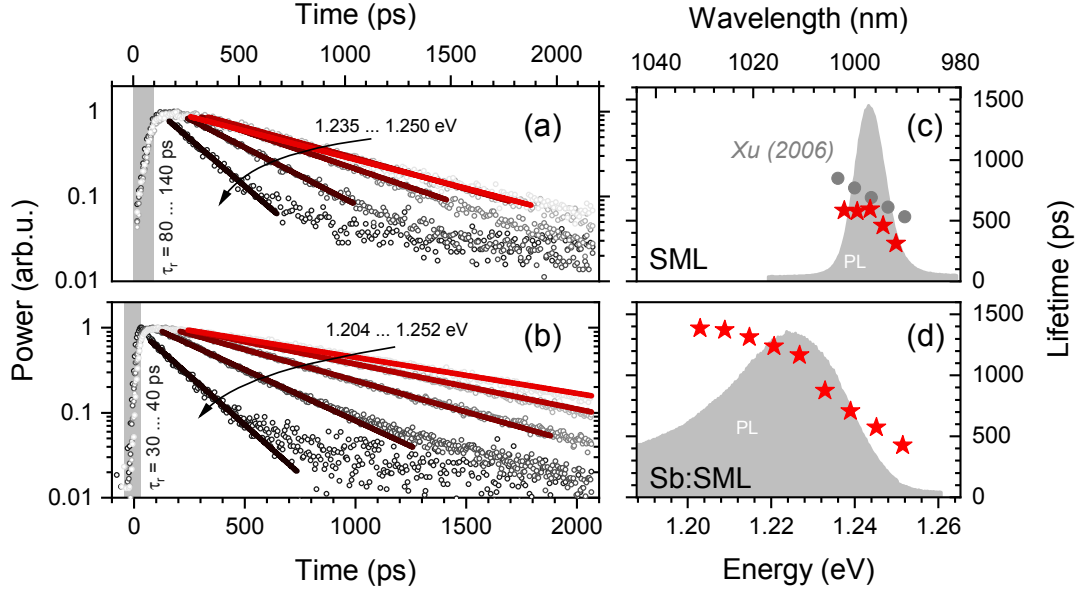Figure 4.5.: Time-resolved photoluminescence spectra of the (a) SML$_{1060}$ and (b) SML:Sb$_{1060}$ sample, respectively, after fs-pulsed optical injection into the GaAs barrier, recorded at 4 K. Dots mark experimental data, lines represent single-exponential fits to estimate the carrier lifetimes. The obtained time constants for both samples are indicated in (c) and (d), respectively.

140 ps for the low energy side was obtained. However the SML:Sb sample shows a more efficient capture on a time scale below the temporal resolution limit of 35 ps with. Assuming that the thermalization and relaxation of the 3D GaAs reservoir happens on a much faster time scale the rise time mainly reflects the capture processes into the dots and thus is a measure for the Auger scattering coefficient, which tends to be at least a factor of 3 larger in Sb:SML than in SML agglomerations. This effect might be attributed to the Sb-induced increased hole-confinement, which leads to a reduced hole-mobility and thus more efficient electron-hole recombination process.

Part II.

Device Applications

The second part of this thesis, contains studies for the application of submonolayer quantum dots as active medium in optoelectronic devices. At first in chapter 5 a study of the gain dynamics of semiconductor optical amplifiers based on submonolayer grown quantum dots is presented, revealing ultrafast recovery and a large nonlinear optical response. Results from this chapter were mainly published in Refs. [1], [2] and [4]. A combined study on lasers based on different types of submonolayer quantum dots, as compared to quantum well lasers is presented in the next chapter. The observation of large material gain and increased gain bandwidth of dots alloyed with antimony is discussed, which was published in Ref. [1]. The large amplitude-phase coupling in terms of the α-parameter was found in samples from the *960*-series, as well as from the *1060*-series, enabling to drive the devices into a regime of chaotic oscillations. Thus in the last chapter a study on feedback-induced laserdynamics is presented, showing regimes of weak and strong chaos.

5. Semiconductor Optical Amplifiers

As introduced earlier in subsection 2.2.4 zero dimensionally confined structures have proven favorable properties regarding the gain dynamics during optical light amplification. The strong carrier localization in those structures leads to an efficient assistance of radiative carrier recombination, as compared to higher dimensional structures like QW or bulk material. However, amplification in devices based on SML QDs has hitherto not been studied. In this chapter the gain dynamics of SOAs based on InAs/GaAs and InAs:Sb/GaAs SML QDs are investigated by time resolved pump probe measurements, revealing significantly different carrier relaxation pathways as compared to typical SK QDs. The following points will be treated:

- The gain recovery for resonant and off-resonant pulse amplification in InAs/GaAs SML QD SOAs mainly takes place on a single digit ps time scale.

- The underlying DOS and corresponding carrier relaxation pathways of the active region is formed by an extended Gaussian effective exciton state, surrounded by a cloud of inactive states, which are both fed by a 3 D carrier reservoir formed by the GaAs bulk material.

- Significant changes of the spectral and recovery dynamics for InAs/GaAs:Sb SML QD based SOAs occur due to the a bimodal exciton state distribution of the active region, containing deeper bound states.

- A large amplitude-phase coupling in terms of the α-parameter

5.1. Fast Gain Recovery and Large Optical Nonlinearities

The complex gain recovery dynamics of the SML_{960} SOAs have been investigated via heterodyne detected pump probe measurements according to subsection 3.4.2. At
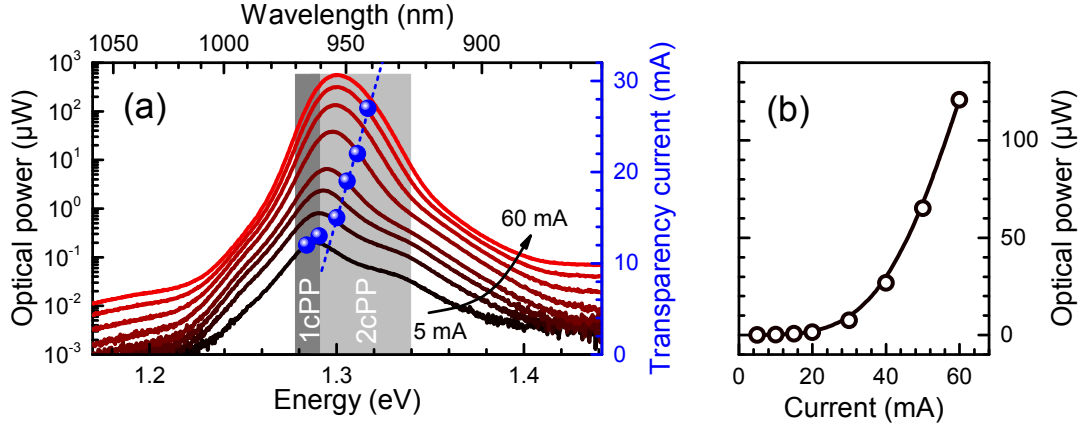
Figure 5.1.: (a) ASE spectra of an SML$_{960}$ SOA for injection currents ranging from 5 to 60 mA plotted as red lines. Gray areas mark the spectral range of one- and two-color pump-probe experiments. The spectrally dependend transparency current was extracted from two-color pump probe measurements and is shown as blue dots. (b) Spectrally integrated emission as a measure for the light-current characteristics [4].

first one-color pump-probe spectroscopy (1cPP) has been applied at the ASE maximum in order to extract the relevant gain and phase recovery times for amplification. Two-color pump-probe spectroscopy (2cPP) is then applied for quantification of recovery times in e.g. XGM configuration.

Figure 5.1 (a) shows the ASE spectra of a typical device of 0.5 mm length and 4 μm ridge width for injection currents I ranging from 5 to 60 mA. Dark gray areas mark the spectral window of the 1cPP measurements in subsection 5.1.1 and light gray area the scanning range of the 2cPP excitation pulse in subsection 5.1.2. Blue dots mark the obtained transparency current I_{tr}, which roughly samples the integrated number of SML QD energy states up to the excitation energy window. For the 1cPP and 2cPP measurements the pump and probe pulse powers were set to 300 μW and 30 μW, corresponding to 0.4 pJ/pulse and 4 pJ/pulse, respectively, to drive the SOA in linear operating mode. The temporal and spectral pulse FWHM were set to 250 fs and 10 nm (13 meV), respectively.

5.1.1. Gain Recovery Dynamics

According to Equation 3.10 in subsection 3.4.2, the pump-induced changes of the SOA gain $\Delta G(t)$ and the refractive index in terms of a phase change $\Delta\Phi(t)$ are obtained from relative measurements to the unperturbed system with the complex Lock-In voltage $V_0 \exp[i\Phi_0]$ via $\Delta G(t) = 10 \times \log V/V_0$ and $\Delta\Phi(t) = \Phi_0 - \Phi$. Note that due to the logarithmic expression of $\Delta G(t)$ and the exponential power law at linear
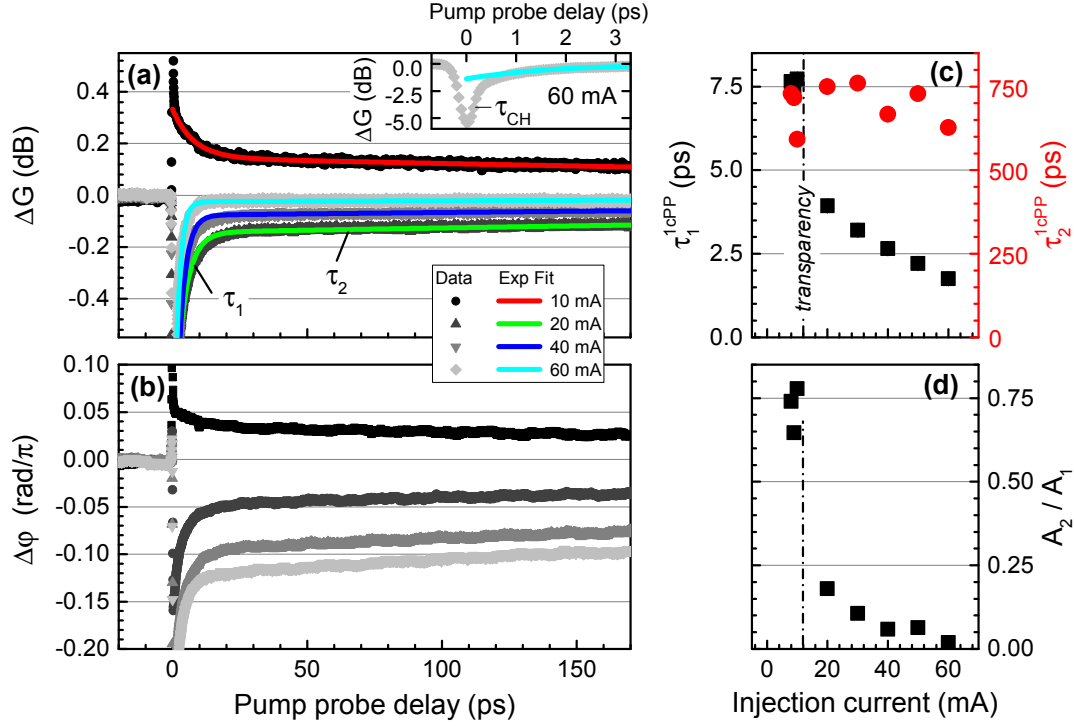
Figure 5.2.: Recovery dynamics of an SML_{960} SOA in terms of (a) gain ΔG and (b) phase $\Delta\Phi$. Gray symbols mark experimental data, lines show the biexponential fits. (c) and (d) show the obtained time constants τ_1 and τ_2 along with their amplitude ratio A_2/A_1 for different injection currents. The single color pump probe measurement was performed resonantly to the ASE peak at 965 nm [4].

amplification in Equation 2.10, this parameter can be directly interpreted as a scaled population number ΔN. The same accounts for the the refractive index modulation Δn, which is directly proportional to the phase change $\Delta\Phi$ of the transmitted pulse.

Similar to Figure 5.1 the injection current during all pump probe experiments was limited to 60 mA in order to prevent the device from degradation. This corresponds to a nominal current density of $6\,kA/cm^2$ if no current spreading was assumed, which would be significant in shallow etched QW devices [107].

The obtained gain dynamics are shown in Figure 5.2 (a) as gray symbols for the different injection currents of 10, 20, 40 and 60 mA. According to Figure 5.1 the transparency current for this wavelength range has been determined to $I_{th} = 12$ mA. Therefore, for the lowest current of 10 mA the SOAs operate in the absorbing regime, while for the higher currents it is in the state of amplification. For both regimes, the traces can be decomposed into three distinct parts, similar to those found for SK QD SOAs (see subsection 2.2.4).

(i) A sub-ps response due to coherent interaction and ultrafast carrier heating (CH) processes after SHB, as marked in the inset of Figure 5.2 (a) by τ_{CH}. These processes are below the temporal resolution of the measurement and will thus not be taken into account quantitatively.

(ii) A single digit ps recovery, which reflects the refilling of the depleted states by nearby carriers. As the term *nearby carriers* contains a lot of physics and plays the most important role regarding acceleration of gain recovery in SOAs, it will be studied later in more detail. The corresponding time constant is indicated as τ_1.

(iii) The long-time recovery τ_2 denotes the equilibration of the entire carrier density by electrical injection and is mainly driven by reservoir refilling processes.

Hence the gain traces $\Delta G(t)$ were phenomenologically fitted by a sum of exponential functions neglecting the CH process τ_{CH}. Applying the individual amplitudes A_1 and A_2 for the respective processes, the function reads:

$$\Delta G(t) = A_1 \exp\left(-t/\tau_1\right) + A_2 \exp\left(-t/\tau_2\right). \tag{5.1}$$

The fit results are plotted in Figure 5.2 (a) as solid lines and the results for the time constants accompanied by their amplitude ratios are listed in (c) and (d) for different injection currents, respectively. The designation *1cPP* implies a resonant measurement, meaning the absence of cross gain or phase modulation effects (XGM or XPM).

The fast recovery constant, plotted as black symbols, has been found in the range of 6 to 8 ps for the absorption regime, accelerating to values down to 2 ps in the case of amplification. In comparison, typical QW based devices show recovery times in the order of 10 ps, as the depleted states are solely refilled by the surrounding barrier material acting as carrier resevoir, leading to an additional diffusion step [108, 109]. This step seems to be absent in case of the InAs/GaAs SML QDs, indicating a different potential landscape from standard QWs. On the contrary this efficient capture process is an evidence for lower dimensionality, similar to, e.g., dot-in-a-well structures. Those can be efficiently filled with carriers accumulated at higher energies in either the QD ES or states of the embedding QW, from which they can efficiently feed the depleted states on a few-ps time scale [9, 110].

As a consequence the more DWELL-like rather than QW-like recovery suggests the existence of an efficent carrier reservoir feeding the SML QD states. However, following subsection 2.1.2 a deeper interpretation might be found regarding the effect of heteroconfinement [50]. As in similar structures the high degree of localization for

the hole wavefunction, accompanied by the extended electron wavefunction has been observed, a similar effect for the *960*-sample series can be assumed. Thus an efficient coupling of neighboring SML islands might cause a fast response to changes in the carrier occupation caused by the creation or annihilation of an exciton. Clarification will be provided after modeling the data, which will be shown later in this work (see section 5.2). The slow time constant τ_2, describing the carrier injection of the complete electronic system is plotted in Figure 5.2 (c). It has been determined to be about 600-800 ps, showing only little dependence on the injection current. However, its amplitude as compared to the fast time constant decreases with higher currents above transparency to values below 5 %, as shown in (d).

Roughly similar dynamics are observed for the long-term recovery of phase or rather the refractive index modulation, shown in Figure 5.2 (b). As the refractive index is influenced not only by the participating carriers the coherent processes, but rather the entity of the electronic system, its dynamics are mainly driven by the carrier reservoir occupation number. Further, the phase dynamics can not easily be attributed to exponential time constants, therefore no fit is applied in this work.

5.1.2. Cross Gain Modulation

To probe the potential of the InAs/GaAs SML QDs for cross gain modulation, two color pump probe spectroscopy has been applied to the SML_{960} SOAs. To this end, the probe pulse was left in resonance to the ASE peak, while the pump was blue shifted up to 940 nm towards the blue shoulder of the emission spectra, as indicated in Figure 5.1. As stated earlier, the transparency current I_{tr} roughly samples the number of energy states up to the pump energy window and thus increases for shorter wavelengths. As a consequence different injection currents belong to different regimes, as shown in Figure 5.3 (a)-(c) for the absorption, transparency, and amplification regime, respectively. In the figure all curves were normalized for better comparability of the weights of fast and slow relaxation component.

Similar to the phase dynamics, the slow recovery component obtained from these 2cPP measurements is mainly determined by the carrier reservoir and consequently it is comparable for all measurements. Hence the traces are limited to the first ten picoseconds after the pump probe overlap. The fitted recovery time constants τ_1^{2cPP} are shown in Figure 5.3 (d), accompanied by their respective amplitude ratios A_2/A_1 in (e). The time constants follow the trend of the 1cPP experiments accelerating down to 2 ps from absorption the the amplification regime. Spectrally the fastest dynamics are reached in case of resonant pulses, which can be traced back to the additional diffusion process, needed for recombination after off-resonant excitation. Despite the
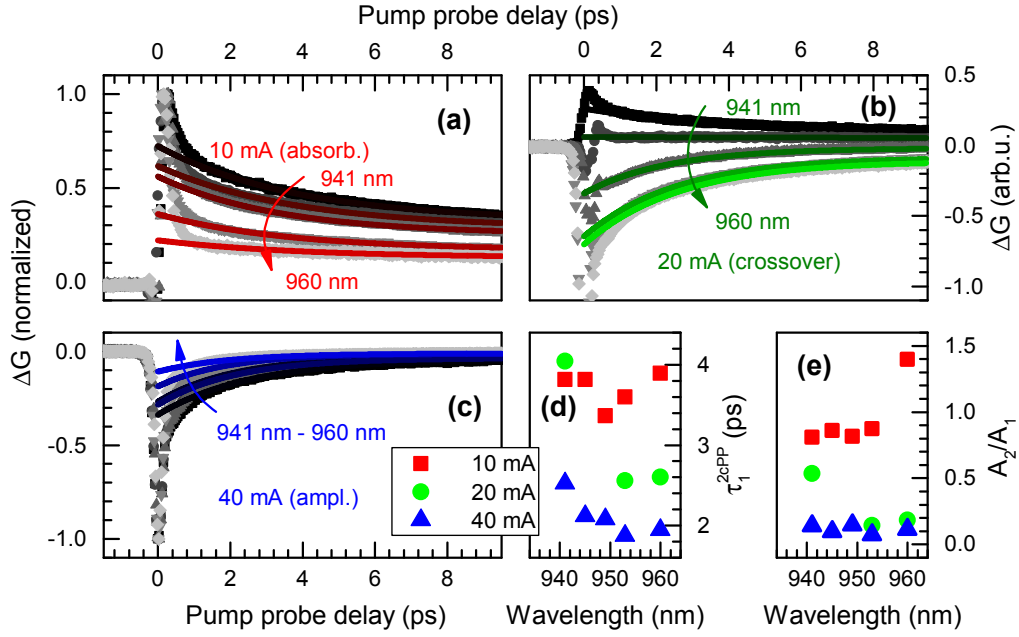
Figure 5.3.: Intraband gain recovery dynamics of an SML SOA from the *960*-series, measured via two color pump probe experiments, probing the ASE peak at 960 nm and pumping at higher energies up to the wavelength of 941 nm. Different regimes are entered due to the wavelength dependency of the transparency current in terms of (a) absorbtion, (b) crossover, and (c) amplification. (d) Time constants τ_1^{2cPP} and (e) amplitude ratios A_2/A_1 [4].

fast recovery, the amplitude ratio, shown in Figure 5.3 (d) reveals a major influence of the slow component in terms of the reservoir dynamics τ_2 for the absorbing regime. In case of amplification, this component plays only a minor role.

Comparable experiments have been applied to SK QD SOAs in order to coherently probe the underlying energy structure [7]. This *gain excitation spectroscopy* revealed mixed states between confined states and the surrounding reservoir material, referred to as *crossed excitons* [49]. However, in contrast to the results found for SML QDs, those states do not dominate the dynamics of SK QDs.

5.2. Carrier Relaxation Pathways

To gain deeper insight into microscopic processes and carrier relaxation within the potential landscape, the resonant recovery from subsection 5.1.1 in its full complexity of gain and phase is analyzed via a microscopically motivated rate equation modelling by B. Lingnau (TU Berlin) [2]. As stated previously, the explanation for the fast state refilling τ_1 in Figure 5.2 is of high interest, as it plays the biggest role for the SOA dynamics.
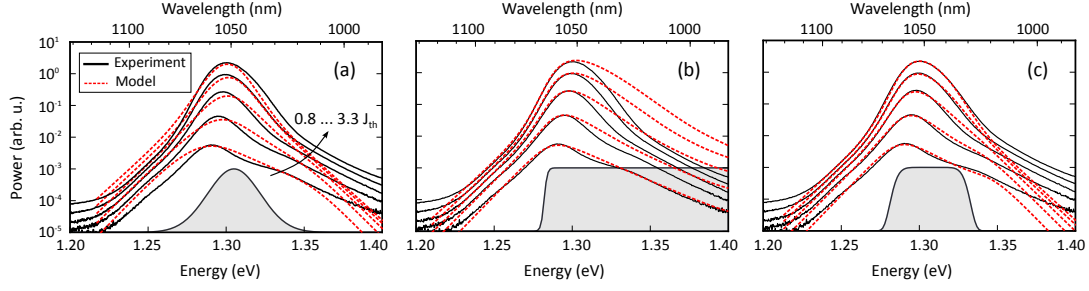
Figure 5.4.: Measured (solid lines) and simulated (dashed lines) ASE spectra of an SML$_9$60 SOA. For the simulations (a) a Gaussian, (b) step-like, and (c) an extended Gaussian-like exciton [2].

To this end B. Lingnau (TU Berlin) adapted his rate equation system from subsection 2.2.4, which was originally developed for SK QD based SOAs, and applied it to the experimentally obtained amplitude and phase dynamics of the SML$_{960}$ SOA. As a starting point the twofold state distribution of SK QDs by means of the QD GS N_{GS}^j and ES N_{ES}^j were replaced with an SML distribution N_{SML}^j. Initially the scattering rates remain the same, while the SML distribution has to be determined. To this end the ASE spectra in Figure 5.1 had to be modeled first.

The ASE spectra $P(E, z)$ were calculated via integration of a spontaneous emission source term $R(E)$ and the optical gain $G(E)$ along the device length L:

$$\frac{d}{dz}P(E, z) = R(E) + G(E)\, P(E, z) \tag{5.2}$$

$$P(E, z) = R(E)\frac{\exp\left[G(E)\, L\right] - 1}{G(E)\, L} \tag{5.3}$$

As $R(E)$ and $G(E)$ are directly linked to the distribution of optically active states f^j (see Equation 2.16), the carrier DOS can be finally determined after testing different variations of f^j. Taking into account the carrier heteroconfinement (see subsection 2.1.2) it seems reasonable to first test a typical 0 D as well as a 2 D like distribution.

Figure 5.4 (a) shows the result after application of a Gaussian DOS, as it is known for a inhomogeneously broadened SK QD ensemble. Apparently that model is not able to capture all features of the measured spectra, as it overestimates the low energy side while underestimating the high energy tail. Additionally the decay dip around 1.31 eV is not captured as well. As a next step in Figure 5.4 (b) a thermally broadened step-like DOS is assumed, as it is typical for QW structures. Whilst this distribution offers a good agreement on the low energy side, the high energy side becomes dra-
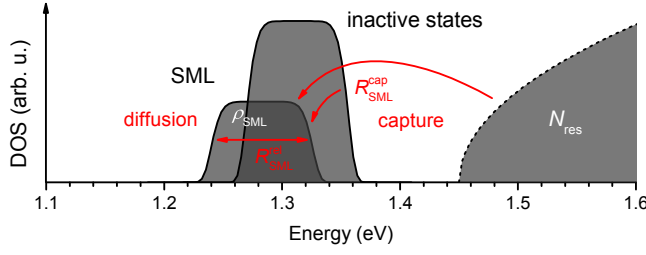
Figure 5.5: Sketch of the DOS and carrier relaxation pathways used for modelling of the InAs/GaAs SML QDs at room temperature. Inactive states in terms of free carriers form efficient carrier reservoir without providing optical gain [2].

matically overestimated and the decay dip at 1.31 eV is absent as well.

Thus the failure of either a purely 0D or 2D DOS are obvious and a solution might be found in between. In order to merge both systems into an analytic DOS, the attempt of modeling an extended Gaussian distribution has been made, which is plotted in Figure 5.4 (c). This function combines the carrier localization in terms of an absent high-energy tail and the nearly constant DOS of 2D systems by an broadened plateau at the peak. Assuming an inhomogeneous broadening ΔE_{inh} for the SML states $E^j_{SML} = \hbar\omega^j_{SML}$ around the central energy E_{SML}, this distribution is expressed by:

$$f^j = \mathcal{N}^{-1}\left[-4\ln 2\left(\frac{\hbar\omega^j_{SML} - E_{SML}}{\Delta E^{inh}_{SML}}\right)^8\right],\qquad(5.4)$$

capturing most features of the ASE spectra. Solely the high energy tail is slightly underestimated, which is in the order of below -10 dB. Potentially the exact DOS might have been found after reverse engineering the ASE spectra. However, in order to minimize calculation efforts and due to the almost neglectible deviation of the extended Gaussian function to the measurement, this result is considered sufficient for this work.

The carrier reservoir was determined according to Wilms et al. [111] at the temporal point at which the gain recovery changes from local refilling to full equilibrium. According to the previous section this point denotes the transition from τ_1 to τ_2, which for the SML QDs happens after approximately 10 ps. Microscopically determined scattering rates from a 2D as well as a 3D reservoir into QD states revealed a linear current dependence for the former, while the latter shows quadratic growth. To model the data correctly, a current-dependent capture rate hat to be assumed after:

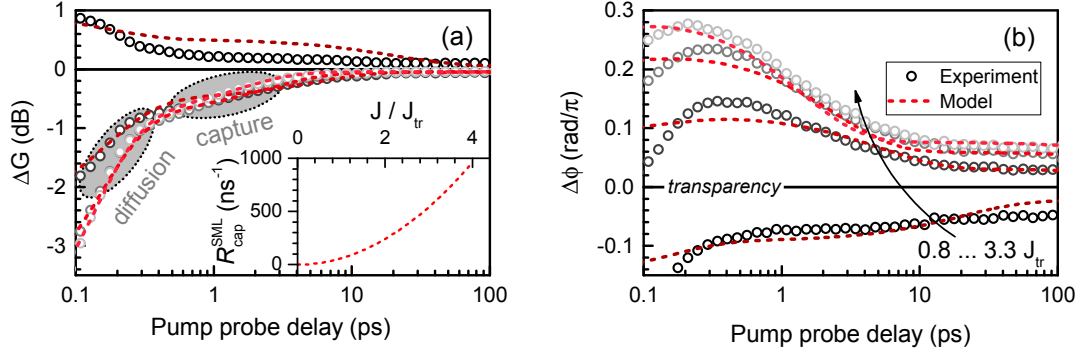$$R_{cap} = 60\ ns^{-1}\left[\frac{J}{J_{tr}}\right]^2\qquad(5.5)$$

59

Figure 5.6.: Modelled pump probe spectra in terms of (a) gain and (b) phase recovery of a SML QD SOA from the *960*-sample series via a coupled rate equation system. Areas of diffusion and carrier capture are marked for the gain recovery. The large phase shift of up to 0.3 π can only be captured assuming a large amount of optically inactive states. The inset in (a) shows the modelled quadratic dependence of the capture rate with the injection current J [2].

with the transparency current J_{tr}, plotted as inset in Figure 5.6 (a), assuming the GaAs barrier surrounding the SML QD layers as a 3D carrier reservoir.

Inactive states have been revealed from the phase response, showing extremely large values, as compared to a SK QD SOA, which is shown in Figure 5.2 (b). The ratio of the phase response for both SOAs $\Delta\Phi_{SML}/\Delta\Phi_{SK}$ accounts for values in the range 10 to 20 at all recovery times, suggesting the presence of states, not contributing to the coherent processes, but influencing the refractive index. This happens e.g. via free carrier absorption of dissociated excitons or non-radiative recombination at trap states. In order to capture these processes it is necessary to add an additional contribution named *inactive states* into the model.

The full rate equation system is illustrated in Figure 5.5, showing the obtained state distribution and the respective scattering channels. Putting all parts together the system reads as follows:

$$\frac{\partial}{\partial t}N_{Res} = J - \frac{N^{Res}}{\tau_{Res}} - 2N_{SML}\sum_j f^j R_{cap}(j) \tag{5.6}$$

$$\frac{\partial}{\partial t}N^j_{SML} = -\frac{(N^j_{SML})^2}{\tau_{SML}} + R_{cap}(j) + R_{rel}(j) + R_{stim}(j). \tag{5.7}$$

with microscopically obtained scattering rates similar to Equation 2.17. A good agreement with the complex pump probe data from the previous section is visual-

ized in Figure 5.6. Owing to the model a number of conclusions about the physical processes within the SML QD system can be drawn, which is summarized in the following:

(i) The SML states are fed directly by the GaAs barrier and a number of inactive states, formed by a cloud of unbound carriers. The latter represent a way faster recovery channel than the former, as it is also the case for the QW of SK DWELL structures.

(ii) The inactive states enable a large phase response as compared to a SK QD or QW based active medium.

(iii) Even though the carriers are bound heterogeneously, the fast recovery dynamics are mainly driven by the localized holes, forcing their delocalized counterparts to follow.

As a result, the gain recovery of SML QD SOAs is considered to compete with the time scales of SK QD SOAs. However, the large phase response presents a main difference between both and will be investigated further in this work.

5.3. Broadband Amplification in SML:Sb SOAs

To proceed, the same experiment has been performed for the SML:Sb based SOAs from the *1060*-sample series. As shown previously in section 4.2 SML structures show a dramatic increase of their emission bandwidth after alloy with Sb and there is reason to presume an at least bimodal exciton state distribution. To gain more clarity, the recovery dynamics of an SML:Sb based SOA of 0.5 mm length, with a 3 μm ridge is analyzed.

5.3.1. Carrier Localization

The gain recovery after amplification of a pump pulse, spectrally centered at the ASE maximum around $\lambda = 1060$ nm, is shown in Figure 5.7 (a) as open symbols for different injection currents and on a logarithmic time scale. The transparency current at this particular wavelength has been determined to $I_{tr} = 47$ mA, which is about four times larger than for the SML$_{960}$ SOAs. Assuming neglectible current leakage through the waveguide structure, this rise of I_{tr} can only be caused by either a large resonant excitable DOS or the necessity of refilling deeper exciton states or carrier traps.
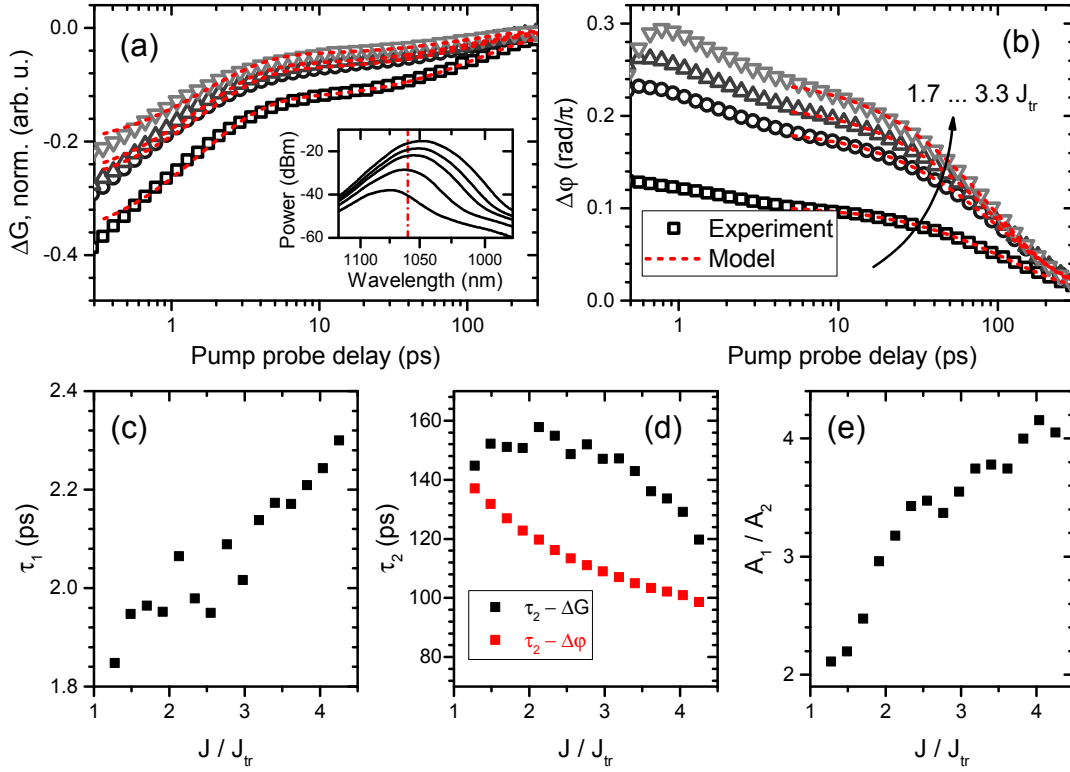
Figure 5.7.: (a) Gain and (b) phase recovery dynamics of an amplifying SML:Sb QD SOA from the *1060*-series obtained via single color pump probe resonantly to the ASE peak (inset). The gain recovery can be well approximated by a biexponential decay with (c) τ_1 and (d) τ_1 being the fast and slow decay component and (e) A_1/A_2 their respective amplitude ratio. [1]

Analogous to the InAs/GaAs SML based device, the gain recovery is decomposed into two regions of exponential decay with the time constants τ_1 and τ_2, plotted in Figure 5.7 (c) and (d). Again those are attributed to a fast inter-dot capture process and to state-refilling from the carrier reservoir, respectively. Remarkably, both time constants are faster than the ones found in Sb-free SML SOAs, with τ_1 slowing down with increasing current and τ_2 accelerating while losing influence. The latter refers to the amplitude ratio $A_1/A2$ of both processes, plotted in Figure 5.7 (e).

Although the recovery traces of both, the SML_{960} and the $SML:Sb_{1060}$ SOAs, can be approximated by a biexponential decay function, qualitative differences exist in the fitted time constants and the corresponding current evolution. While the carrier diffusion previously has been found to accelerate from values around 7 ps down to 2 ps with larger injection current, the opposite appears for the SML:Sb based SOA. One attempt of physical explanation might be the saturation of a lower-energetic exciton state, fed from carriers located at the probed energy range. This lowest state appears to be sufficiently small in order to saturate at moderate currents thus drawing signif-
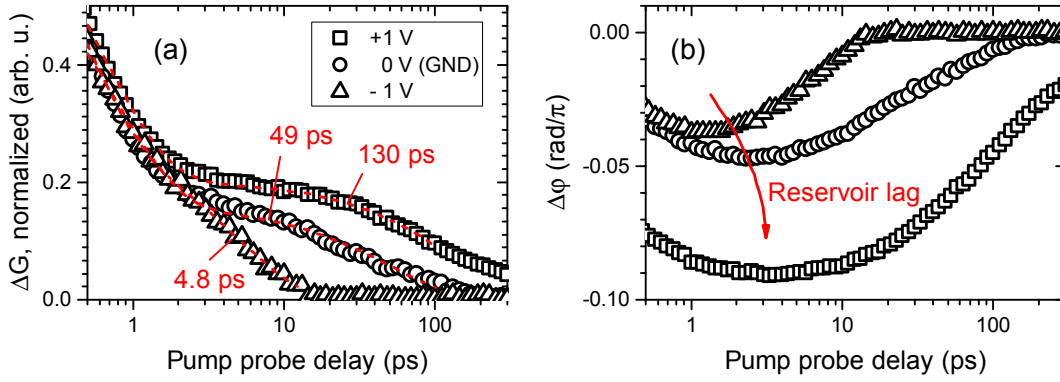
Figure 5.8.: (a) Gain and (b) phase dynamics of an SML:Sb SOA in +1 V forward bias, ground potential, and -1 V reverse bias, respectively.

icant influence on the system. This further supports the assumption of an additional exciton state of high localization on the red shoulder of the emission spectra around 1100 nm.

The phase dynamics in Figure 5.7 (b) shows a growing response for high injection current, reaching a peak value of 0.3 π at 3.3 J_{tr}, which is a comparable amount as to the SML SOA from the previous section. The phase the maximum phase shift appears within the first ps after the pulse amplification, showing slower built-up for higher currents. For greater delay times the temporal evolution follows a strict single exponential decay with time constants in the 100 ps range, plotted in Figure 5.7 (d). As amplitude and phase show comparable recovery constants at long delay times, they might be attributed to the same refill processes, mainly determined by direct capture from the 3D GaAs barrier.

5.3.2. Response Broadening

While the Sb-system requires a larger current density for transparency, it also enables faster gain recovery dynamics as compared to the unalloyed SML QD system. A further feature of SML:Sb SOAs is the broadened gain spectrum, as shown in section 4.2. Hence to proceed, in this section the response to an incoupled optical pulse is analyzed for an absorbing SOA state. To this end the SOAs are reverse biased in order to support exciton dissociation and carrier transport from the active region to the doped areas of the devices. This allows to probe the absorption cross section and thus the spectral response, as well as the exciton dissociation time scales, important for e.g. detector applications.

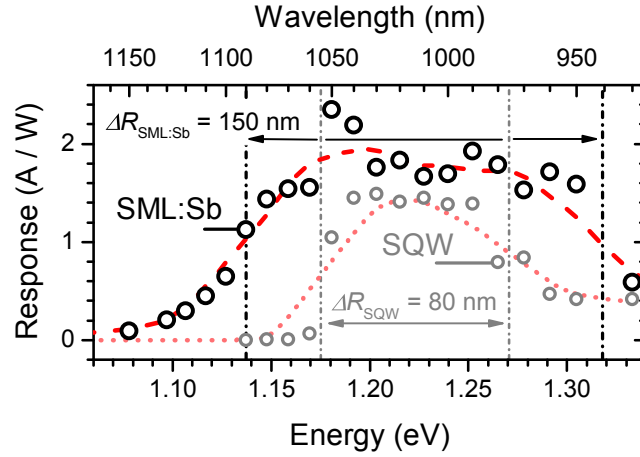The gain and phase dynamics of an SML:Sb SOA at +1 V / GND / -1 V bias is shown

Figure 5.9.: Spectral response of an SML:Sb SOA in comparison to an SQW SOA at -1 V bias and 10 nm excitation bandwidth. Dots mark experimental data, dashed lines sketch the envelope as a guide to the eye, ΔR marks the response bandwidth. [1].

in Figure 5.8 (a) and (b), respectively. A brief estimate for the ionizability of optically induced excitons within the active region leads to the assumption that a reverse bias of -1 V already ensures sufficient carrier transport. Typically optical detectors are biased at -1 ... -5 V, according to the design and break through voltage. In contrast to the amplification regime of previous section, the capture processes τ_2 rather than the carrier diffusion τ_1 shall be considered in here.

Unlike before for the amplification regime, gain and phase dynamics are no longer synchronized in absorption mode. While some carriers tend to dissociate due to band bending, a reverse bias even accelerates carrier recovery by aspirating optically induced charge carriers. The extracted time constants in Figure 5.8 (a) drop down more than one order of magnitude from 130 ps at +1 V to 5 ps at -1 V. However, (b) shows that the phase dynamics lags behind the gain, as the phase is also able to sample of resonant charge carriers, which do not contribute the optical gain. Regarding both quantities, the system becomes completely stable in less than 20 ps when reverse biased at -1 V, which is a promising result for detector application, enabling an at least >50 GHz bandwidth.

Retaining at a fixed reverse bias of -1 V the broadband response R of an SML:Sb SOA is measured via incoupling of a tunable external optical pulse with a fixed power of P_{in} = 30 μW. The response is a measure for the efficiency of actual photodetectors and it relates the induced photocurrent I to the excitation power via

$$I(\lambda) = R(\lambda) \cdot P_{in}. \tag{5.8}$$

Figure 5.9 shows the obtained response at different excitation wavelengths. The
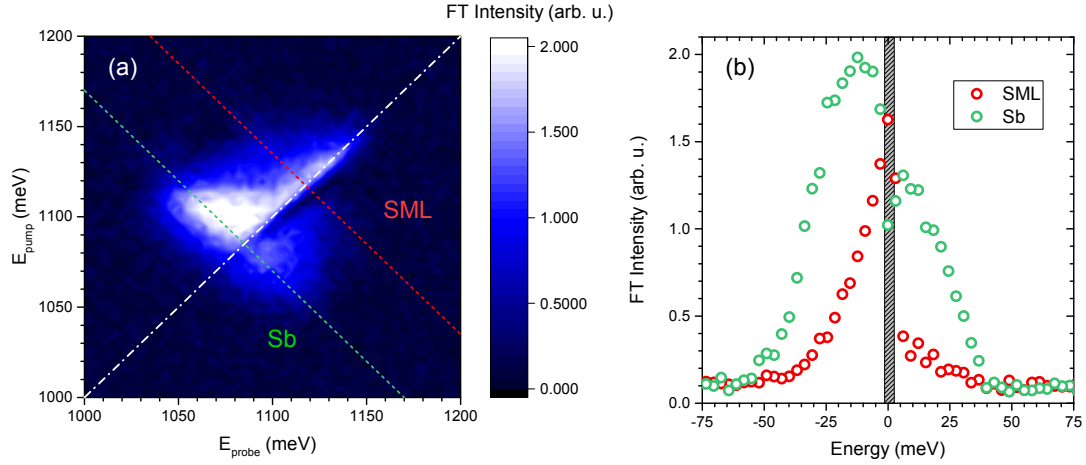
Figure 5.10.: Room-temperature 2D spectrum of an SML:Sb QD SOA with two distinct coherent states: SML and Sb. (a) Amplitude spectrograph, (b) off-diagonal cuts.

SML:Sb SOA shows a large bandwidth of roughly $\Delta R = 150$ nm (180 meV) with a slight peak around 1050 nm accompanied by a plateau up to 950 nm. For comparison the same measurement has been applied to an SQW_{1060} SOA, showing a response bandwidth of 80 nm (95 meV), which is roughly half the width as compared to the SML:Sb based device. As mentioned before the assumption of an at least bimodal state distribution seems legit, with the spectral response peak indicating the intersection of lower and higher energy states in the SML:Sb QDs. Furthermore the enlarged response bandwidth accompanied by the fast response time scale are promising features for possible semiconductor photodetector applications [112].

5.3.3. Coherent Coupling

As introduced in subsection 3.4.3, two-dimensional white light spectroscopy offers a convenient way to identify and measure coherent states of optical materials embedded in waveguide structures. To this end, the SML:Sb SOAs from previous chapter with shortest cavity lengths were used for this measurement, in order to minimize accumulated absorption losses. The top-p contact of the devices was set to GND potential, providing a completely unexcited electronic system before pulse arrival. The pulses were spectrally centered around 1060 nm with a FWHM of roughly 150 nm in order to capture the major part of both assumed states.

The spectrograph in Figure 5.10 (a) shows the amplitude intensity spectra of an unbiased SML:Sb SOA after Fourier transformation of the FWM signal. The white dash-dotted line marks the diagonal, containing coherent states and their inhomogeneous broadening. In the spectrograph two distinct exciton states have been observed,

Figure 5.11: Sketch of the DOS and carrier relaxation pathways used for modelling the InAs/GaAs:Sb SML QD dynamics. A deeper Sb-induced Gaussian-distributed state has been added to the previous SML model [1].
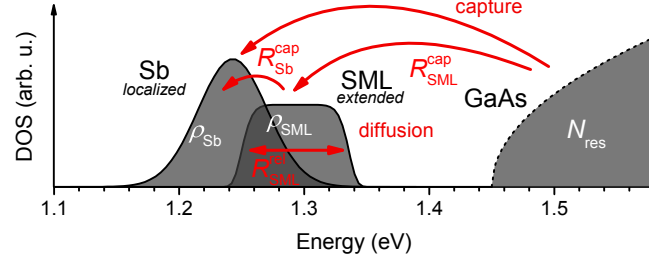
which will be denoted as SML and Sb states in the following.

5.4. Modeling the SML:Sb QD DOS

Following the accumulation of numerous hints at a dual state distribution in Sb-alloyed SML QDs, this point will be examined in more detail in this sections. Initially, two-dimensional coherent spectroscopy has been used to identify both states and their coupling. By means of an extension to the SML QD rate equation system, the PL data from Figure 4.5 was fitted and decay parameters were obtained.

It seems reasonable that both distinct states originate from two different exciton types with different carrier distributions. As visible from the 4 K time-resolved PL spectra in Figure 4.5, an efficient decay channel is assumed on the blue spectral side, while a long living tail remains on the red side. Assuming that the Sb incorporation adds new states to the InAs/GaAs SML system rather than a modification, the deeper states may originate solely from the alloy. Since the fitting in section 4.2 was not sufficient to capture the exact QD DOS, the SML model in section 5.2 had to be adapted to the SML:Sb system by B. Lingnau (TU Berlin).

Starting from the bimodal assumption, the SML QD DOS in Figure 5.5 was extended by means of a deeper Gaussian-distributed exciton state, as sketched in Figure 5.11 [1]. The different states are denoted as *SML* and *Sb* with the former describing the extended exciton wavefunction from the SML model and the latter a deeper and more localized state, induced by the Sb-alloy. Even though an increased localization generally results into larger confinement energy, the Sb state is assumed to be deeper due to the Sb-induced reduced effective bandwidth.

Like for the original SML DOS charge carriers from the bulk reservoir N_{Res} can be captured into the SML states N_{SML} with an effective rate $R_{cap} = R_{cap}^{SML}$, according to Equation 5.5. As the latter depends on the reservoir carrier density, the carrier distribution f is specified by the physical reservoir size h_{Res} and the energy dependent
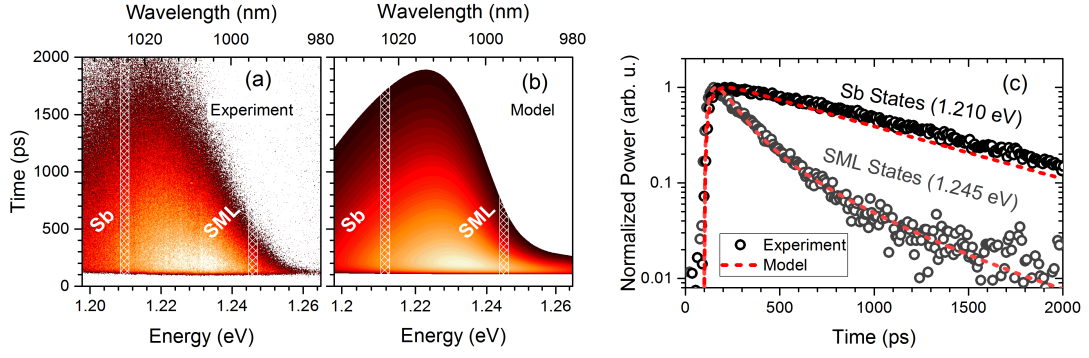
Figure 5.12.: Temporally and spectrally resolved photoluminescence of the SML:Sb sample at a temperature of 4 K and optical excitation into the GaAs barrier. (a) Measured data, (b) modeled data, and (c) the comparison of both in spectral cuts. [1].

SML DOS $\mathcal{D}_{SML}$ via:

$$f(E) = \frac{\mathcal{D}_{SML}(E)}{h_{Res}}. \tag{5.9}$$

Further the ultrafast lateral scattering rate R_{rel} was taken from previous model as well and a cascade capture into the lowest Sb states N_{Sb} is assumed. Even though a direct capture into the Sb states can not be excluded, it can be neglected due to the larger energy separation and consequently decreased rate by more than one order of magnitude.

Converting from discrete approximation to a continuous energy distribution according to the full DOS in Figure 5.11 leads to the following rate equation system [1]:

$$\frac{\partial}{\partial t}N_{Res} = J - \frac{N_{Res}}{\tau_{Res}} - \int \frac{\mathcal{D}_{SML}(E)}{h_{Res}}R_{cap}^{SML}(E)\,dE\,, \tag{5.10}$$

$$\frac{\partial}{\partial t}\rho_{SML}(E) = -\frac{\rho_{SML}(E)}{\tau_{SML}} + R_{cap}^{SML}(E) + R_{rel}^{SML}(E) - \int \frac{\mathcal{D}_{Sb}(E')}{N_{SML}}R_{cap}^{Sb}(E,E')\,dE'\,, \tag{5.11}$$

$$\frac{\partial}{\partial t}\rho_{Sb}(E) = -\frac{\rho_{Sb}(E)}{\tau_{Sb}} + \int \frac{\mathcal{D}_{SML}(\tilde{E})}{N_{SML}}R_{cap}^{Sb}(\tilde{E},E)\,d\tilde{E}\,. \tag{5.12}$$

Proceeding, this model is applied to the SML:Sb$_{1060}$ time-resolved PL data. Even though describing laser rate equations, the model is valid for dynamics of any charge carrier distribution, even without waveguide-supported coupling. In case of the wafer piece PL samples from the *1060*-sample series, no current can be applied. Instead, *J* translates into a time-dependent Gaussian source term in the carrier reservoir with a temporal FWHM of 230 fs. In contrast to section 5.2, the photoluminescence spectra $S(E)$ are calculated from the time-resolved charge carrier distributions $\mathcal{D}_m$, with *m*

Table 5.1.: Parameters used in the simulations of the SML:Sb luminescence by B. Lingnau.

Quantity	Symbol	Value	
Bulk lifetime	τ_{Res}	1 ns	[2]
SML lifetime	τ_{SML}	0.8 ns	[2]
Sb lifetime	τ_{Sb}	0.8 ns	[1]
SML inhom. width	ΔE_{SML}^{inhom}	50 meV	[1]
Sb inhom. width	ΔE_{Sb}^{inhom}	65 meV	[1]
SML areal density	N_{SML}	$3.5 \cdot 10^{11}$ cm^{-2}	[2]
Sb areal density	N_{Sb}	$0.7 \cdot 10^{11}$ cm^{-2}	[1]
Capture rate into SML	$R_{SML}^{cap}(J)$	60 ns$^{-1} \times (J/J_{tr})^2$	[2]
Diffusive SML scatt. rate	R_{SML}^{rel}	3.5 ps^{-1}	[2]
Capture rate into Sb	R_{Sb}^{cap}	1 ps^{-1}	[1]
Dephasing time	T_2	150 fs	[2]

iterating over the *SML* and *Sb* states. The absence of a waveguide and excitation at normal incidence translates into a development of $L \rightarrow 0$, which lets the gain term in Equation 5.3 collapses to unity. The luminescence thus follows:

$$S(E) \propto \sum_m \int \rho_m(E') \mathcal{D}_m(E') \mathcal{L}(E' - E) \, \partial E', \qquad (5.13)$$

assuming a sech-shaped emission lineshape of each optical transition

$$\mathcal{L}(E) = \frac{T_2}{\pi \hbar} \, \text{sech}\left(\frac{T_2 E}{\hbar}\right). \qquad (5.14)$$

For applying the model and in order to reduce the number of free parameters, values from literature by means of Refs. [41] and [2] have been used. Figure 5.12 shows the simulated time-resolved PL spectra of the SML:Sb$_{1060}$ QD sample in comparison of (a) experimental and (b) modeled data at 4 K sample temperature. Subfigure (c) shows spectral cuts at the lower energetic edge of both, the SML and the Sb states. With the parameters listed in Table 5.1 the numerical model accurately reproduces the measured data, supporting the bimodal exciton assumption.

In detail the characteristic tail towards short wavelengths around 1.26 eV shortly after the excitation can be attributed to the SML states filled from the bulk charge carrier reservoir, which quickly depletes when the charge carriers scatter into the Sb states. The trapped carriers in these localized states lead to the broad and long-lived emission around 1.21 eV. Further, the broad emission also hints on a weak coupling between the emitting states, as the carriers remain trapped without thermalizing.
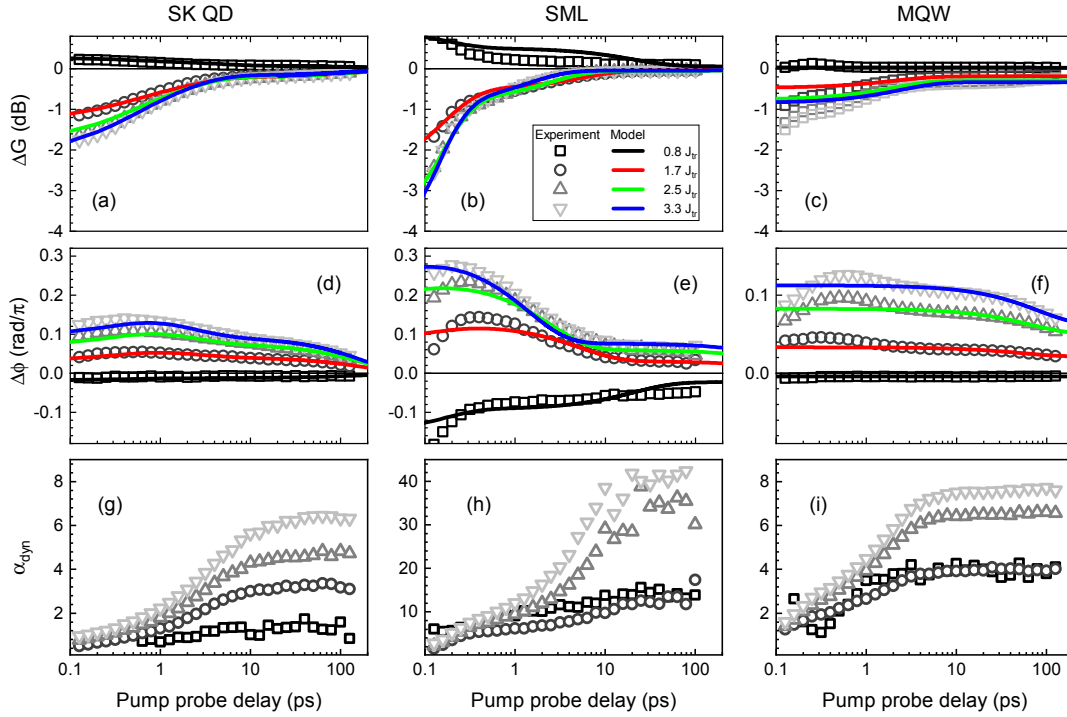
Figure 5.13.: (a) - (c) Gain and (d) - (f) phase dynamics of an SK QD, InAs/GaAs SML QD, and MQW-based SOA at four different injection currents. Open symbols mark experimental data, solid lines represent results of numerical modelling (SK, SML) or exponential fitting (MQW). (g) - (i) show the respective time traces of the obtained dynamical α-parameters [3].

5.5. Amplitude-Phase Coupling

As introduced in subsection 2.2.5 a change in absorption or gain in any optically active semiconductor waveguide intrinsically also modifies the effective refractive index. This mainly is caused by an energetic rearrangement of resonant and non-resonant carriers in the active region of the device following an optical perturbation. The coupling of the light field amplitude to its phase is characterized in terms of Henry's α-parameter [26], which has been developed from the theory of laser linewidth enhancement by Haug and Haken [113].

As discussed earlyer in many cases α does not remain a fixed parameter but rather changes with driving conditions or non-equilibrated exciton states [114, 115]. In particular during optical amplification along the waveguide of an SOA, the phase response determines weather any optical pulse is distorted or not.

Since the heterodyne-detected pump probe measurements in subsection 5.1.1 delivers both, amplitude and phase data, α can be directly retrieved. According to subsection 3.4.2 the measurement compares the complex lock-in signal in presence $V(t)$

and absence V_0 of the time-delayed pump pulse with

$$\frac{V(t)}{V_0(t)} = \frac{|V(t)|}{|V_0|} \cdot \exp^{i(\Phi(t) - \Phi_0)}, \tag{5.15}$$

considering $|V| = \sqrt{Re(V)^2 + Im(V)^2}$ and $\Phi = \arctan[Im(V)/Re(V)]$. Taking the logarithm leads to a differential intensity gain $\Delta G(t)$ on a dB scale and a phase shift $\Delta\Phi$ on a rad scale. Thus with $\Delta G \propto L\, G_{net}$ the definition of α in Equation 2.24 can be directly transformed to

$$\alpha_{dyn}(t) = -\frac{20}{\ln 10} \cdot \frac{\Delta\Phi(t)}{\Delta G(t)}, \tag{5.16}$$

where the subscript *dyn* refers to the temporal development [110, 116]. It is well known that different experimental approaches are prone to yield differing numbers for the value of α [117], and care must be taken when comparing values for the parameter obtained under different conditions.

5.5.1. Large α-Parameter in InAs/GaAs SML QDs

In a combined study the complex gain dynamics of the SML_{960} SOAs have been investigated and directly compared to SK QD and MQW based devices emitting at comparable wavelength ranges. In particular the investigated SK QD SOA has been grown with similar growth protocols to the SK QDs from the *1060*-sample series section 5.1. Results of pump-probe measurements are shown in Figure 5.13 regarding (a) - (c) differential gain and (d) - (f) phase shift for an SK QD, InAs/GaAs SML QD, and InGaAs MQW based SOA on a logarithmic time scale. Open symbols mark experimental data at four different injection currents with comparable fractions of the transparency current J_{tr}, determined to 23 mA, 12 mA and 60 mA for the SK QDs, SML QDs and QWs, respectively. Solid lines mark results of numerical modeling in case of the SK QD and SML_{960} SOA, while for the SQW device an exponential fit has been applied.

In particular, the recovery dynamics of the SK QDs in Figure 5.13 (a) and (d) shows comparable features as discussed in subsection 2.2.4 with a good agreement to the SK QD model by B. Lingnau. For the SML_{960} SOA in (b) and (e) the same data from subsection 5.1.1 has been taken and will not be discussed further at this point. The dynamics of the QW in (c) and (f), apart from a spectral hole-burning process, is
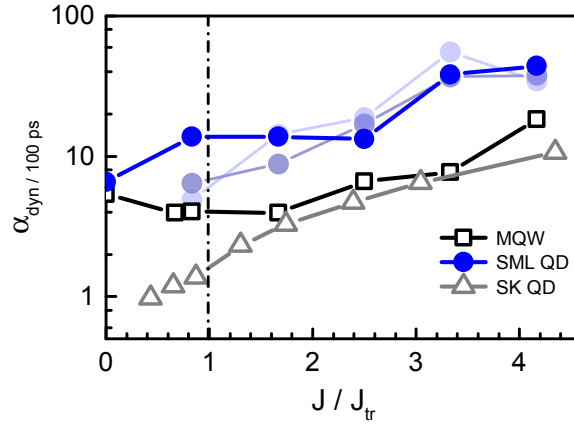
Figure 5.14.: Equilibrated values of α_{dyn} at 100 ps after perturbation for a MQW, SML QD, and SK QD based SOA with increasing injection current. Blue dots mark results for different SOAs from the SML_{960} series, processed from distinct points on the wafer [3].

reasonably well described by single-exponential fits due to the monomodal exciton structure [3]. The obtained temporal evolution of the amplitude-phase coupling is shown in Figure 5.13 (g) - (i) for all respective devices. Initially $\alpha_{dyn}(t)$ rises from low single-digit values to a maximum after around 10 ps. In general equilibrium establishes as soon as an optically induced perturbation has spread to the full electronic system regarding active states and carrier reservoir.

For comparison the equilibrium value of α_{dyn} is considered at around 100 ps after the pump-probe overlap. This is can be motivated since for practical applications, e.g. optical telecommunications, such devices are not driven in continuous mode but are rather modulated on a double-digit GHz rate. Thus the technically relevant α_{dyn} is considered by its saturation value at long delay times, as shown in Figure 5.14 for all three structures. For the SML QD based SOAs values were taken for altogether four different devices, processed from different parts of the wafer in order to illustrate the reliability of the data. Comparing all devices, the QW SOA exhibits the weakest current dependence with α_{dyn} increasing from 2.5 to 8. The SK QD based SOA, in contrast, shows values around unity at low current and moderately increases at higher injection up to comparable values as for the QW SOA. The SML QDs, however, show the highest absolute values of the α-parameter. Being still comparable to the QW at low injection current, but increasing dramatically to above 50 at 4 J_{tr}.

Comparing the SML SOA data with previous rate-equation simulations shows that the ratio of active to inactive states at energies close to the probe wavelength is giving rise to this behavior. The hetero-confined charge carriers in those QDs lead to a strong phase shift and thus refractive index modulation caused by the background of
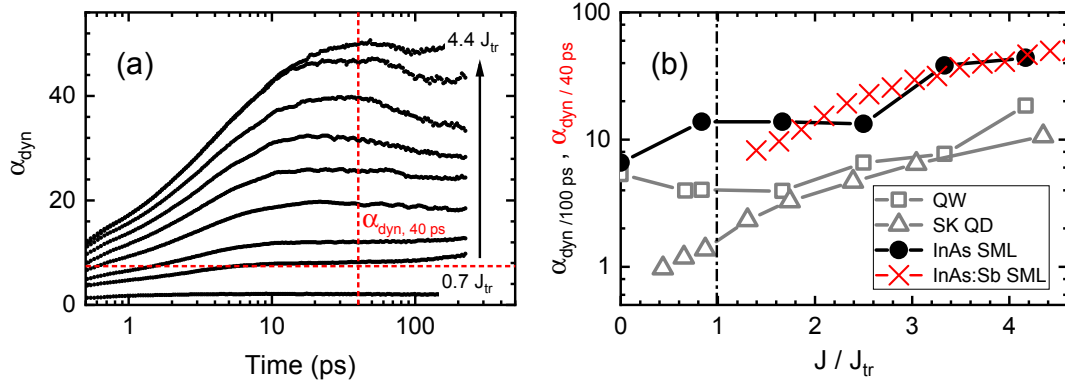
Figure 5.15.: (a) Temporal development of the dynamical α-parameter of an SML:Sb$_{1060}$ based SOA. (b) Equilibrated α_{dyn} in comparison to the measurements on a MQW, SK QD, and SML$_{960}$ based SOA according to Figure 5.14 [1].

unbound carriers. As a mixed dimensional system, an enlargement of the SML dot sizes would increase the electron binding energy leading to 0D confinement, while reduction would decrease the hole binding energy, translating into 2D confinement [3]. Both situations would thus lower the α-parameter.

5.5.2. Influence of the Sb-Alloy

Considering widely established bimodal systems, such as that of SK QDs attached to a surrounding QW (DWELL), B. Lingnau et al. investigated the temporal evolution of α_{dyn} via rate equation modelling according to subsection 2.2.4 [6]. Since SK QDs are known for relatively low amplitude-phase coupling, it has been found that the peak magnitude of α_{dyn} for those structure depends on both, the confinement energy and the inhomogeneous broadening, leading to lower values for narrow and largely confined states. The distinction into individual contributions of QD states and reservoir revealed that mainly the reservoir refilling rate determines the equilibration time of α_{dyn}.

Figure 5.15 (a) shows the temporal evolution of α_{dyn} of an SML:Sb$_{1060}$ SOA under injection from 0.7 to 4.4 times the transparency current. The spectral range of measurement was chosen as 1060 nm, which overlaps with the spectral transition edge of the Sb and SML states. A comparable temporal development to the InAs SML QDs based SOAs in Figure 5.13 (h) is observed.
At small delay times and low currents a single-digit value for α_{dyn} was obtained, fol-

lowed by a rise to very high values of up to 50 on the timescale of 10 ps. This rise time is much faster than for the pure InAs SML QDs, though in some cases in particular for large currents there is a small overshoot with the final equilibrium value being reached at about 40 ps [1].

These quasi-steady state values are plotted in Fig. 5.15 (b) versus injection current. A monotonic growth of α_{dyn} from values close to unity at transparency up to values above 40 at a fourfold transparency current have been observed. The high value of α_{dyn} signifies that devices based on SML:Sb QDs will display large optical nonlinearities. Furthermore, assuming a linear dependence for $n(N)$ in Equation 2.24, the linear increase of α_{dyn} indicates a reciprocal dependency $G(N) \propto N^{-1}$, which is the case for, e.g., free carrier absorption [118, 119]. Again it needs to be stated that α in terms of α_{dyn} is by no means considered as constant, since carrier thermalization and recombination are nonlinear processes with different contributions to gain and refractive index modulation [1].

6. Semiconductor Lasers

After successful integration of both, the InAs/GaAs as well as the InAs/GaAs:Sb SML QD material system into SOAs, this chapter treats the application as SCLs, initially analyzing static device properties. All investigated lasers belong to the *1060-* sample series, as introduced in section 4.2. The sample pool consists of lasers not only based on a single layer of SML QDs, but also based on a SQW or an SK QD layer. However, the focus of investigations will lie on the SML:Sb system, since only little is known about that material so far. The chapter treats the following:

- A comparable quantum efficiency and corresponding temperature stability of all devices with an significantly increased lasing threshold for the SML:Sb material.

- Increased material gain of SML:Sb QDs as compared to the reference media.

- Unveiling of an additional exciton state after expansion of the rate equation model for SML QD to the SML:Sb dots.

6.1. Characteristics

Capturing the characteristics of an SCL first and foremost means capturing emission spectra and light-current dependence. While the former provides information about lasing wavelength and bandwidth the latter is leads to lasing threshold and quantum efficiency of the respective devices. At last the material will be analyzed regarding modal and material gain, measured via the Hakki Paoli method.

6.1.1. Development of the Lasing Line

The main difference between an SCL and an SOA lies in the presence or absence of optical feedback, which is why the term *ASE* becomes inappropriate and rather will be replaced by electroluminescence (EL). EL spectra of all samples were recorded
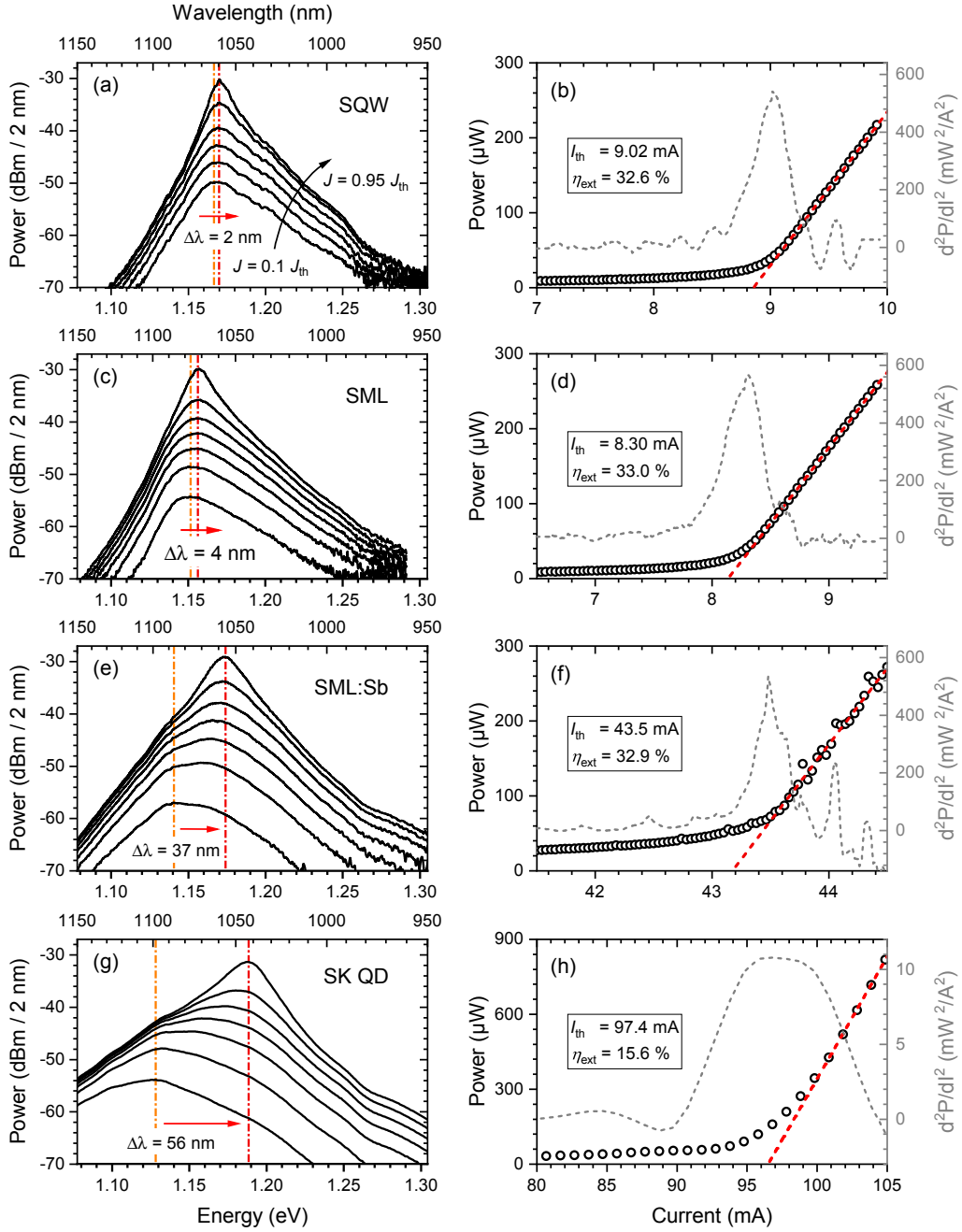
Figure 6.1.: Room temperature electroluminescence spectra and light-current characteristics of lasers from the *1060*-sample series with a 1.0 mm long single-modal cavity based on one layer of the (a)-(b) SQW_{1060}, (c)-(d) SML_{1060}, (e)-(f) $SML:Sb_{1060}$, and (g)-(h) SK QD_{1060}, respectively. The spectra were recorded at different currents ranging from 0.1 to 0.95 times the respective threshold current J_th, determined from the light-current characteristics via linear fitting (dashed lines). Dash-dotted lines mark the spectral peak shift from low injection (orange) up to lasing (red). The second derivative method was applied to the light-current curves for threshold current determination (gray curves). Linear fits were used to obtain the slope efficiency (red dashed lines) [1].

Table 6.1.: Luminescence characteristics of all respective lasers.

	SQW	SML	SML:Sb	SK QD
λ_0 (nm)	1059.4	1072.8	1057.5	1043.1
$\Delta\lambda$ (nm)	2.2	4.4	37	56
I_{tr} (mA)	8.9	8.1	43.2	96.5

with an OSA according to subsection 3.2.2 at a resolution bandwidth of 2 nm. The left column in Figure 6.1 shows the spectra of all devices at different injection currents ranging from 0.1 to 0.95 times the respective lasing threshold J_{th}, obtained from the light-current characteristics in the right column from a linear fit.

Even though the devices were designed for emission at 1060 nm the individual electronic structure satisfies the lasing condition at differing wavelength, respectively. Typically the EL peak of ordinary Fabry-Pérot SCLs experiences a slight blue shift at the transition to lasing due to general state filling of the electronic system. However the exact filling mechanism mainly is determined by the individual DOS and carrier lifetimes, which is of different complexity for all devices.

The peak shift is indicated in the figure by a dash-dotted orange line for the low injection peak and a red line for the lasing wavelength. While for the SQW_{1060} and SML_{1060} SCLs the lasing line develops to a great extent in the region of the lowest emitting state, the EL peaks of the $SML:Sb_{1060}$ and SK QD_{1060} lasers shift significantly towards shorter wavelengths with higher current, indicating that lasing may take place at a higher exciton state, as it is found in SK QD excited state lasers [8, 9]. The parameters of all devices are listed in Table 6.1.

It has to be noted that values for state filling solely represent a lower bound, since processes of lattice heating lead to bandgap shrinkage and cavity expansion, thus counteracting and red-shifting the spectrum. Qualitatively the relocation of the lasing line for all devices correlates well with the respective amount of carrier localization in terms of mobility and exciton extension.

Since excitons in a standard InGaAs SQW to relax down to the sharp band edge of the 2D DOS, intrinsic absorption is overcome at this point due to the large DOS. SML QDs to some extent behave similar due to the efficient diffusion processes within the potential landscape. However the extended Gaussian DOS contains a not as steep red edge as compared to the SQW, providing too little gain for overcoming the lasing threshold, which is why lasing occurs at a slightly larger energy level with larger DOS. This leads to a slightly larger lasing threshold as compared to the SQW device. The large line shift of the SML:Sb and SK QD based lasers however originates from

filling of the additional exciton state below the one participating at the lasing process, introduced in section 5.4. This lower state must saturate first, since its gain is too little to overcome intrinsic losses for lasing. As for the SK QDs it is well known that for certain dot compositions the QD GS produces too little gain leading to ES lasing [8], as it seems to be the case in here. A similar reason might be true for the SML:Sb QDs, which further supports the assumption of a bimodal state distribution within the system.

6.1.2. External Quantum Efficiency

The next characteristic parameter for the SCL performance is the external differential quantum efficiency η_{EQE} (EQE), namely the number of emitted photons per injected electron-hole pair. Also known as slope efficiency the lasing output is typically linearly proportional to the laser drive current just above threshold and saturates or even decreases with higher current due to thermal heating and non-radiative recombination. It can be easily obtained from the slope of the optical power, measured in free space ideally at both facets for the lasing frequency $\nu_0 = c/\lambda_0$ via: [120]

$$\eta_{ext} = \frac{2e}{h\nu_0} \frac{dP_{ext}}{dI} \ . \tag{6.1}$$

The right column of Figure 6.1 shows the slope fit of the light-current characteristics of all devices and the thus obtained EQE quantities. While the SQW, SML, and SML:Sb lasers show comparable values of 33 % per facet, the SK QD devices only achieves approximately 16 % per facet. Note that the measurement has been performed by simultaneously measuring the EL spectra and the ouput power at either facet, which is why the attribute *per facet* for η_{EQE} is used. The significantly lower value for the SK QD based SCL mainly is due to the very large threshold current and accompanying thermal losses [13].

6.1.3. Increase of the Temperature Stability

Another application-relevant property is the temperature dependency of the lasing threshold current $J_{th}(T)$. As commercial devices usually must be certified for operation at temperatures between at least 0 and 85 °C, SCLs need to remain in lasing mode all over this temperature range. As stated earlier in subsection 6.1.2 temperature influences η_{EQE} due to increased absorbtion along the light propagation path. It has been found that the absorption edge of the active medium spectrally red-shifts
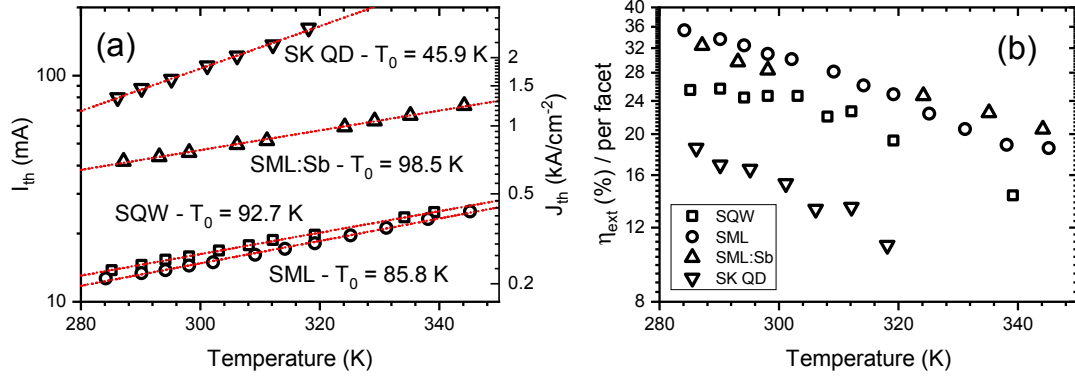
Figure 6.2.: (a) Temperature dependency of the threshold current I_{th} and threshold current density J_{th} of 2 mm long singlemode FP lasers from the *1060*-sample series. (b) Respective external quantum efficiency η_{ext}.

faster than the emission peak, leading to an exponential decay of the EQE [121]. As η_{EQE} and I^{-1} are reciprocally correlated, the threshold current simply follows:

$$J_{th}(T) = J_{th}(0) \cdot \exp\left(\frac{T}{T_0}\right),\qquad(6.2)$$

with the characteristic temperature T_0, scaling the threshold stability of the devices. In the experiment LI curves were recorded at different sample temperatures, using a Peltier-cooled copper mount with a thermistor-feedbacked PID controller. The temperature was tuned over a range of 10-80 °C with an accuracy of ±0.5 K. In contrast to the previous LI measurements, lasers with a longer cavity of 2 mm have been used for the sake of better heat dissipation. In Figure 6.2 the obtained values for the (a) threshold current and (b) external quantum efficiency for all devices are shown. Open symbols mark measured data and red dashed lines the exponential fits to obtain T_0. Since all devices were identically processed, differences in the characteristic temperature are solely determined by the temperature stability of the active medium itself. The following quantities have been obtained in this work or were reported in literature for an FP SCL with 1 mm cavity and slightly different SML composition, emitting at 980 nm:

	SQW	SML	SML:Sb	SK QD	SQW [122]	SML [122]
T_0 (K)	92.7	85.8	98.5	45.9	97.4	101.6

Remarkably the SML QD and SQW based lasers show a similar temperature stability, while T_0 for the SK QD SCL is significantly lower, leading to reduced stability. As SK QD are known for particular stable lasing and even values $T_0 \rightarrow \infty$ were reported

[123, 124], this result seems confusing. However, this is mainly the case for p-doped dots and additionally varying with the respective material composition. As the investigated SK QD SCLs need a relatively large current to reach the lasing threshold, showing low efficiency at the same time, a large nonradiative decay channel has to be assumed. Those mainly phonon-driven recombination processes become more efficient with higher temperature, leading to an increasing lasing threshold, which is also typical for undoped dots.

In contrast, a more substantial result can be found in the evaluation of the SML and SML:Sb lasers as compared to either the SQW reference device or also the older report of Ref. [122]. Amongst those, the SML:Sb SCL shows the most stable lasing threshold with T_0 = 98.5 K, while the SQW SCL performs intermediate with T_0 = 92.7 K, and the SML SCL show least stability. For SK QDs emitting in the 1.3 μm window, it has been found that the decreasing Auger recombination rate with the temperature plays the most important role for the threshold stability [123]. Regarding in particular the SML:Sb SCL, the increased stability hints at an increased carrier localization and less electron leakage. As compared to the SQW based device, the SML active medium shows a lower stability even though the quantum efficiency is large, which may be caused by an increased radiative recombination rate.

6.2. Material Gain

Initially one major motivation for development of the SML growth was the aim to increase the modal gain of zero dimensionally confined nanostructures by narrowing the emission linewidth [31]. When applied in waveguide structures this would translate into enlargement of the modal gain, which has been successfully reported for different SML compositons [2, 35, 122]. However the question arises whether the system of InAs/GaAs:Sb SML QDs is able to compete with the traditional SML system, since the broadened EL spectrum lets assume a reduction in modal gain. In this section both quantities, the modal and the material gain will be obtained for the SML:Sb$_{1060}$ SCL and subsequently be brought into relation to the performance of the SQW$_{1060}$, SML$_{1060}$ and SK QD$_{1060}$ lasers.

6.2.1. Modal Gain

The modal gain G, also denoted as *roundtrip gain* and earlier introduced in Equation 2.10, denotes the optical amplification along the laser cavity of the length L. It
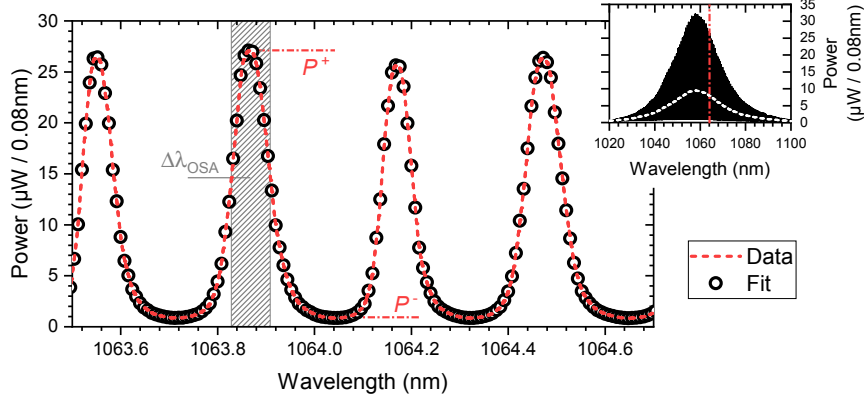
Figure 6.3.: Longitudinal modes of an SML:Sb SCL with a 0.5 mm cavity, driven at 0.9 J_{th}. Dots mark experimental data, dashed lines result from nonlinear mode fitting.

is linearly related to the material gain g_{mat} by the optical confinement factor Γ with $G = \Gamma g_{mat}$ to read:

$$G = \underbrace{\Gamma g_{mat} - \alpha_{mirr}}_{G_{net}} - \alpha_{int}, \tag{6.3}$$

with the cavity losses α subdivided into the out-coupling losses α_{mirr} and the internal waveguide losses α_{int}. Typically, gain measurement methods solely allow to obtain the net modal gain G_{net}, which still implies the waveguide losses α_{int}. While α_{mirr} can be easily determined from the mirror reflection coefficient R, α_{int} results from an extrapolation of G_{net} to the point of zero material gain.

The explicit measurement of G_{net} has been performed using the Hakki-Paoli method [91, 125] as earlier introduced in subsection 3.2.2. A set of basic transformations on Equation 3.6 leads to the calculation of G_{net} from the longitudinal mode power via:

$$G_{net} = \frac{1}{L}\left(\ln \frac{\sqrt{r}-1}{\sqrt{r}+1}\right) - \frac{1}{L}\ln R \tag{6.4}$$

with the amplitude ratio of:

$$r = \frac{P_i^{max} + P_{i+a}^{max}}{2P_i^{min}}, \tag{6.5}$$

as sketched in Figure 6.3. The goal of this section is thus to determine all geometric parameters in order to apply the Hakki-Paoli equation in order to obtain the material gain for the SML:Sb SCL as well as the reference devices. Owed to the limited OSA resolution of $\Delta\lambda_{min} = 0.08$ nm the HP method has been applied to the shortest available devices.
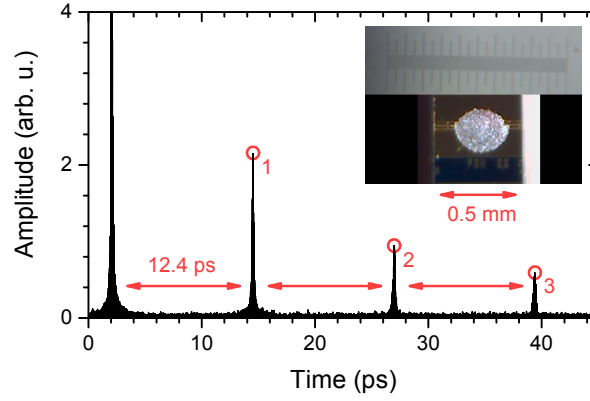
Figure 6.4.: Temporal echoes of a transmitted and partially reflected fs pulse through the waveguide of an SML:Sb$_{1060}$ SCL. Inset: microscope image and scale bar.

Geometric parameters like the cavity length L, the refractive index n and thus the mirror reflectivity R are measured by the optical cavity roundtrip time. To this end a weak fs-pulse has been coupled into the cavity, being reflected back and forth for if a current greater than the transparency current is applied. Via time-delayed interferometric measurement with respect to a temporally invariant local oscillator according to subsection 3.4.1, the distance of the reflected pulses can be determined with a high temporal resolution of about 300 fs. In order to ensure linear transmission the input power was limited to 15 μ W, translating into 0.2 pJ per pulse at 1060 nm.

The pulse train is plotted in Figure 6.4 and a roundtrip time of $\Delta t = 12.4$ ps was obtained for a driving current of 0.9 J_{th}. The inset of the figure shows a microscope image of an exemplary SCL as well as a μm-scale bar for determination of the cavity length. The obtained cavity length of $L = 0.50$ mm leads to an effective refractive index of:

$$n = \frac{c\Delta t}{2L} = 3.72 \,. \tag{6.6}$$

The mirror reflectivity then follows the Fresnel equations for perpendicular reflection on a dielectric surface to read:

$$R = \left(\frac{n_0 - n}{n_0 + n}\right)^2 = 0.33 \,, \tag{6.7}$$

with $n_0 = 1$ being the refractive index in air. Consequently the equivalent mirror losses are calculated via:

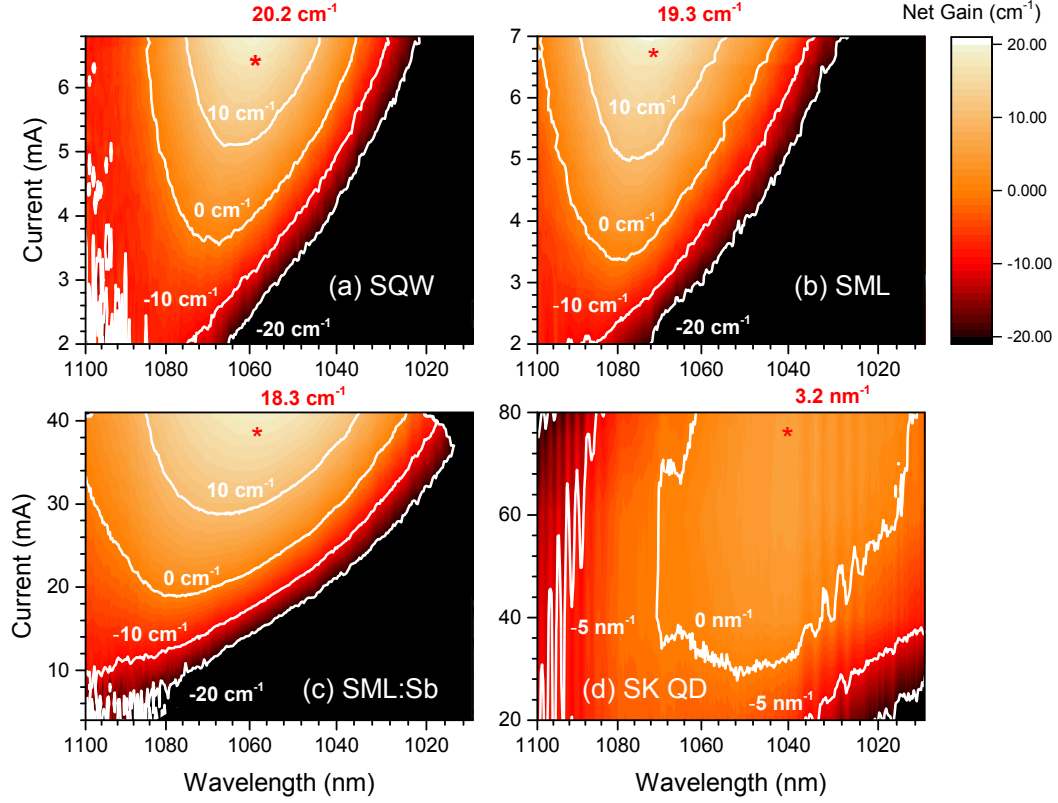$$\alpha_{mirr} = \frac{1}{L} \ln \frac{1}{R} = 22.1 \; cm^{-1} \,. \tag{6.8}$$

Figure 6.5.: Net modal gain of an (a) SQW_{1060}, (b) $Sb:SML_{1060}$, (c) SQW_{1060}, and (d) SK QD_{1060} laser obtained from Hakki-Paoli measurements.

Finally for proper HP measurement a sufficient relation of OSA resolution $\Delta\lambda$ and FP mode spacing $\delta\lambda$ has to be ensured. At a central wavelength of $\lambda_0 = 1060$ nm the modes of a 0.5 mm cavity are separated by

$$\delta\lambda = \frac{\lambda^2}{2L}. \tag{6.9}$$

As both quantities are only separated by a factor of four, a direct read out of $P^{max/min}$ from the OSA data would lead to an underestimation of g, which is why the data has to be deconvoluted with a Gaussian window function, considering $\Delta\lambda = 0.08$ nm:

$$H(\lambda) = \exp\left(4 \ln 2 \frac{(\lambda - \lambda_0)^2}{\Delta\lambda^2}\right). \tag{6.10}$$

The net modal gain below threshold was obtained after insertion of all geometric parameters into Equation 6.4. Represented as 2 D maps over driving current and wavelength Figure 6.5 shows the gain development of all lasers at driving currents be-

tween 0.1 to 0.95 J_{th}. The two-dimensional representation has been chosen for better comparison and overview. Regions of identical net gain were marked with white lines, where a value of $G_{net} = 0$ cm^{-1} corresponds to transparency or unperturbed pulse transmission. The quantities for all devices were obtained as follows:

Quantity	SQW$_{1060}$	SML$_{1060}$	SML:Sb$_{1060}$	SK QD$_{1060}$
G_{net} (cm^{-1})	20.2	19.3	18.3	3.2
$\Delta\lambda_{G,\,3dB}$ (nm)	13.7	17.9	28.0	57.0

The SML$_{1060}$ SCL shows a few differences as compared to the SQW reference. While the peak net gain at 0.95 J_{th} is slightly lower, the 3 dB bandwidth shows broader values. Both observations are valid for the SML:Sb$_{1060}$ SCL as well, with a significantly larger effect with respect to a reduced peak net gain and broader bandwidth. The SK QD based SCL amongst all samples shows the lowest peak gain and broadest bandwidth. As both quantities were observed to show a monotonous trend regarding the built-in material, it seems legit to address peak gain reduction and bandwidth broadening to the different charge carrier confinement. While carriers in the SQW are mostly decoupled, they are most able to relax to the bandedge where they can provide large and narrow gain. For both SML systems the more localized holes lead to broader state occupation with lower peak density. This effect is even stronger for layers of decoupled and inhomogeneously broadened SK QDs. Additionally for the SML:Sb the interplay of SML and Sb states with lasing performed at the former a further broadening is reached.

Regarding former research, Xu et al. reported 44 cm^{-1} of modal gain for an InAs/GaAs SML broad area laserdiode [35]. Since those devices showed internal losses of 33 cm^{-1}, the net modal gain is reduced to $G_{net} = 11$ cm^{-1} and thus lower than the data reported in this work. Regarding the SOAs from the *960* sample series subsection 5.1.1, a large modal gain and narrow gain bandwidth with fast gain recovery have been found within those SML based devices [2]. There the model of B. Lingnau et al. obtained a modal gain of 90 cm^{-1} with losses of 10 cm^{-1}. For those devices, however, it has to be noted that five QD layers were applied into the waveguide, leading to up to fivefold increased confinement factor and reducing the modal gain to below 20 cm^{-1} per layer.
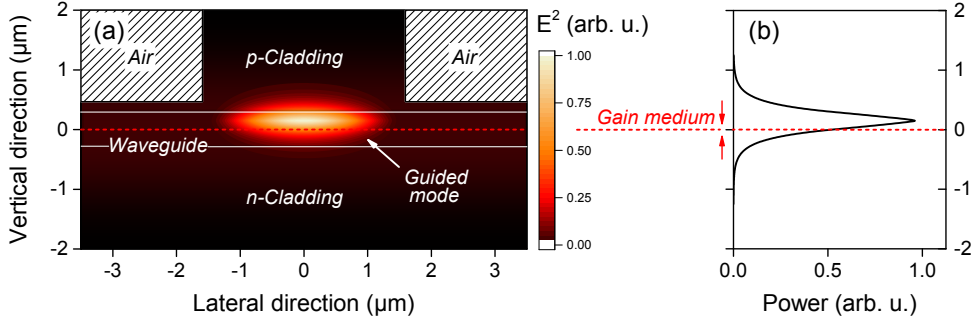
Figure 6.6.: Simulation of the mode field distribution of the waveguide layer structure for confinement factor calculation. (a) TE_{00} mode profile, (b) intensity cut. The red dashed line marks the position of the active layer [1].

6.2.2. Mode Confinement Factor

According to Equation 6.3 the material gain g_{mat} is linearly related to the net modal gain G_{net} by the confinement factor Γ, considering the overlap of the optical mode field with the active medium i. It is defined by:

$$\Gamma = \frac{\int_i E^2(x, y)\, dxdy}{\int_{-\infty}^{\infty} E^2(x, y)\, dxdy},$$ (6.11)

with the transversal electric (TE) field distribution $E^2(x, y)$, modeled from the refractive index calculated from the epitaxial layer structure. Since all devices were grown with identical layer structures except for the active region, a roughly comparable mode profile will be assumed. The calculation of the mode profile was performed according to Ref. [126] using a semi-analytical mode solver. The exact layer structure for the model was taken from growth and etch protocols as introduced in Figure 4.2 atsection 4.2. All calculations were performed for the case of zero current, leading to slight deviations at larger drive current due to current spreading, which was not determined in this work, but was assumed to only marginally influence the confinement factor Γ.

With the active medium vertical size d, taken according to growth protocols, the parameters for Γ and $g_{mat,\,max}$ were obtained as follows:

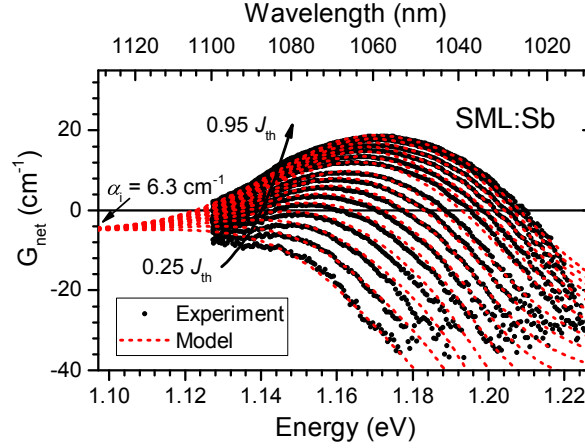| Quantity		SQW	SML	SML:Sb
d	(nm)	8.3	5.7	3.5
Γ	(%)	3.8	2.6	1.6
$g_{mat,\,max}$	(cm^{-1})	700	1000	1500

Figure 6.7.: Gain spectra of the SML:Sb$_{1060}$ SCL for injection currents ranging from 0.25 to 0.95 times the threshold. Black symbols mark experimental data, red dashed lines mark the modeled data [1].

Increasing values for the material gain from 700 to 1500 cm^{-1} for the SQW$_{1060}$ to the SML:Sb$_{1060}$ SCL have been found. The largest value for the SML:Sb$_{1060}$ device thereby mainly results from its lowest vertical expansion and thus smallest confinement factor. This, however, is a promising observation regarding high power laser fabrication, as it allows larger stacking of those respective structures and consequently larger achievable peak gain values.

6.2.3. SML:Sb Gain Modeling

Taking a closer look at the large material gain of InAs/GaAs:Sb SML QDs as active medium, the model of B. Lingnau et al. from section 5.4 was applied to the gain data from section 6.2. With the gain coefficient g, implicitly containing the waveguide properties in terms of mode confinement [114] and the group velocity v_g, the net gain follows:

$$G_{net}(E) = \frac{g}{v_g} \sum_m \int [2\rho^m(E') - 1] \mathcal{D}_m(E') \mathcal{L}(E' - E) \mathrm{E}' - \alpha_{int}. \tag{6.12}$$

In Fig. 6.7 the derived gain curves from Figure 6.5 (c), plotted as black symbols, are superimposed with the modeled data for different injection currents ranging from $J = 0.25...0.95\ J_{th}$, plotted as dashed red lines. The gain coefficient g was used as a fitting parameter and determined to $g = 3 \cdot 10^{-4}\ \mathrm{eV\,m^2s^{-1}}$. The good agreement of model and data represents a further prove for the validity of the bimodal state assumption.

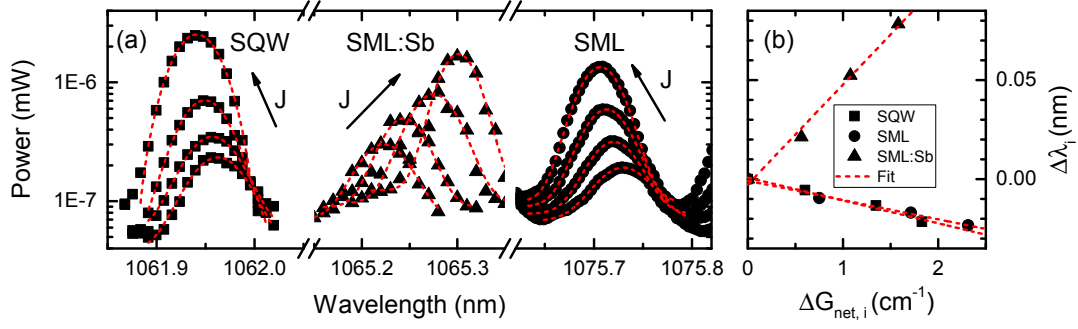Figure 6.8.: (a) Longitudinal mode development of the SML_{1060} and $SML{:}Sb_{1060}$ lasers as compared to the SQW_{1060} reference with rising injection current below threshold. (b) Obtained shift of gain and refractive index in order to obtain α_{stat}.

6.3. Alpha Parameter under Steady State Conditions

Regarding temporally slow changes as compared to internal time scales, a good estimate for the amplitude-phase coupling in SCLs is to measure the *static* alpha parameter α_{stat}, using the method of Henning and Collins [95], as introduced in subsection 3.2.3.

Similar to the HP method, HC is only valid below threshold due to the earlier mentioned roundtrip approximation. With the longitudinal Fabry-Pérot resonator modes of a free running SCL below threshold are shifting and rising with current, amplitude-phase coupling is obtained via:

$$\alpha_{stat} \approx \frac{2}{\delta\lambda \cdot L} \cdot \frac{\Delta\lambda_i/\Delta I}{\Delta G_{net,i}/\Delta I} \, , \tag{6.13}$$

as an approximation of Equation 3.7 according to Ref [127]. Applied to the previously studied laser structures of the *1060*-sample series the mode shift of the developing lasing wavelength of an SML, SML:Sb, and SQW SCL is shown in Figure 6.8 (a). The first thing to notice is the relatively large shift of the SML:Sb associated modes with opposite sign to the other SCLs. This is assumed to result from the deeper located Sb states not contributing to material gain at this spectral range, but influencing the phase, as the imaginary part of the dielectric function may tail up to that wavelength.

The slope of the respective mode shift with rising modal gain, as plotted in Figure 6.8
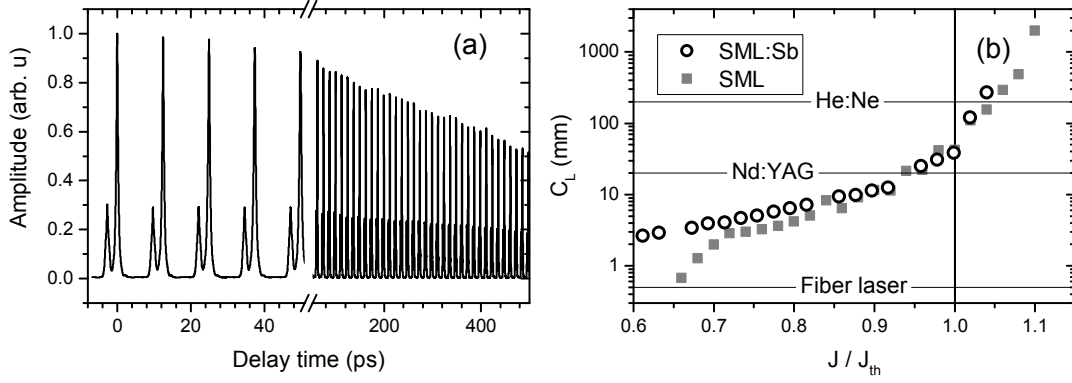
Figure 6.9.: (a) Inteferogram of a self-interfering SML:Sb laser at lasing threshold, measured via time-delayed optical heterodyne detection. (b) Obtained coherence length C_L for an SML_{1060} and an $SML:Sb_{1060}$ SCL. Typical values of other laser systems, taken from Ref. [128] are marked as rough guideline.

(b), according to Equation 3.7 leads to the absolute values of:

Quantity	SQW	SML	SML:Sb
α_{stat}	1.4 ± 0.1	1.3 ± 0.1	6.5 ± 0.3

While the static α-parameter for the SML SCL has been found to be comparable to the SQW reference, the SML:Sb shows a fourfold larger effect, promising for, e.g., nonlinear operating applications. As stated before the method of Henning and Collins solely yields α under steady-state conditions and therefore diverges from the dynamical value, as it was previously determined for SOAs.

6.4. Superluminescence

To proceed, an intrinsically broadly emitting material may be promising for short-coherent light emitter applications such as, e.g., superluminescent diodes for OCT, as it was introduced earlier in subsection 2.2.2. Since such diodes are typically driven below threshold, a determination of the respective coherence length L_C of both SML SCLs is highly interesting.

While for atomic or solid state lasers L_C directly follows from the width of the Lorentzian emission line, the calculation for SCLs, depends on multiple factors and requires detailed modeling. However, this quantity can also be directly obtained, using an interferometric measurement, such as, e.g., a Michelson interferometer. Since the heterodyne detection from subsection 3.4.1 incorporates an interferometer as well, it is used with the SCL itself as light source and scanning of the reference

delay.

In Figure 6.9 (a) an obtained interferogram of the SML:Sb SCL is shown at a driving current equal lasing threshold. There, the self-interference of this device shows a double peak signal, which is assumed to result from two different transverse output modes. Regarding the stronger mode, a monotonous decay towards larger delay times is observed, which can be fitted by an exponential decay function to obtain the coherence time $\tau_C = L_C/c$. The corresponding coherence length at different injection current is shown in Figure 6.9 (b). As the gain bandwidth generally decreases with larger injection, L_C of both devices rises as well. Both lasers were observed to show comparable results with single digit mm values below lasing threshold. As a guideline, typical values of a gas laser (He:Ne), solid state laser (Nd:YAG), and fiber laser [128] were added to the figure, indicating a smaller coherence length of the investigated devices when driven below threshold.

7. Delayed Optical Feedback and Chaos

Aiming the creation of nonlinear or even chaotic light sources, a large amplitude-phase coupling within the driving laser is mandatory. A convenient way to create non-deterministic light is to apply time-delayed optical self-feedback to a semiconductor laser, since for a certain range of feedback ratio and phase instabilities in the coherent cw light emission build up. Often considered as nuisance in linear data transmission, these complex light fluctuations have gained the maturity regarding, e.g., chaotic encrypted communication [23, 24] or light detection and ranging [22].

This chapter aims to analyze feedback sensitivity and achievable laser dynamics of both types of SML based lasers in order to explore their potential as active medium for non-deterministic semiconductor laser systems. In a combined study three Fabry Pérot lasers from the *1060*-sample series with a cavity length of 1 mm and 3 μm ridge will be analyzed regarding their response to delayed optical feedback and regimes of different dynamics will be identified. It has to be noted that the term *dynamics* in this chapter relates to laser instabilities rather than gain recovery as in chapter 5. All measurements of this chapter were taken in laboratory of Ingo Fischer at the IFISC (Spain). The following observations will be discussed in this chapter:

- A suitable quantity for laser dynamics characterization is represented by the intensity autocorrelation, marking regimes of as stable emission and weak chaos for the SQW_{1060} SCL.

- The SML_{1060} SCL has been found to show a number of different complex dynamics,comprising a region of strong chaos.

- The $SML:Sb_{1060}$ SCL showed rather weak response due to high damping, but a region of stable external cavity modes was observed.
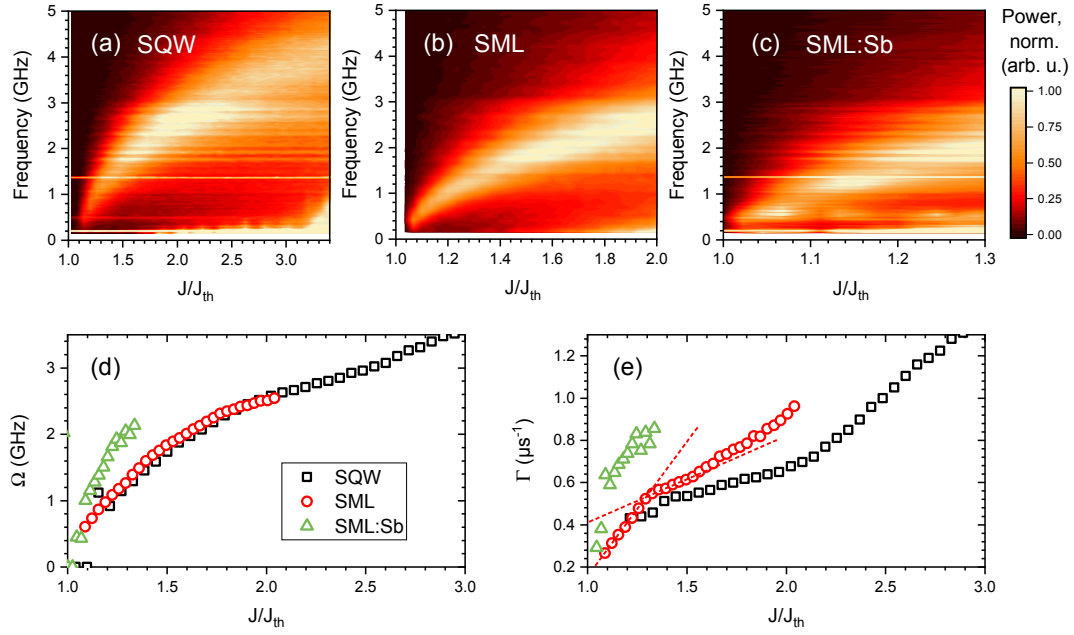
89

Figure 7.1.: Difference power spectra of an (a) SQW$_{1060}$, (b) SML$_{1060}$, and (c) SML:Sb$_{1060}$ SCL. Fitting the data delivers the (d) relaxation oscillation frequency Ω and the (e) damping rate Γ.

7.1. Application of an External Cavity

In order to apply an external cavity considered as *long*, its roundtrip time τ_{EC} needs to satisfy the condition $\tau_{EC} \gg \Omega^{-1}$ with Ω resembling the relaxation oscillation frequency ν_{RO} of the laser at a certain driving current. As introduced in section 2.3, under long cavity condition ECMs average over multiple ROs, thus neglecting the feedback phase. Consequently the relevant intrinsic time scales of the investigated lasers are determined by Ω and the damping rate Γ.

7.1.1. Relative Intensity Noise

The relative intensity noise (RIN) of semiconductor lasers denotes the measured laser output power noise normalized to its average power [129]. It is characterized by features related to internal time scales of the laser. When driven in cw mode under constant current injection, fluctuations of spontaneous emission influence the output power, since optical gain G and charge carrier density N are directly coupled (see subsection 2.2.5). Thus driving damped harmonic oscillations of the lasing mode, those fluctuations translate into an enhanced noise peak at the laser RO frequency, which is typically in the single-digit GHz range. Further under direct modulation, an

enhanced response is found in the range of the RO resonance [22].

For lasers based on either type of SML_{1060} QDs or the reference SQW_{1060}, laser noise spectra $P(f)$ have been taken and plotted in Figure 7.1 (a) - (c). All devices show enhanced noise incidence at around 500 MHz when driven at their respective lasing threshold, which shifts to larger frequencies with increasing current. In order to obtain Ω and Γ quantitatively and to reveal individual features of the respective active media, the spectra were fitted by an empirical function given by: [129, 130]

$$P(f) = \frac{Af^2 + B}{(\Omega^2 + \Gamma^2 - f^2)^2 + 4\Gamma^2 f^2} , \tag{7.1}$$

with A and B representing arbitrary fitting parameters. Results for the RO frequency Ω and damping rate Γ are shown in Figure 7.1 (d) and (e), respectively.

For the SML_{1060} SCL the RO frequency shows a comparable trend as compared to the SQW_{1060} reference, characterized by a square root dependency on the injection current up to double lasing threshold. The absolute values rise from 0.5 to 2.5 GHz. For the $SML:Sb_{1060}$ SCL a square root dependency is observed as well which, however, shows a much steeper trend regarding the current in multiples of the lasing threshold. This might be mainly caused by the relatively large threshold current leading to larger scattering rates, as it was discussed in chapter 5. Additionally the large J_{th} for the $SML:Sb_{1060}$ SCL limited the maximum applied current to prevent heating and degradation during measurement.

The damping of the free running SCLs monotonically rises with the injected current, showing slightly increased rates for the SML_{1060} SCL and a larger increase for the $SML:Sb_{1060}$ SCL as compared to the SQW reference. The SML_{1060} SCL additionally shows an unconventional dependency on the pump current with two linear regions, as marked in Figure 7.1 (e) by red dashed lines. This *kink* is assumed to originate from the pump-current dependent efficiency for carrier capture into the SML states according to section 5.2 [131]. Further that kink is not observed for the $SML:Sb_{1060}$ SCL, but might be shifted to larger injection current. The overall larger damping of this device follows the trend known for SK QD based SCLs, in which the stronger carrier confinement leads to enhanced damping of the ROs [114].

7.1.2. Feedback Rate and Threshold Current Reduction

In the next step a length-tunable external cavity was coupled to the respective SCLs according to the setup described in subsection 3.3.2. Via measuring the LI character-
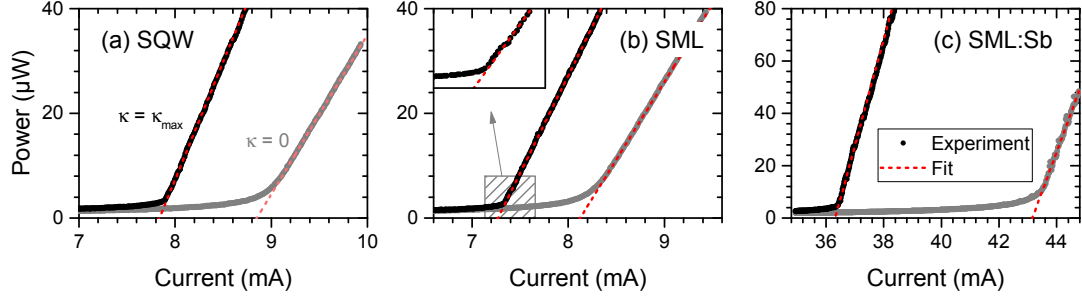
Figure 7.2.: Light-current characteristics of an (a) SQW_{1060}, (b) SML_{1060}, and (c) $SML:Sb_{1060}$ SCL with and without delayed optical self-feedback κ. The highlighted data shows the feedback-induced deviation from the linear lasing slope.

istics in the first step, the cavity has been characterized, including the determination of the maximum feedback ratio κ, as introduced in the LK equations in Equation 2.26. Typically the application of external feedback leads to two effects: firstly a threshold current reduction due to reinjection of photons and thus a decrease of cavity losses and secondly a deviation from the linear LI slope. The latter has been found to originate from light fluctuations caused by LFFs, which were induced by the external optical feedback [132].

The measured LI curves for the three investigated SCLs are plotted in Figure 7.2 for the free running lasers, as well as for the highest achievable feedback rate κ_{max} applied, respectively. The deviation from linearity at large κ for the investigated lasers is rather weak but existent, as it is shown in the inset of Figure 7.2 (b). This minor influence hints at a generally low feedback sensitivity for all lasers, which might be due to the single active layer, as well as the absence of a distributed grating.
Further, the SCL output under optical feedback shows a steeper slope with current than under free running conditions. This is due to the symmetric facet reflectivity of the devices from the *1060*-sample series, which protects the SCL cavity from an asymmetric power balance, often occurring for lasers with combined AR and HR coated facets, as in Ref. [89].

The magnitude of the feedback rate is given by: [132]

$$\kappa = \frac{(1-R)}{\tau_{LD}} \sqrt{\frac{R_0}{R}},$$

(7.2)

assuming a symmetric facet reflectivity $R = 0.33$ and the external cavity power reflectivity R_0, which also includes coupling losses [133]. κ is thus scaled with the SCL

Table 7.1.: Obtained light-current parameters in presence and absence of the external cavity.

Quantity	SQW_{1060}		SML_{1060}		$SML:Sb_{1060}$	
	LD	EC	LD	EC	LD	EC
I_{th} (mA)	9.02	7.90	8.30	7.34	43.48	36.49
dP/dI (A/W)	0.30	0.45	0.30	0.37	0.30	0.41
ΔI_{th} (%)	-	14	-	13	-	19
κ_{max} (ns^{-1})	-	37	-	21	-	30

internal cavity roundtrip time τ_{LD}, given by $\tau_{LD} = 2Lnc^{-1} = 23.3$ ps, which leads to a maximum feedback rate of 50 ns^{-1} in case of loss-free coupling $R_0 = R$.

In reality, however, not only the feedback mirror reflection, but also the collimation lens transmission and the deviation of the mode profile fram a Gaussian beam profile cause losses typically up to several dB. For better estimation of a maximum effective feedback rate κ_{eff}, the LI slope in presence and absence of the external cavity, denoted as *EC* and *LD*, have to be considered via: [134, 135]

$$\kappa_{eff} = \frac{(1-R)}{\tau_{LD}} \cdot \frac{E_{ph}}{e} \left[\left(\frac{\partial I}{\partial P} \right)_{LD} - \left(\frac{\partial I}{\partial P} \right)_{EC} \right], \tag{7.3}$$

with the photon energy E_{ph} and the electron charge e. The slope dP/dI of the respective LI characteristics was determined via linear fitting, leading to values for $\kappa_{max,eff}$ of 37, 21, and 30 ns^{-1} for the SQW_{1060}, SML_{1060}, and $SML:Sb_{1060}$ SCL respectively. The lasing threshold was calculated via second derivative method according to subsection 3.2.1, leading to an effective reduction of 14, 13, and 19 %, respectively. All results for the external cavity characterization are listed in Table 7.1.

7.2. Multimodal Feedback

After characterization of the free running SCL dynamics, as well as the external feedback rate, subsequently the feedback sensitivity of the SQW_{1060} laser was analyzed in order to obtain a reference for understanding occurring feedback regimes. Since the focus is on dynamics of the SML_{1060} and $SML:Sb_{1060}$ SCL, all results will be related to the SQW_{1060} reference. To this end the external cavity length was set to $L_{ext} = 58.0 \pm 0.5$ cm, leading to an effective roundtrip frequency of $\nu_{ext} = c_0/2L_{ext} = 260$ MHz, thus remaining in the long cavity regime. In a first experiment, a relatively large feedback rate of $\kappa \approx 25$ ns^{-1} has been applied to the
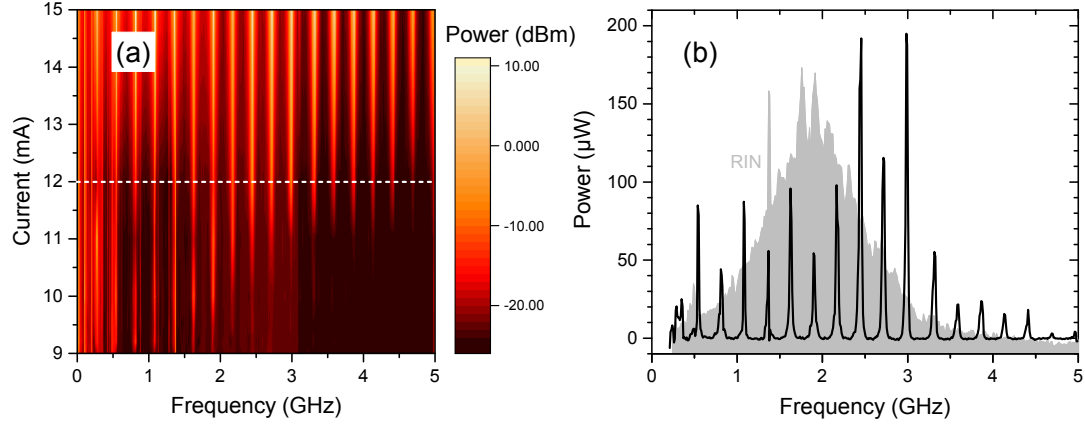
Figure 7.3.: (a) Power spectra of an SQW_{1060} SCL under delayed optical feedback of $\kappa \approx 25$ ns^{-1} for different injection currents. (b) Spectrum at $I = 12$ mA and comparison to the corresponding RIN spectra of the free running device.

laser, leading to undamping of the ROs and triggering cavity oscillations at frequencies in multiples of ν_{ext}.

7.2.1. Cavity and Longitudinal Modes

Electrical power spectra of the SQW SCL under constant feedback rate and for different injection currents are shown in Figure 7.3 (a) with a color coded logarithmic power scale. To obtain those spectra the ESA was set to a resolution (RBW) of 100 kHz with tenfold integration by means of the video bandwidth (VBW). The relatively large feedback rate has been chosen to ensure undamping of the laser ROs, leading to traveling ECMs, which are characterized by vertical lines in the spectra map at frequencies of $\nu \approx m \cdot 260$ MHz. Since the ROs are expected to couple to external cavity modes the center of gravity for the spectra rises with larger injection currents to higher frequencies and larger amplitudes.

A horizontal cut at a current of 12 mA is shown in Figure 7.3 (b) with a linear power scale. For comparison the corresponding RIN spectrum is plotted as grey filled area, matching the center of gravity of the cavity modes. It has to be noted that the spectra represent a temporal integration of the ECMs, showing a certain amount of fluctuations due to mode hopping and alternating damping and undamping of the ROs, which make the spectra rather *effective* than absolute.

In order to better understand this behavior, the ESA was replaced with a real-time spectrum analyzer (RSA) *Tektronix RSA 6114A*, which adds a temporal dimension to the electric power spectra. This helps to evaluate stability and reproducibility of the feedback dynamics. An exemplary RSA trace is shown in Figure 7.4 (a) for the
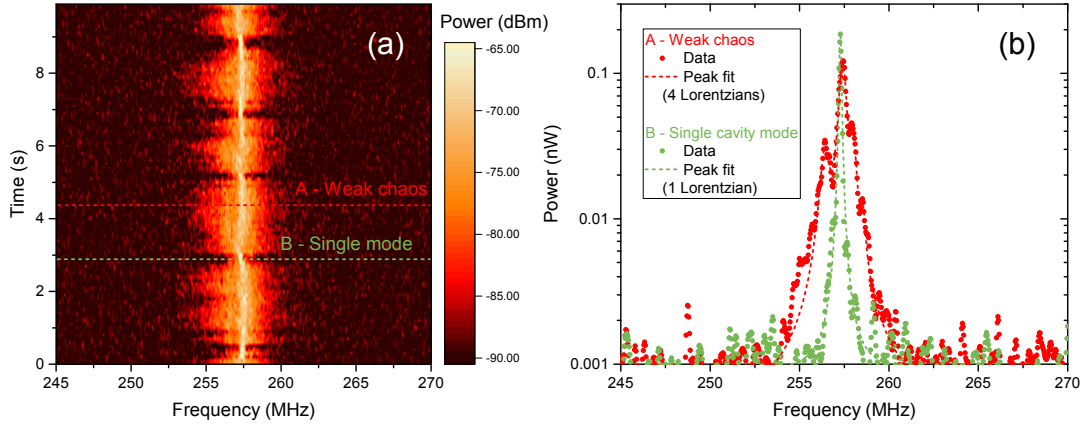
Figure 7.4.: (a) Real-time power spectrum at the first delay echo of an SQW_{1060} SCL under moderate feedback, driven at 12 mA. Each time trace integrates over a period of 100 ms. (b) Temporal cuts at a point of time with A: weak-chaotic oscillations and B: stable external cavity modes. The gray area marks the averaged data over the full time trace.

same device and operating conditions as in Figure 7.3. Using the same parameters for RBW and VBW, the RSA records one spectrum every 10 ms, which are put together to a spectral time trace.

Thus for those respective driving conditions the SQW SCL has been found to periodically switch between two operating modes: stable emission and weak chaotic pulsation, characterized by broad and sharp cavity echoes, as marked by *A* and *B* in the figure. Snapshots of those two modes are plotted in Figure 7.4 (b) and fitted by Lorentzian peak functions. Spectrum *A* was a sum of at least four Lorentzians, while for *B* one Lorentzian is sufficient. The width of each peak was found to be in the order of the RBW of roughly 100 kHz, which lets a assume even sharper delay echoes. The assembly of multiple Lorentzians for snapshot *A* indicates a switching of multiple quasi-stable modes on a shorter time scale.

Optical power spectra   in the next step are analyzed to gain information about the mode switching described above, since a competition of multiple longitudinal modes often occurs in FP lasers. With similar driving conditions as before, the optical power spectra of the SQW_{1060} SCL are shown in Figure 7.5 (a) for different injection currents. The longitudinal modes are represented by vertical lines, spaced by 0.15 nm (L = 1.0 mm). Since the threshold current was reduced by the optical feedback, a pronounced lasing line around 1063.9 nm builds up already at a driving current of 8 mA. A second line around 1064.2 nm rises at 10 mA and the number of dominant modes further increases with higher current, with the center of gravity shifting towards larger wavelengths, since the device heats up.
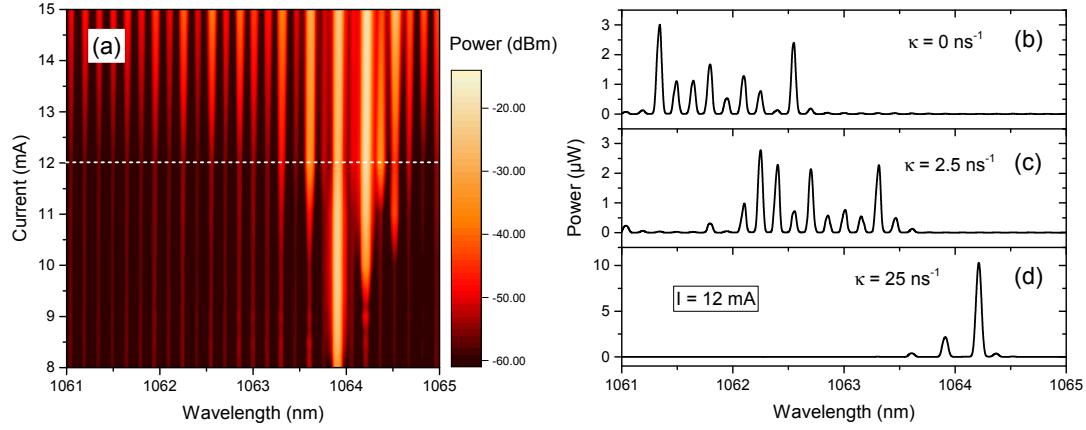
Figure 7.5.: (a) Optical Fabry-Pérot modes of the SQW$_{1060}$ SCL under feedback of $\kappa \approx$ 25 ns^{-1} at different injection currents. (b) - (d) Spectra of the free running device, moderate feedback, and strong feedback, respectively. The lasing modes shift towards longer wavelengths with larger feedback rates.

For a constant driving current of $I = 12$ mA, spectra were taken at different amounts of feedback rate κ, as shown in Figure 7.5 (b) - (d) for the free running device, moderate feedback, and strong feedback, respectively.

In the spectra a collective red shift of the emission with larger feedback rate was observed. This is assumed to result mainly from the feedback-induced threshold current reduction. Since the gain spectra fill up the energetically deepest states first, which in absence of the external cavity would provide too little gain to start the lasing process. However with increasing feedback ratio that threshold gets lowered and lasing is achieved, which also clamps the gain and prevents the blue states from filling. This also influences the mode competition of the FP laser at low feedback and gets modified at larger feedback rates, leading to one pronounced lasing mode, as observed in Figure 7.5 (d). It has to be noted that analogous to the previous electric spectra, the optical traces show some fluctuations as well, originating from hopping between damped and undamped ROs, which is why the spectra have to be understood as *effective* as well. However, the collective shift of the modes is maintained for all dynamics.

7.2.2. Intensity Time Series

Further insight into the feedback dynamics of the SQW$_{1060}$ SCL can be gained after recording the dynamics in the time domain. To this end real-time scope traces have been taken on a maximum bandwidth of 16 GHz and a sample spacing of 25 ps, as shown in Figure 7.6 (a) for the same device and driving conditions as in previous
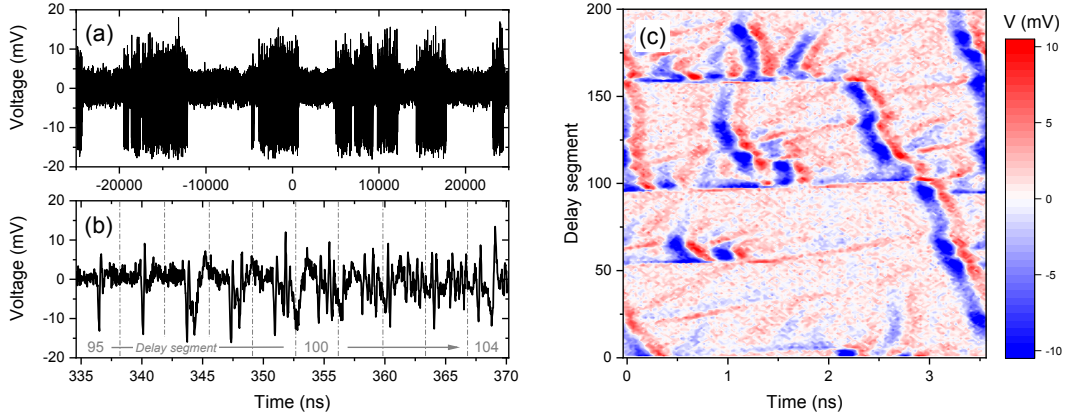
Figure 7.6.: Emission dynamics of a SCL laser at 1.5 J_{th} and a feedback rate of $\kappa \approx 25$ ns^{-1}. (a) Full scope trace reveals periods of stable emission and feedback-induced dynamics (b) zoom into a period of undamped relaxation oscillations, and (c) spatio-temporal representation of the period of (b).

measurements.

This 50 ms snapshot contains a time trace of an AC coupled 16 GHz photodetector with a total of $2 \cdot 10^6$ data points. In contrast to the time-integrated or slow measurements before, the trace now reveals periods of stable cw emission, translating in a flat detector signal, and periods of feedback-induced laser dynamics. A zoom into the trace is shown in Figure 7.6 (b) on a temporal window of 11 cavity roundtrips of 3.6 ns duration each. The trace reveals different types of dynamics: segments 93 and 94 show a single pronounced dip, representing a single oscillating ECM. While this mode is still visible in segment 95, it is followed by an additional collapse with rather slow recovery, as it is typical for LFFs. From segment 100 on multiple modes start to built up and the dynamics becomes more chaotic.

For better discernability of those different types of dynamics, a spatio-temporal representation helps to visualize traveling modes. In this way of visualization the dynamics the time trace is cut into integral multiple pieces of cavity roundtrips, which are stacked on top of each other with a color-coded power scale. A spatio-temporal plot of the laser dynamics within the time window of 0 to 720 ns is shown in Figure 7.6 (b). In this plot external modes propagate from bottom to top, while regular pulse packages being represented by a single pronounced traveling mode. LFFs in that case are represented by horizontal lines and chaotic fluctuations are identified by multiple modes, which also tend to jitter.

Since this trace already contains three different types of dynamics, a categorization of feedback regimes becomes difficult by only this single method. Consequently a further measure for characterization is required, which describes the degree of corre-
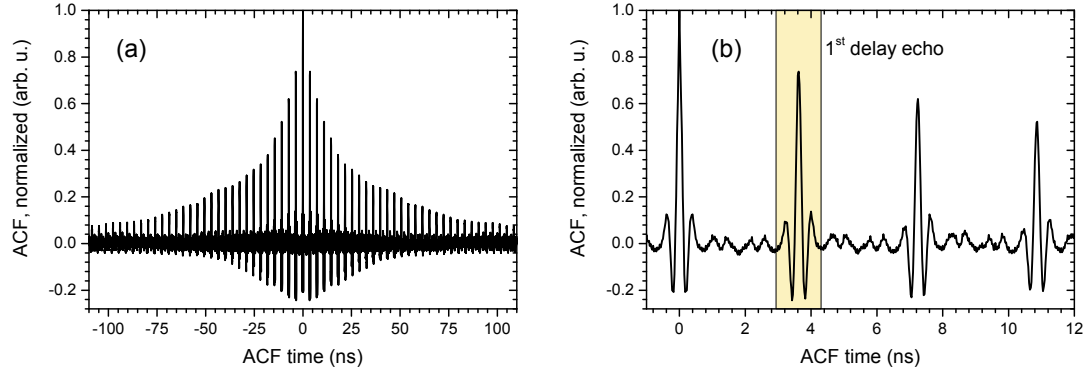
Figure 7.7.: (a) Autocorrelation function of the SCL laser emission dynamics at 1.5 J_{th} and a feedback rate of $\kappa \approx 25$ ns^{-1}. (b) Zoom into the region of the first three delay echoes.

lation within the time trace.

The intensity autocorrelation (AC) of a recorded time trace represents a commonly used approach to analyze the characteristics of a delayed feedback system [87, 89]. As introduced in subsection 2.3.2 the AC is calculated from the recorded intensity trace after Equation 2.28. Since the full trace contains $2 \cdot 10^6$ data points with a sample spacing of 25 ps, it includes more than 10^4 cavity roundtrips, thus containing time scales related to RO, ECM and even LFF.

The calculated normalized AC of the full intensity time trace from Figure 7.6 is shown in Figure 7.7 (a) on a time scale of 30 cavity roundtrips. A remarkably regular comb of delay echoes is observed with roughly exponentially decaying amplitudes. This hints at a relatively large amount of correlation and thus a major content of ECMs in the data. Figure 7.7 (b) shows a zoom into the first three delay echoes with the first rountrip highlighted. In the following this echo will considered as indicator for the regularity of the cavity oscillations according to Ref.[87]. A large echo amplitude represents a high amount of single ECMs, while a low amplitude either indicates chaotic pulsations or stable cw emission.

7.3. Regimes of Laser Dynamics

As it was observed in Figure 7.6 the laser dynamics of one snapshot may switch between different ECMs, cw or even chaotic pulsations. In order to categorize the dynamics into different regimes and to find a suitable quantity for comparison of different lasers, a reasonable evaluation algorithm had to be found. To this end for a constant driving current and varying feedback ratio the laser dynamics at each feedback
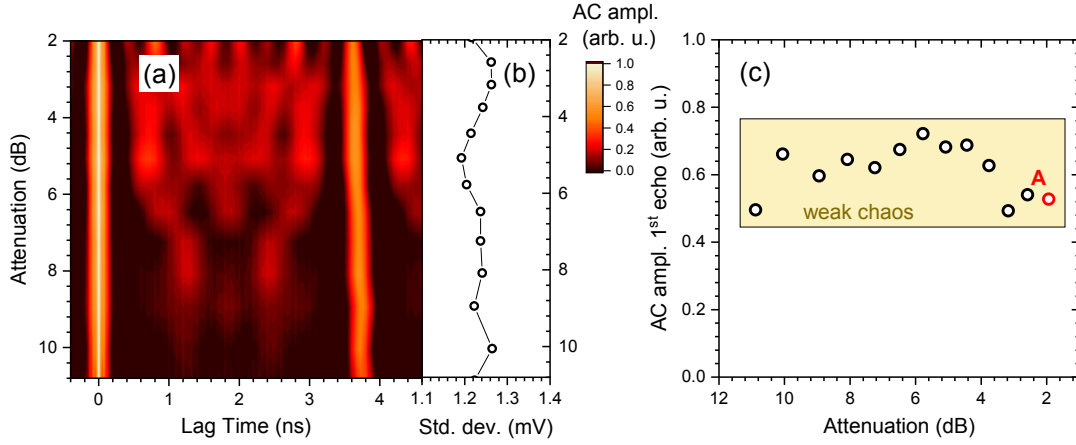
Figure 7.8.: (a) Center peak and first delay echo of the normalized autocorrelation function of the feedback-induced SQW$_{1060}$ SCL dynamics. The plot is an average of individual ACs of multiple dynamics periods. (b) Number of concatenated feedback events. (c) Amplitude of the first echo peak. The trace from Figure 7.6 is indicated as a red dot *A*.

level was cut into traces of single events of concatenated delay segments, character-ized by a standard deviation σ exceeding the detector noise. After autocorrelation of all events, the results were averaged and finally a mean AC was obtained.

7.3.1. SQW Lasers: Low Feedback Sensitivity

After application of the algorithm to the traces measured with the SQW$_{1060}$ SCL at 12 mA driving current, the effective AC, shown in Figure 7.8 (a) has been obtained from a number of feedback events, listed in (b). For this particular representation the applied attenuation μ was chosen for scaling rather than the feedback rate κ due to logarithmic tuning with a continuously variable attenuator and synchronized power measurement, as has been introduced in subsection 3.3.2:

$$\mu = 20 \log_{10} \left(\frac{\kappa}{\kappa_{max}} \right). \tag{7.4}$$

The AC map shows a rather stable echo peak for all attenuation values, as it is plotted in Figure 7.8 (c) and indicates low sensitivity of the SQW SCL to delayed optical feedback, denoted as *weak chaos*. For an attenuation of 12 dB or greater, the system has been found to be insensitive to any feedback at all, showing no dynamics and thus a disappearing AC echo peak. Regimes of strong chaos have not been observed for this particular device and driving current.
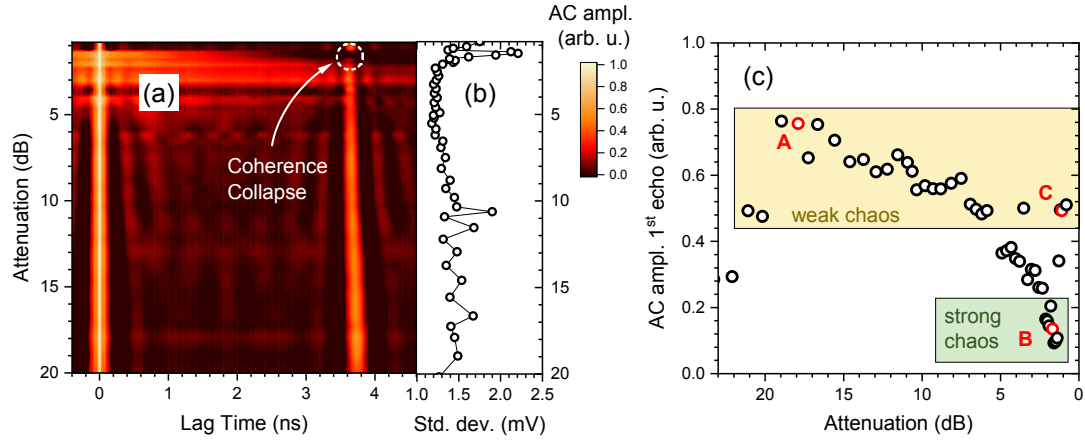
Figure 7.9.: (a) Obtained effective normalized autocorrelation function for an optically feed-backed SML$_{1060}$ SCL at similar driving conditions as the SQW$_{1060}$ SCL before. (b) Standard deviation σ of the full scope trace as measure for the intensity of laser dynamics. (c) Amplitude of the first echo peak.

## 7.3.2. SML Lasers: Regimes of Weak and Strong Chaos

Following the evaluation concepts described above, a similar routine was applied to an SML$_{1060}$ SCL of same length and ridge width as the SQW$_{1060}$ SCL from the previous section. For that device laser dynamics occurred already for an attenuation of $\mu \approx 20$ dB, which combined with the slightly lower achieved feedback ratio κ as listed in Table 7.1 results in an increased feedback sensitivity by one order of magnitude. The effective AC for a range of feedback applied ratios is plotted in Figure 7.9 (a). In contrast to previous measurements on the SQW based device, the SML$_{1060}$ SCL shows regions of multiple different dynamics including a complete breakdown of the first echo peak, as highlighted in the figure. The latter region at $\kappa \approx 2$ dB is assumed to result from a high degree of coherence collapse, thus indicating a region of strong chaotic light emission. This is further supported by Figure 7.9 (b), which indicates a high amount of dynamics events rather than cw emission.

The amplitude of the first AC delay echo is plotted in Figure 7.9 (c) showing regions of weak and strong chaos, characterized by their amplitude similar to Figure 2.11 and Ref. [87]. To better understand the chaotic characteristics, traces of both regions are analyzed in the following, as highlighted by red points *A - C* in the figure

All traces show different types of dynamics. Trace *A* is mainly characterized by short periods of ECMs, which only last for a couple of external cavity roundtrips and disappear again due to strong damping. In trace *C* in the *weak chaos* regime, the system switches between different ECMs, which hint on competition of at least two external
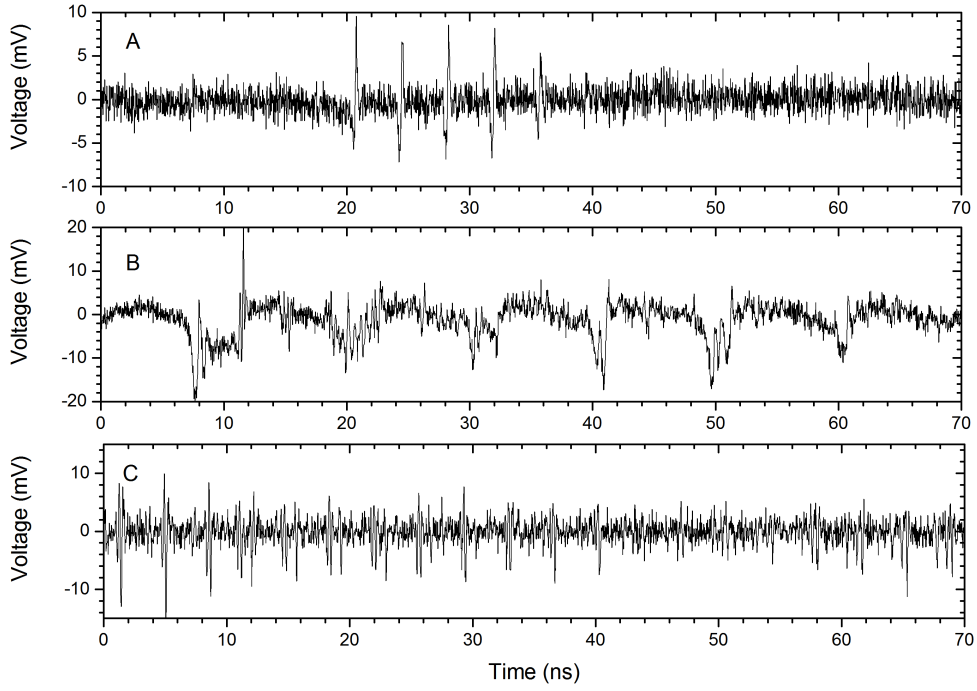
(a) SML SCL - Time domain representation
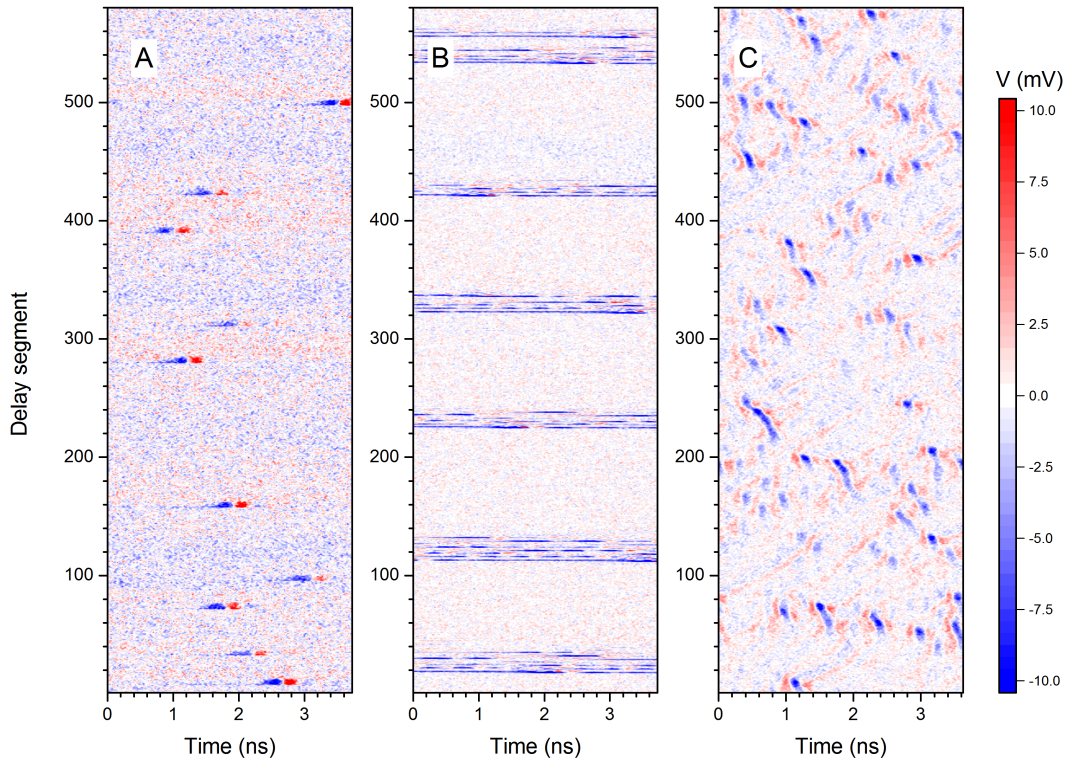
(b) SML SCL - Spatio-temporal representation

Figure 7.10.: (a) Temporal and (b) spatio-temporal represented snapshots of laser dynamics of an SML_{1060} SCL for feedback ratios enabling weak (A, C) or strong (B) chaos.
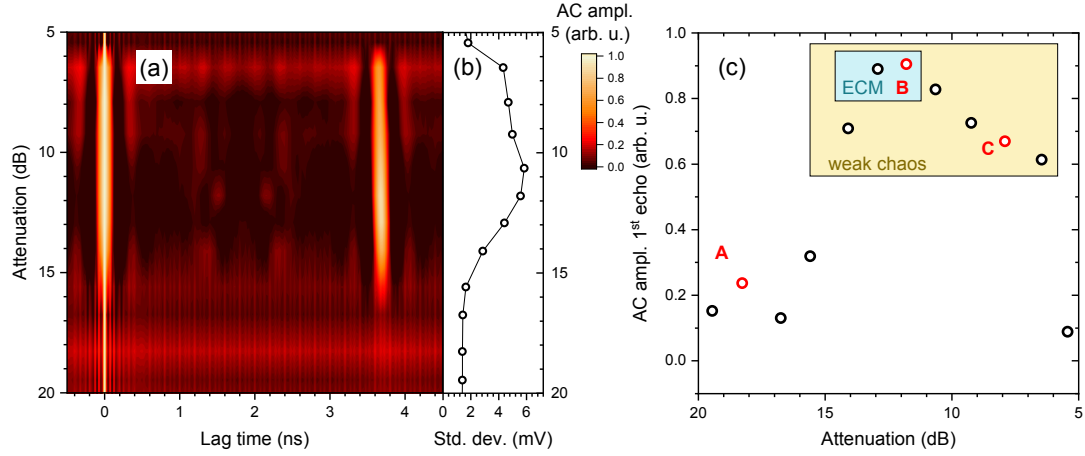
Figure 7.11.: (a) Effective normalized autocorrelation function of an SML:Sb$_{1060}$ SCL driven at 60 mA (1.5 J$_{th, LD}$) under delayed optical feedback. (b) Standard deviation σ of the full scope trace and (c) obtained amplitude of the first autocorrelated delay echo.

modes. The trace *B*, in contrast, shows periods with an amount of irregular break-downs of the lasing emission. This and even switching between two different output levels leads to a rather irregular output fluctuation and thus a collapse of the AC delay echo peak. Traces with that particular characteristic are considered as *strong chaotic* [87].

7.3.3. SML:Sb Lasers: Stable External Modes

Finally feedback analysis has been applied to an SML:Sb$_{1060}$ SCL of identical device geometry as the SML$_{1060}$ SCL and the SQW$_{1060}$ reference from previous measurements. Likewise the laser has been driven at $J \approx 1.5$ J$_{th, LD}$, which due to the larger lasing threshold translates into a roughly fivefold injection current of 60 mA. At that constant injection the feedback strength has been tuned to values from 0.03 to 25 ns^{-1} and snapshots of the dynamics have been taken.

After application of the evaluation algorithm a map of effective ACs has been obtained and plotted in Figure 7.11 (a). In contrast to the SQW$_{1060}$ and SML$_{1060}$ SCL, the SML:Sb$_{1060}$ laser dynamics has been found to show a single pronounced region between 6 and 16 dB attenuation where the correlated echo peak is extremely stable and rather large. The standard deviation plotted in (b) in that region is enlarged as well, indicating intensive dynamics. The first delay echo AC peak is shown in Figure 7.11 (c) with the region of weak chaotic dynamics highlighted as well.

The indicated points *A - C* in the figure mark regions of different dynamics, which are plotted in detail in Figure 7.12. As compared to point *A* in the SML$_{1060}$ dynamics,
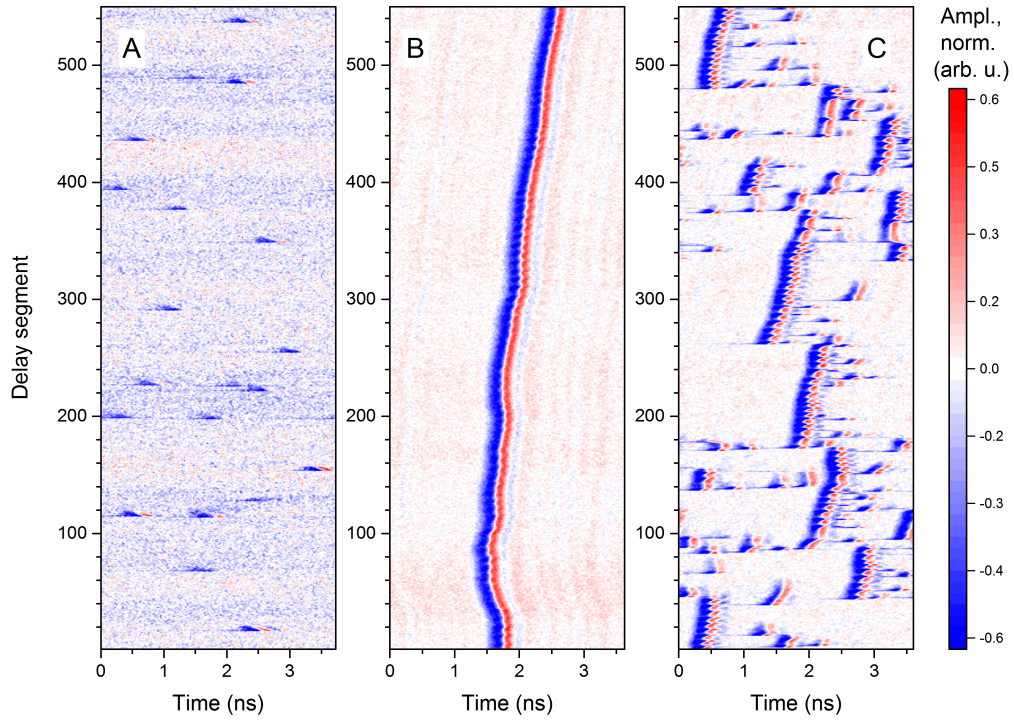
A in this figure resembles a region of low dynamics by means of single circulating pulses on a single-digit number of external cavity roundtrips, which again is assigned to weak chaotic dynamics. Trace *B*, in contrast, represents laser dynamics with a high degree of correlation. This plain form of a single oscillating ECM is marked in the figure as sub-area of the weak chaotic regimes. The spatio-temporal representation of this dynamics reveals fluctuations in the roundtrip time of that mode due to mainly device-internal jitter. Further a small number of weak echo modes can be identified as well, which are assumed to result from not-fully damped ROS. Trace *C* belongs to a dynamics region of increasing chaos which however shows only just enough correlation to be assigned to the weak chaos regime. As visible from the spatio-temporal representation in (b), the dynamics there is mainly described by one pronounced ECM, superimposed by a periodic intensity modulation and occasional attending sidemodes.

In contrast to the SML_{1060} SCL the dynamics of the $SML:Sb_{1060}$ SCL switch back directly from weak chaos to stable emission at higher feedback ratios without intermediate regions of strong chaos. This is assumed to result from the higher damping rate Γ as obtained from the RIN spectra in section 7.1.
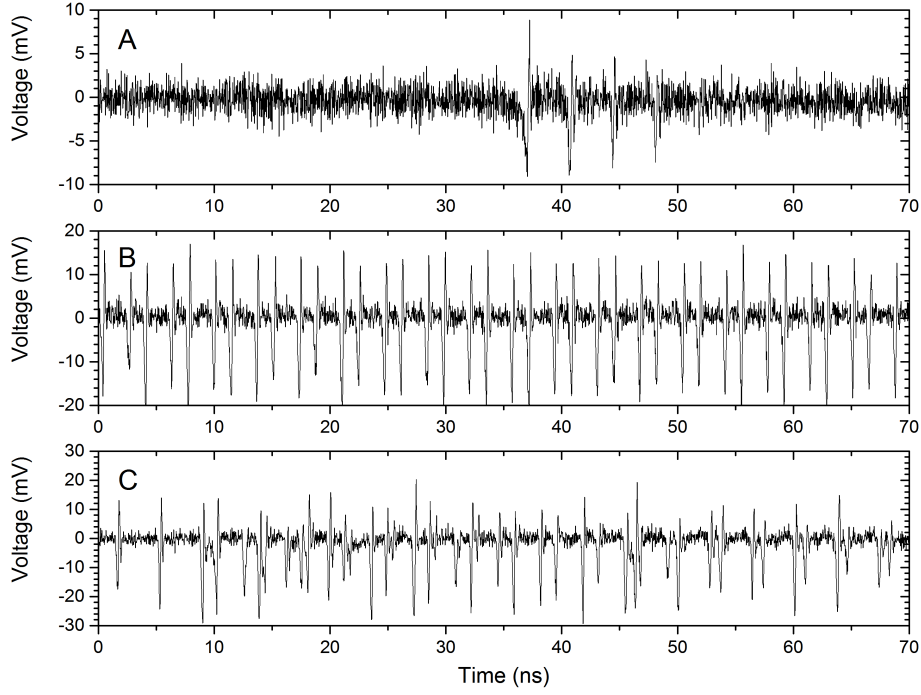
(a) SML:Sb - Time domain representation

(b) SML:Sb - Spatio-temporal representation

Figure 7.12.: (a) Time signature and (b) spatio-temporal represented snapshots of feedback-induced dynamics of an SML:Sb$_{1060}$ SCL driven at 60 mA (1.5 J$_{th}$). Trace *A* resembles a region of low dynamics, *B* shows high correlation by means of a single traveling ECM, and *C* shows weak-chaotic fluctuations, as comparable to the SQW$_{1060}$ SCL before.

8. Summary and Outlook

In the framework of this thesis the assets and drawbacks of submonolayer-grown quantum dots as gain medium in optoelectronic devices were analyzed. On the basis of multiple combined studies the potential of this material to replace established gain media based on nanostructured III-V compound semiconductors with transition energies in the near infrared range was exploited.

8.1. Material Properties

For submonolayer quantum dots as gain medium in semiconductor optical amplifiers a remarkably fast recovery was found in time-resolved and heterodyne-detected pump probe measurements, undercutting time constants found in quantum well structures and competing with established quantum dot gain media, grown in the Stranski-Krastanow mode. While the fast dynamics of the latter is known to result from an efficient carrier capture from the surrounding quantum well, submonolayer quantum dots have been found to be fed efficiently by an energetically adjacent reservoir of inactive exciton states. These states, however, not only speed up the gain recovery, but also cause a notably large phase response, which was unveiled through analyzing the complex signal after heterodyne detection. Further investigations of the phase response were quantified by Henry's α-parameter, which was found to exceed up to five times the values found in devices based on quantum wells or layers of self-assembled grown quantum dots.

In a second study, semiconductor lasers containing submonolayer quantum dots alloyed with antimony were fabricated and analyzed. As compared to reference lasers based on a single layer of unalloyed dots or a single quantum well, an increase of threshold current and gain bandwidth were observed. Both effects could be addressed to an additional antimony-induced confined state, which was revealed after modeling the low temperature luminescence decay. Like before, an exceptionally large α-parameter was found in devices based on antimony-alloyed submonolayer quantum dots as well.
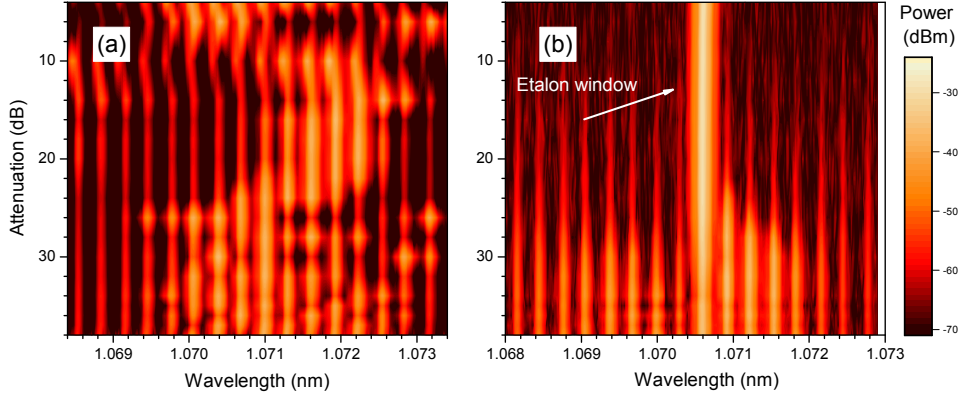
Figure 8.1.: (a) Multimodal vs. (b) singlemodal optical feedback of an SML QD based Fabry Pérot SCL at different feedback rates increasing from bottom to top.

8.2. Complex Laser Dynamics

The application of both types of submonolayer quantum dots for nonlinear device operation is therefore obvious and has been demonstrated. In particular the creation of chaotic light dynamics via time-delayed optical self-feedback was successfully demonstrated. In a combined study on edge-emitting Fabry Pérot lasers containing a single layer of either submonolayer quantum dots or a single quantum well, the induced laserdynamics were experimentally analyzed. While the latter sample was found to show a rather low feedback sensitivity, more complex dynamics were observed for the submonolayer quantum dot based lasers. For the sample without antimony even conditions for driving strong chaos were identified.

Following this empirical study, which aimed to prove the applicability of submonolayer quantum dots as gain medium for semiconductor chaotic light sources, further studies are recommended. Above all, understanding the complexity of this multimodal feedback would be of high interest. Grasping the direct link of laser dynamics to the alpha parameter, however, requires proper measurement and modeling of single mode dynamics in advance. Consequently a sharp selection of a single feedback mode in the experiment would be a next logical step. This was successfully demonstrated by use of a tailored etalon with a sharp transmission window and large free spectral range, matching the longitudinal cavity modes of the lasers, as it is demonstrated in Figure 8.1. In the figure a direct comparison of the optical spectra of a submonolayer based laser is demonstrated for different feedback ratios in (a) presence and (b) absence of the etalon. Remarkably already for feedback light below 1 % a pronounced laser line starts to dominate, which can be considered as single modal feedback.
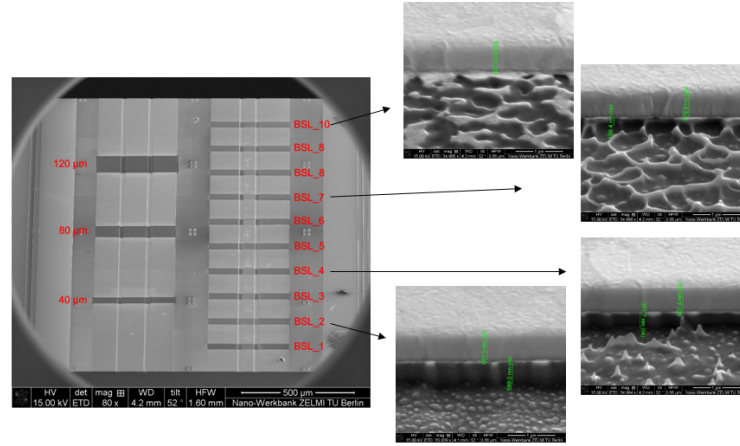
Figure 8.2.: Electron microscope image of semiconductor lasers based on antimony-alloyed submonolayer quantum dots. Different cuts demonstrated different cutting depth with the goal to create a two-section mode-lock laser.

Making use of this wavelength selection the experiments from chapter 7 need to be repeated for different selected modes. This can reduce the number of free parameters and also enable a proper application of the Lang-Kobayashi rate equation system, which consequently could be expanded by the developed dynamics model for the submonolayer quantum dots from Refs. [1–3]. After successful understanding and verification of the potential for chaotic light generation, proper device engineering is the next step. To this end not only one, but a larger number of submonolayer quantum dot layers should be implemented into devices, which further may contain a on-chip feedback line for plug-and-play generation of chaotic light pulsations.

8.3. Mode-Locking and Superluminescence

Besides the application in nonlinear laser sources, also large material gain of antimony-alloyed submonolayer quantum dots, accompanied by the broad gain bandwidth are worth further investigations. Both properties give rise to two more fields of application: superluminescent diodes and passively mode-locked lasers. While the former where already briefly investigated in this work, the creation of more optimized devices, containing more or even spectrally chirped active layers would be of keen interest.

Consequently a two-section device containing absorbing and gain region was aimed to be created by cutting the Fabry Pérot lasers of this work into two sections via

focused ion beam, as it is shown in Figure 8.2. While the cutting depth in this case is a crucial parameter determining optical, as such as electrical conduction, an optimized depth has not been found yet and further investigations will be performed in future. A first fabricated device already showed a number of oscillations, but died after a few tens of seconds under operation. However, the feasibility of modelocking in submonolayer based devices has been reported by C. G. E. Alfieri et al. [18] by means of a submonolayer quantum dot based external cavity laser. Following up the authors work a better result would be expected with antimony-alloyed dots due to the accessible broader gain bandwidth of this material.

Abbreviations

1cPP Single-color Pump Probe

2cPP Dual-color Pump Probe

AC Autocorrelation

AR Anti-Reflection

ASE Amplified Spontaneous Emission

CB Conduction Band

CC Coherence Collapse

CH Carrier Heating

cw continuous wave

DUT Device Under Test

DWELL Dots-In-A-Well

ECM External Cavity Mode

EL Electroluminescence

ES Excited State

ESA Electrical Spectrum Analyzer

FWHM Full Width at Half Maximum

GS Ground State

HR High-Reflection

LFF Low-Frequency Fluctuations

LI Light Power over Current

LK Lang-Kobayashi

LO Local Oscillator

MOVPE Metalorganic Vapour-Phase Epitaxy

MQW Multiple Quantum Well

NA Numerical Aperture

NIR Near Infrared

OSA Optical Spectrum Analyzer

QD Quantum Dot

RIN Relative Intensity Noise

RF Radio Frequency

RO Relaxation Oscillation

RTO Real Time Oscilloscope

SQW Single Quantum Well

SCL Semiconductor Laser

SCH Separate Confinement Heterostructure

SK Stranski-Krastanov

SLD Superluminescent Diode

SML Submonolayer

SOA Semiconductor Optical Amplifier

VB Valence Band

XGM Cross Gain Modulation

XPM Cross Phase Modulation

Bibliography

[1] B. Herzog, B. Lingnau, M. Kolarczik, S. Helmrich, A. W. Achtstein, K. Thommes, F. Alhussein, D. Quandt, A. Strittmatter, U. W. Pohl, O. Brox, M. Weyers, U. Woggon, K. Lüdge, and N. Owschimikow. Broadband semiconductor light sources operating at 1060 nm based on InAs:Sb/GaAs submonolayer quantum dots. *IEEE J. Sel. Top. Quantum Electron.*, 25(6): 1900310, 2019.

[2] B. Lingnau, K. Lüdge, B. Herzog, M. Kolarczik, Y. Kaptan, U. Woggon, and N. Owschimikow. Ultrafast gain recovery and large nonlinear optical response in submonolayer quantum dots. *Phys. Rev. B*, 94(1):014305, 2016.

[3] B. Herzog, B. Lingnau, M. Kolarczik, Y. Kaptan, D. Bimberg, A. Maaßdorf, U. W. Pohl, R. Rosales, J.-H. Schulze, A. Strittmatter, M. Weyers, U. Woggon, K. Lüdge, and N. Owschimikow. Strong amplitude-phase coupling in submonolayer quantum dots. *Appl. Phys. Lett.*, 109(20):201102, 2016.

[4] B. Herzog, N. Owschimikow, J.-H. Schulze, R. Rosales, Y. Kaptan, M. Kolarczik, T. Switaiski, A. Strittmatter, D. Bimberg, U. W Pohl, and U. Woggon. Fast gain and phase recovery of semiconductor optical amplifiers based on submonolayer quantum dots. *Appl. Phys. Lett.*, 107(20):201102, 2015.

[5] M. Kolarczik, C. Ulbrich, P. Geiregat, Y. Zhu, L. K. Sagar, A. Singh, B. Herzog, A. W. Achtstein, X. Li, D. Van Thourhout, Z. Hens, N. Owschimikow, and U. Woggon. Sideband pump-probe technique resolves nonlinear modulation response of PbS / CdS quantum dots on a silicon nitride waveguide. *APL Photonics*, 016101(3), 2018.

[6] B. Lingnau, B. Herzog, M. Kolarczik, U. Woggon, K. Lüdge, and N. Owschimikow. Dynamic phase response and amplitude-phase coupling of self-assembled semiconductor quantum dots. *Appl. Phys. Lett.*, 110(24): 241102, 2017.

110

[7] M. Kolarczik, N. Owschimikow, B. Herzog, F. Buchholz, Y. Kaptan, and U. Woggon. Exciton dynamics probe the energy structure of a quantum dot-in-a-well system: The role of Coulomb attraction and dimensionality. *Phys. Rev. B*, 91(23):235310, jun 2015.

[8] Y. Kaptan, A. Röhm, B. Herzog, B. Lingnau, H. Schmeckebier, D. Arsenijević, V. Mikhelashvili, O. Schöps, M. Kolarczik, G. Eisenstein, D. Bimberg, U. Woggon, N. Owschimikow, and K. Lüdge. Stability of quantum-dot excited-state laser emission under simultaneous ground-state perturbation. *Appl. Phys. Lett.*, 105(19):191105, 2014.

[9] Y. Kaptan, H. Schmeckebier, B. Herzog, D. Arsenijević, M. Kolarczik, V. Mikhelashvili, N. Owschimikow, G. Eisenstein, D. Bimberg, and U. Woggon. Gain dynamics of quantum dot devices for dual-state operation. *Appl. Phys. Lett.*, 104(26):261108, 2014.

[10] G. M. Hale and M. R. Querry. Optical constants of water in the 200-nm to 200-μm wavelength region. *Applied Optics*, 12(3):555–563, 1973.

[11] A. Y. Egorov, A. E. Zhukov, P. S. Kop'ev, N. N. Ledentsov, M. V. Maksimov, and V. M. Ustinov. Growth of (In,Ga)As/GaAs quantum-well heterostructures through the deposition of "submonolayer" strained InAs layers. *Semiconductors*, 28:363–366, 1994.

[12] A. E. Zhukov, A. R. Kovsh, S. S. Mikhrin, N. A. Maleev, V. M. Ustinov, D. A. Livshits, I. S. Tarasov, D. A. Bedarev, M. V. Maximov, A. F. Tsatsul'nikov, I. P. Soshnikov, P. S. Kop'ev, Zh. I. Alferov, N. N. Ledentsov, and D. Bimberg. 3.9 W CW power from sub-monolayer quantum dot diode laser. *Electron. Lett.*, 35(21):1845, 1999.

[13] S. S. Mikhrin, A. E. Zhukov, A. R. Kovsh, N. A. Maleev, I. S. Tarasov, D. A. Bedarev, B. V. Volovik, M. V. Maximov, and Zh. I. Alferov. 0.94 μm diode lasers based on Stranski-Krastanow and sub-monolayer quantum dots. *Semicond. Sci. Technol.*, 15:1061–1064, 2000.

[14] T. D. Germann, A. Strittmatter, J. Pohl, U. W. Pohl, D. Bimberg, J. Rautiainen, M. Guina, and O. G. Okhotnikov. High-power semiconductor disk laser based on InAs/GaAs submonolayer quantum dots. *Appl. Phys. Lett.*, 92(10):101123, 2008.

[15] J. O. Kim, S. Sengupta, A. V. Barve, Y. D. Sharma, S. Adhikary, S. J. Lee, S. K. Noh, M. S. Allen, J. W. Allen, S. Chakrabarti, and S. Krishna. Multi-stack

InAs/InGaAs sub-monolayer quantum dots infrared photodetectors. *Appl. Phys. Lett.*, 102, 2013.

[16] H. Ghadi, S. Sengupta, S. Shetty, A. Manohar, A. Balgarkashi, S. Chakrabarti, N. B. Pendyala, S. L. Prajapati, and A. Kumar. Comparison of Three Design Architectures for Quantum Dot Infrared Photodetectors: InGaAs-Capped Dots, Dots-in-a-Well, and Submonolayer Quantum Dots. *IEEE Trans. Nanotechnol.*, 14(4):603–607, 2015.

[17] Y. Kim, K.-Y. Ban, C. Zhang, and C. B. Honsberg. Material and device characteristics of InAs/GaAsSb sub-monolayer quantum dot solar cells. *Appl. Phys. Lett.*, 107(15):153103, 2015.

[18] C. G. E. Alfieri, D. Waldburger, J. Nürnberg, M. Golling, L. Jaurigue, K. Lüdge, and U. Keller. Mode-locking Instabilities for High-Gain Semiconductor Disk Lasers Based on Active Submonolayer Quantum Dots. *Phys. Rev. Appl.*, 10(4):044015, 2018.

[19] S. Sengupta, A. Mandal, H. Ghadi, S. Chakrabarti, and K. L. Mathur. Comprehensive study on molecular beam epitaxy-grown InAs sub-monolayer quantum dots with different capping combinations. *J. Vac. Sci. Technol. B*, 31(3): 03C136, 2013.

[20] D. Quandt, J. Bläsing, and A. Strittmatter. Analysis of InAsSb/GaAs submonolayer stacks. *J. Cryst. Growth*, 494:1–7, 2018.

[21] J. G. Fujimoto. Optical coherence tomography for ultrahigh resolution in vivo imaging. *Nat. Biotechnol.*, 21(11):1361–1367, 2003.

[22] M. C. Soriano, J. García-Ojalvo, C. R. Mirasso, and I. Fischer. Complex photonics: Dynamics and applications of delay-coupled semiconductors lasers. *Rev. Mod. Phys.*, 85(1):421–470, 2013.

[23] A. Argyris, D. Syvridis, L. Larger, V. Annovazzi-Lodi, P. Colet, I. Fischer, J. García-Ojalvo, C. R. Mirasso, L. Pesquera, and K. A. Shore. Chaos-based communications at high bit rates using commercial fibre-optic links. *Nature*, 438(7066):343–346, 2005.

[24] A. Uchida. *Optical Communication with Chaotic Lasers*. Wiley-VCH, 2011.

[25] R. Lang and K. Kobayashi. External Optical Feedback Effects on Semiconductor Injection Laser Properties. *IEEE J. Quantum Electron.*, 16(3):347–355, 1980.

[26] C. H. Henry. Theory of the linewidth of semiconductor lasers. *Quantum Electron. IEEE J.*, 18(2):259–264, 1982.

[27] R. N. Hall, G. E. Fenner, J. D. Kingsley, T. J. Soltys, and R. O. Carlson. Coherent Light Emission from GaAs Junctions. *Physical Review Letters*, 9(9): 366–369, 1962.

[28] D. Bimberg. Erratum for Quantum dot based nanophotonics and nanoelectronics. *Electron. Lett.*, 44(3):390, 2008.

[29] H. Ibach and H. Lüth. *Festkörperphysik - Eine Einführung in die Grundlagen.* Springer Verlag, 1981.

[30] D. Bimberg, N. Kirstaedter, N. N. Ledentsov, Zh. I. Alferov, P. S. Kop'ev, and V. M. Ustinov. InGaAs - GaAs Quantum-Dot Lasers. *IEEE J. Sel. Top. Quantum Electron.*, 3(2):196–205, 1997.

[31] M. V. Belousov, N. N. Ledentsov, M. V. Maximov, P. D. Wang, I. N. Yasievich, N. N. Faleev, I. A. Kozin, V. M. Ustinov, P. S. Kop'ev, and C. M. Sotomayor Torres. Energy levels and exciton oscillator strength in submonolayer InAs-GaAs heterostructures. *Phys. Rev. B*, 51(20):14346–14351, 1995.

[32] Z. Xu, K. Leosson, D. Birkedal, V. Lyssenko, J. M. Hvam, and J. Sadowski. In-GaAs/GaAs quantum-dot-quantum-well heterostructure formed by submonolayer deposition. *Nanotechnology*, 14:1259–1261, 2003.

[33] Z. Xu, Yating Zhang, Jørn M. Hvam, Jingjun Xu, Xiaoshuang Chen, and Wei Lu. Carrier dynamics in submonolayer InGaAs/GaAs quantum dots. *Appl. Phys. Lett.*, 89(1):013113, 2006.

[34] Z. Xu, Y. Zhang, A. Tackeuchi, Y. Horikoshi, and J. M. Hvam. Short exciton radiative lifetime in submonolayer InGaAs/GaAs quantum dots. *Appl. Phys. Lett.*, 92(6):063103, 2008.

[35] Z. Xu, D. Birkedal, M. Juhl, and J. M. Hvam. Submonolayer InGaAs/GaAs quantum-dot lasers with high modal gain and zero-linewidth enhancement factor. *Appl. Phys. Lett.*, 85(15):3259–3261, 2004.

[36] A. Lenz, H. Eisele, J. Becker, L. Ivanova, E. Lenz, F. Luckert, K. Pötschke, A. Strittmatter, U. W. Pohl, D. Bimberg, and M. Dähne. Atomic Structure of Buried InAs Sub-Monolayer Depositions in GaAs. *Appl. Phys. Express*, 3(10): 105602, 2010.

[37] A. Lenz, H. Eisele, J. Becker, J.-H. Schulze, Tim D. Germann, F. Luckert, K. Pötschke, E. Lenz, L. Ivanova, A. Strittmatter, D. Bimberg, U. W. Pohl, and M. Dähne. Atomic structure and optical properties of InAs submonolayer depositions in GaAs. *J. Vac. Sci. Technol. B*, 29(4):04D104, 2011.

[38] T. Niermann, F. Kießling, M. Lehmann, J.-H. Schulze, T. D. Germann, K. Pötschke, A. Strittmatter, and U. W. Pohl. Atomic structure of closely stacked InAs submonolayer depositions in GaAs. *J. Appl. Phys.*, 112(8): 083505, 2012.

[39] F. Hopfer, A. Mutig, G. Fiol, M. Kuntz, V. Shchukin, N. N. Ledentsov, and D. Bimberg. 20 Gb / s 85 °C Error Free Operation of VCSEL Based on Submonolayer Deposition of Quantum Dots. *IEEE J. Sel. Top. Quantum Electron*, 13(5):119–120, 2007.

[40] T. D. Germann, A. Strittmatter, U. W. Pohl, D. Bimberg, J. Rautiainen, M. Guina, and O. G. Okhotnikov. Quantum-dot semiconductor disk lasers. *J. Cryst. Growth*, 310(23):5182–5186, 2008.

[41] D. Quandt, J.-H. Schulze, A. Schliwa, Z. Diemer, C. Prohl, A. Lenz, H. Eisele, A. Strittmatter, U. W. Pohl, M. Gschrey, S. Rodt, S. Reitzenstein, D. Bimberg, M. Lehmann, and M. Weyland. Strong charge-carrier localization in InAs/GaAs submonolayer stacks prepared by Sb-assisted metalorganic vapor-phase epitaxy. *Phys. Rev. B*, 91(23):235418, 2015.

[42] J. O. Kim, Z. Ku, A. Urbas, and S. J. Lee. Investigation of the shape of submonolayer quantum dots using a polarization-dependent photocurrent. *Semicond. Sci. Technol.*, 30(11):115005, 2015.

[43] D. Das, H. Ghadi, S. Sengupta, A. Ahmad, A. Manohar, and S. Chakrabarti. Optimization of the number of stacks in the submonolayer quantum dot heterostructure for infrared photodetectors. *IEEE Trans. Nanotechnol.*, 15(2): 214–219, 2016.

[44] Y. Kim, K.-Y. Ban, and C. A. B. Honsberg. Multi-stacked InAs/GaAs quantum dots grown with different growth modes for quantum dot solar cells. *Appl. Phys. Lett.*, 106(22):222104, 2015.

[45] D. Guimard, M. Nishioka, S. Tsukamoto, and Y. Arakawa. Effect of antimony on the density of InAs/Sb:GaAs(1 0 0) quantum dots grown by metalorganic chemical-vapor deposition. *J. Cryst. Growth*, 298:548–552, 2007.

[46] U. W. Pohl, K. Pötschke, A. Schliwa, F. Guffarth, D. Bimberg, N. D. Zakharov, P. Werner, M. B. Lifshits, V. A. Shchukin, and D. E. Jesson. Evolution of a multimodal distribution of self-organized InAs/GaAs quantum dots. *Phys. Rev. B*, 72(24):245332, 2005.

[47] Yu. I. Mazur, V. G. Dorogan, G. J. Salamo, G. G. Tarasov, B. L. Liang, C. J. Reyner, K. Nunna, and D. L. Huffaker. Coexistence of type-I and type-II band alignments in antimony-incorporated InAsSb quantum dot nanostructures Yu. *Appl. Phys. Lett.*, 100:033102, 2012.

[48] S. Gies, M. J. Weseloh, C. Fuchs, W. Stolz, J. Hader, J. V. Moloney, S. W. Koch, and W. Heimbrodt. Band offset in (Ga, In)As/Ga(As, Sb) heterostructures. *J. Appl. Phys.*, 120(20), 2016.

[49] N. Owschimikow, M. Kolarczik, Y. Kaptan, N. B. Grosse, and U. Woggon. Crossed excitons in a semiconductor nanostructure of mixed dimensionality. *Appl. Phys. Lett.*, 105(10):101108, 2014.

[50] S. Harrison, M. P. Young, P. D. Hodgson, R. J. Young, M. Hayne, L. Danos, A. Schliwa, A. Strittmatter, A. Lenz, H. Eisele, U. W. Pohl, and D. Bimberg. Heterodimensional charge-carrier confinement in stacked submonolayer InAs in GaAs. *Phys. Rev. B*, 93(8):085302, 2016.

[51] K. P. O'Donnell and X. Chen. Temperature dependence of semiconductor band gaps. *Appl. Phys. Lett.*, 58(25):2924–2926, 1991.

[52] G. A. Alphonse, D. B. Gilbert, M. G. Harvey, and M. Ettenberg. High-Power Superluminescent Diodes. *IEEE J. Quantum Electron.*, 24(12):2454–2457, 1988.

[53] C. F. Lin and B. L. Lee. Extremely broadband AlGaAs/GaAs superluminescent diodes. *Appl. Phys. Lett.*, 71(12):1598–1600, 1997.

[54] P. D. L. Greenwood, D. T. D. Childs, K. Kennedy, K. M. Groom, M. Hugues, M. Hopkinson, R. A. Hogg, N. Krstajić, L. E. Smith, S. J. Matcher, M. Bonesi, S. MacNeil, and R. Smallwood. Quantum dot superluminescent diodes for optical coherence tomography: Device engineering. *IEEE J. Sel. Top. Quantum Electron.*, 16(4):1015–1022, 2010.

[55] S. Chen, W. Li, Z. Zhang, D. Childs, K. Zhou, J. Orchard, K. Kennedy, M. Hugues, E. Clarke, I. Ross, O. Wada, and R. Hogg. GaAs-Based Superluminescent Light-Emitting Diodes with 290-nm Emission Bandwidth by Using Hybrid Quantum Well/Quantum Dot Structures. *Nanoscale Res. Lett.*, 10(1): 0–7, 2015.

[56] A. Rostami, H. Baghban, and R. Maram. *Nanostructure Semiconductor Optical Amplifiers*. Springer Verlag, 2011.

[57] J. C. Simon. Semiconductor laser amplifier for single mode fiber communication systems. *J. Opt. Comm.*, 4(2):52–63, 1983.

[58] M. Born and E. Wolf. *Principles of Optics*. Pergamon Press, Oxford, 1993.

[59] D. Marcuse. Reflection loss of laser mode from tilted end mirror. *J. Lightw. Technol.*, 7:336–339, 1989.

[60] S. Philippe, A. L. Bradley, B. Kennedy, F. Surre, and P. Landais. Experimental Investigation of Polarization Effects in Semiconductor Optical Amplifiers and Implications for All-Optical Switching. *J. Light. Technol.*, 26(16):2977–2985, 2008.

[61] P. Borri, W. Langbein, J. M. Hvam, F. Heinrichsdorff, M.-H. Mao, and D. Bimberg. Ultrafast gain dynamics in InAs-InGaAs quantum-dot amplifiers. *IEEE Photonics Technol. Lett.*, 12(6):594–596, 2000.

[62] M. Sugawara, M. Mukai, and H. Shoji. Effect of phonon bottleneck on quantum-dot laser performance. *Appl. Phys. Lett.*, 71:2791–2793, 1997.

[63] A. V. Uskov, Y. Boucher, J. Le Bihan, and J. McInerney. Theory of a self-assembled quantum-dot semiconductor laser with Auger carrier capture: quantum efficiency and nonlinear gain. *Appl. Phys. Lett.*, 73:1499–1501, 1998.

[64] T. W. Berg and J. Mørk. Saturation and noise properties of quantum-dot optical amplifiers. *IEEE J. Quantum Electron.*, 40(11):1527–1539, 2004.

[65] B. Lingnau, W. W. Chow, E. Schöll, and K. Lüdge. Feedback and injection locking instabilities in quantum-dot lasers: a microscopically based bifurcation analysis. *New J. Phys.*, 15(9):93031, 2013.

[66] M. W. Fleming and A. Mooradian. Fundamental line broadening of single-mode (GaAl)As diode lasers. *Appl. Phys. Lett.*, 38(7):511–513, 1981.

[67] B. Lingnau, W. W. Chow, and K. Lüdge. Amplitude-phase coupling and chirp in quantum-dot lasers: influence of charge carrier scattering dynamics. *Opt. Express*, 22(5):4867–79, 2014.

[68] C. Harder, K. Vahala, and A. Yariv. Measurement of the linewidth enhancement factor α of semiconductor lasers. *Appl. Phys. Lett.*, 42(4):328–330, 1983.

116

[69] W. Rideout, B. Yu, J. LaCourse, P. K. York, K. J. Beernink, and J. J. Coleman. Measurement of the carrier dependence of differential gain, refractive index, and linewidth enhancement factor in strained-layer quantum well lasers. *Appl. Phys. Lett.*, 56(8):706–708, 1990.

[70] G. Liu, X. Jin, and S. L. Chuang. Measurement of linewidth enhancement factor of semiconductor lasers using an injection-locking technique. *IEEE Photonics Technol. Lett.*, 13(5):430–432, 2001.

[71] M. v. d. Poel, E. Gehrig, O. Hess, D. Birkedal, and J. M. Hvam. Ultrafast Gain Dynamics in Quantum-Dot Amplifiers: Theoretical Analysis and Experimental Investigations. *IEEE J. Quantum Electron.*, 41(9):1115–1123, 2005.

[72] J. Muszalski, J. Houlihan, G. Huyet, and B. Corbett. Measurement of linewidth enhancement factor in self-assembled quantum dot semiconductor lasers emitting at 1310 nm. *Electron. Lett.*, 40(7), 2004.

[73] T. C. Newell, D. J. Bossert, A. Stintz, B. Fuchs, K. J. Malloy, and L. F. Lester. Gain and linewidth enhancement factor in InAs quantum-dot laser diodes. *IEEE Photonics Technol. Lett.*, 11(12):1527–1529, 1999.

[74] I. O'Driscoll, T. Piwonski, C.-F. Schleussner, J. Houlihan, G. Huyet, and R. J. Manning. Electron and hole dynamics of InAs/GaAs quantum dot semiconductor optical amplifiers. *Appl. Phys. Lett.*, 91(7):071111, 2007.

[75] T. Fordell and Å. M. Lindberg. Experiments on the Linewidth-Enhancement Factor of a Vertical-Cavity Surface-Emitting Laser. *IEEE Photonics Technol. Lett.*, 43(1):6–15, 2007.

[76] S. Melnik, G. Huyet, and A. Uskov. The linewidth enhancement factor alpha of quantum dot semiconductor lasers. *Opt. Express*, 14(7):2950–2955, 2006.

[77] T. Heil, I. Fischer, and W. Elsäßer. Influence of amplitude-phase coupling on the dynamics of semiconductor lasers subject to optical feedback. *Phys. Rev. A*, 60(1):634–641, 1999.

[78] T. Heil, I. Fischer, W. Elsässer, and A. Gavrielides. Dynamics of Semiconductor Lasers Subject to Delayed Optical Feedback: The Short Cavity Regime. *Phys. Rev. Lett.*, 87(24):243901, 2001.

[79] T. Heil, I. Fischer, W. Elsäßer, B. Krauskopf, K. Green, and A. Gavrielides. Delay dynamics of semiconductor lasers with short external cavities: Bifurcation scenarios and mechanisms. *Phys. Rev. E*, 67(6):066214, 2003.

[80] M. Peil, I. Fischer, and W. Elsäßer. Spectral broadband dynamics of semiconductor lasers with resonant short cavities. *Phys. Rev. A - At. Mol. Opt. Phys.*, 73(2):023805, 2006.

[81] I. Fischer, G. H. M. Tartwijk, A. M. Levine, W. Elsäßer, E. O. Göbel, and D. Lenstra. Fast pulsing and chaotic itinerancy with a drift in the coherence collapse of semiconductor lasers. *Phys. Rev. Lett.*, 76(220), 1996.

[82] J. Mørk, B. Tromborg, and J. Mark. Chaos in semiconductor lasers with optical feedback: Theory and experiment. *IEEE J. Quantum Electron.*, 28(1):93, 1992.

[83] D. Lenstra, B. H. Verbeek, and A. J. den Boef. Coherence Collapse in Single-Mode Semiconductor Lasers Due to Optical Feedback. *IEEE J. Quantum Electron.*, 21(6):674–679, 1985.

[84] T. Heil, I. Fischer, and W. Elsäßer. Stabilization of feedback-induced instabilities in semiconductor lasers. *J. Opt. B*, 2:413–420, 2000.

[85] S. Heiligenthal, T. Dahms, S. Yanchuk, T. Jüngling, V. Flunkert, I. Kanter, E. Schöll, and W. Kinzel. Strong and weak chaos in nonlinear networks with time-delayed couplings. *Phys. Rev. Lett.*, 107(23):1–5, 2011.

[86] T. Jüngling, M. C. Soriano, N. O., and X. Porte. Consistency properties of chaotic systems driven by time-delayed feedback. *Phys. Rev. E*, 97(4):1–13, 2018.

[87] X. Porte, O. D'Huys, T. Jüngling, D. Brunner, M. C. Soriano, and I. Fischer. Autocorrelation properties of chaotic delay dynamical systems: A study on semiconductor lasers. *Phys. Rev. E*, 90(5):1–10, 2014.

[88] Sven Heiligenthal, Thomas Jüngling, Otti D'Huys, Diana A. Arroyo-Almanza, M. C. Soriano, I. Fischer, Ido Kanter, and W. Kinzel. Strong and weak chaos in networks of semiconductor lasers with time-delayed couplings. *Phys. Rev. E*, 88(1):1–13, 2013.

[89] X. Porte, M. C. Soriano, and I. Fischer. Similarity properties in the dynamics of delayed-feedback semiconductor lasers. *Phys. Rev. A - At. Mol. Opt. Phys.*, 89(2):1–6, 2014.

[90] D. M. Kane and J. P. Toomey. Precision Threshold Current Measurement for Semiconductor Lasers Based on Relaxation Oscillation Frequency. *J. Light. Technol.*, 27(15):2949–2952, 2009.

[91] B. W. Hakki and T. L. Paoli. Gain spectra in GaAs double-heterostructure injection lasers. *J. Appl. Phys.*, 46(3):1299–1306, 1975.

[92] V. Jordan. Gain measurement of semiconductor laser diodes: requirements for the wavelength resolution and sensitivity to noise. *IEEE Proc. - Optoelectron.*, 141(1):13–15, 1994.

[93] H. Wang and D. T. Cassidy. Gain measurements of Fabry-Pérot semiconductor lasers using a nonlinear least-squares fitting method. *IEEE J. Quantum Electron.*, 41(4):532–540, 2005.

[94] D. Hofstetter and J. Faist. Measurement of semiconductor laser gain and dispersion curves utilizing Fourier transforms of the emission spectra. *IEEE Photonics Technol. Lett.*, 11(11):1372–1374, 1999.

[95] I. D. Henning and J. V. Collins. Measurements of the semiconductor linewidth broadening factor. *Electron. Lett.*, 19(22):927–929, 1983.

[96] M. Kolarczik, N. Owschimikow, J. Korn, B. Lingnau, Y. Kaptan, D. Bimberg, E. Schöll, K. Lüdge, and U. Woggon. Quantum coherence induces pulse shape modification in a semiconductor optical amplifier at room temperature. *Nat. Commun.*, 4:2953, 2013.

[97] N. B. Grosse, N. Owschimikow, R. Aust, B. Lingnau, and U. Woggon. Pump-probe quantum state tomography in a semiconductor optical amplifier. *Opt. Express*, 22(26):1000–1003, 2014.

[98] M. Kolarczik. *Broadband ultrafast spectroscopy on mixed-dimensional InAs/GaAs systems*. PhD thesis, TU Berlin, 2019.

[99] P. Borri, F. Romstad, W. Langbein, A. Kelly, J. Mork, and J. M. Hvam. Separation of coherent and incoherent nonlinearities in a heterodyne pump-probe experiment. *Opt. Express*, 7(3):107–12, 2000.

[100] S. Schneider, P. Borri, W. Langbein, U. Woggon, R.L. Sellin, D. Ouyang, and D. Bimberg. Excited-state gain dynamics in InGaAs quantum-dot amplifiers. *IEEE Photonics Technol. Lett.*, 17(10):2014–2016, oct 2005.

[101] K. L. Hall, G. Lenz, E. P. Ippen, and G. Raybon. Heterodyne pump - probe technique for time-domain studies of optical nonlinearities in waveguides. *Opt. Lett.*, 17(12):874, 1992.

[102] G. Nardin, T. M. Autry, K. L. Silverman, and S. T. Cundiff. Multidimensional Coherent Photocurrent Spectroscopy of a Semiconductor Nanostructure. *Opt. Express*, 21(23):625–628, 2013.

Bibliography

[103] S. T Cundiff. Coherent spectroscopy of semiconductors. *Opt. Express*, 16(7): 4639, 2008.

[104] Q. Li, S. J. Xu, M. H. Xie, and S. Y. Tong. Origin of the 'S-shaped' temperature dependence of luminescent peaks from semiconductors. *J. Phys. Condens. Matter*, 17(30):4853–4858, 2005.

[105] E. C. Le Ru, J. Fack, and R. Murray. Temperature and excitation density dependence of the photoluminescence from annealed InAs/GaAs quantum dots. *Phys. Rev. B*, 67(24):1–12, 2003.

[106] A. J. Nozik. Spectroscopy and hot electron relaxation dynamics in semiconductor quantum wells and quantum dots. *Annu. Rev. Phys. Chem.*, 52:193–231, 2001.

[107] D. Bimberg and C. Ribbat. Quantum dots: lasers and amplifiers. *J. Phys. Condens. Matter*, 15:R1063, 2003.

[108] G. Eisenstein, J. M. Wiesenfeld, M. Wegener, G. Sucha, D. S. Chemla, S. Weiss, G. Raybon, and U. Koren. Ultrafast gain dynamics in 1.5 μm multiple quantum well optical amplifiers. *Appl. Phys. Lett.*, 58(2):158, 1991.

[109] L. Zhang, I. Kang, A. Bhardwaj, N. Sauer, S. Cabot, J. Jaques, and D. T. Neilson. Optical Amplifier Using p-Type-Doped Multiple Quantum Wells. *IEEE Photon. Technol. Lett.*, 18(22):2323–2325, 2006.

[110] T. Vallaitis, C. Koos, R. Bonk, W. Freude, M. Laemmlin, C. Meuer, D. Bimberg, and J. Leuthold. Slow and fast dynamics of gain and phase in a quantum dot semiconductor optical amplifier. *Opt. Express*, 16(1):170–178, 2008.

[111] A. Wilms, D. Breddermann, and P. Mathé. Theory of direct capture from two- and three-dimensional reservoirs to quantum dot states. *Phys. Status Solidi*, 9 (5):1158–1160, 2012.

[112] D. Z.-Y. Ting, S. V. Bandara, S. D. Gunapala, J. M. Mumolo, S. A. Keo, C. J. Hill, J. K. Liu, E. R. Blazejewski, B. Rafol, and Y.-C. Chang. Submonolayer quantum dot infrared photodetector. *Appl. Phys. Lett.*, 94(11):111107, 2009.

[113] H. Haug and H. Haken. Theory of noise in semiconductor laser emission. *Zeitschrift für Phys.*, 204(3):262–275, 1967.

[114] B. Lingnau, K. Lüdge, Weng W. Chow, and E. Schöll. Failure of the α factor in describing dynamical instabilities and chaos in quantum-dot lasers. *Phys. Rev. E*, 86(6):1–5, 2012.

[115] E. Gehrig and O. Hess. Dynamic amplitude-phase coupling in quantum-dot lasers. *Appl. Phys. Lett.*, 86(20):1–3, 2005.

[116] S. Schneider, P. Borri, W. Langbein, U. Woggon, R.L. Sellin, D. Ouyang, and D. Bimberg. Linewidth enhancement factor in InGaAs quantum dot amplifiers. *IEEE J. Quantum Electron.*, 40(10):1423–1429, 2004.

[117] M. Osinski and J. Buus. Linewidth broadening factor in semiconductor lasers– An overview. *IEEE J. Quantum Electron.*, 23(1):9–29, 1987.

[118] N. Storkfelt, B. Mikkelsen, D.S. Olesen, M. Yamaguchi, and K. E. Stubkjaer. Measurement of carrier lifetime and linewidth enhancement factor for 1.5- mu m ridge-waveguide laser amplifier. *IEEE Photon. Technol. Lett.*, 3(7):632– 634, 1991.

[119] J. Stohs, D. J. Bessert, D. J. Gallant, and S. R. J. Brueck. Gain, refractive index change, and linewidth enhancement factor in broad-area GaAs and InGaAs quantum-well lasers. *IEEE J. Quantum Electron.*, 37(11):1449–1459, 2001.

[120] P. M. Smowton and P. Blood. The differential efficiency of quantum-well lasers. *IEEE J. Sel. Top. Quantum Electron.*, 3(2):491–498, 1997.

[121] J. I. Pankove. Temperature Dependence of Emission Efficiency and Lasing Threshold in Laser Diodes. *IEEE J. Quantum Electron.*, 4(4):119–122, 1968.

[122] D. Arsenijević, C. Liu, A. Payusov, M. Stubenrauch, and D. Bimberg. Temperature-Dependent Characteristics of Single-Mode InAs Submonolayer Quantum-Dot Lasers. *Photonics Technol. Lett. IEEE*, 24(11):906–908, 2012.

[123] S. Fathpour, Z. Mi, and P. Bhattacharya. The role of Auger recombination in the temperature-dependent output characteristics ($T_0 = \infty$) of p-doped 1.3 μm quantum dot lasers. *Appl. Phys. Lett.*, 85(22):5164–5166, 2004.

[124] Z. Mi, P. Bhattacharya, and S. Fathpour. High-speed 1.3 μm tunnel injection quantum-dot lasers. *Appl. Phys. Lett.*, 86(15):1–3, 2005.

[125] D. T. Cassidy. Technique for measurement of the gain spectra of semiconductor diode lasers. *J. Appl. Phys.*, 56(11):3096–3099, 1984.

[126] O. V. Ivanova, M. Hammer, R. Stoffer, and E. van Groesen. A variational mode expansion mode solver. *Opt. Quant. Electron.*, 39(10-11):849–864, 2007.

[127] A. Schonfelder, S. Weisser, J. D. Ralston, and J. Rosenzweig. Differential gain, refractive index, and linewidth enhancement factor in high-speed gaas-based

mqw lasers: influence of strain and p-doping. *IEEE Photon. Technol. Lett.*, 6: 891, 1994.

[128] A. Deninger and T. Renner. *Diode Lasers - 12 Orders of Coherence Control.* TOPTICA Photonics AG, 2010.

[129] J. Wang and K. Petermann. Noise analysis of semiconductor lasers within the coherence collapse regime. *IEEE J. Quantum Electron.*, 27:3–9, 1991.

[130] G. Van Der Sande, M. C. Soriano, M. Yousefi, M. Peeters, J. Danckaert, G. Verschaffelt, and D. Lenstra. Influence of current noise on the relaxation oscillation dynamics of semiconductor lasers. *Appl. Phys. Lett.*, 88(7), 2006.

[131] B. Lingnau, K. Lüdge, and N. Owschimikow. Submonolayer quantum-dot lasers. *Proc. SPIE.*, 10098, 2017.

[132] C. H. Henry and R. F. Kazarinov. Instability of Semiconductor Lasers Due to Optical Feedback from Distant Reflectors. *IEEE J. Quantum Electron.*, 22(2): 294–301, 1986.

[133] J. Sigg. Effects of Optical Feedback on the Light-Current Characteristics of Semiconductor Lasers. *IEEE J. Quantum Electron.*, 29(5):1262–1270, 1993.

[134] N. Schunk and K. Petermann. Numerical analysis of the feedback regimes for a singlemode semiconductor laser with external feedback. *IEEE J. Quantum Electron.*, 24(7):1242–1247, 1988.

[135] L. Jumpertz, F. Michel, R. Pawlus, W. Elsäßer, K. Schires, M. Carras, and F. Grillot. Measurements of the linewidth enhancement factor of mid-infrared quantum cascade lasers by different optical feedback techniques. *Electron. Lett.*, 6(1), 2016.

Acknowledgements